

**The Creeping Motion and Deformation of Drops  
in Solid Constrictions**

by

**THOMAS JOHN RATCLIFFE**

B.S.E, University of Michigan, 2005

A dissertation submitted to the  
Faculty of the Graduate School of the  
University of Colorado in partial fulfillment  
of the requirement for the degree of  
Doctor of Philosophy  
Department of Chemical and Biological Engineering  
2011

This dissertation entitled:  
The Motion and Deformation of Drops in Solid Constrictions  
written by Thomas John Ratcliffe  
has been approved for the Department of Chemical and Biological Engineering

---

Robert H. Davis

---

Alexander Z. Zinchenko

Date\_\_\_\_\_

The final copy of this dissertation has been examined by the signatories, and we  
Find that both the content and the form meet acceptable presentation standards  
Of scholarly work in the above mentioned discipline.

Ratcliffe, Thomas J. (Ph.D., Chemical Engineering)

The Creeping Motion and Deformation of Drops through Solid Constrictions

Dissertation directed by Prof. Robert H. Davis and Dr. Alexander Z. Zinchenko

Understanding the nature of emulsion flows through confined geometries (i.e., packed beds, porous media, and the cardiovascular system) is substantially meaningful to numerous applications, such as food and pharmaceutical manufacturing, oil recovery and fixed-bed catalytic reactors, and also to many fundamental fields of science. When the drops are comparable in size to the constriction pathways, the traditional approach of treating an emulsion flow as a continuous phase is not valid, because complex phenomena, such as pore blockage, circuitous flow pathways, and drop squeezing mechanisms brought on by constrictions need to be considered.

To address some outstanding problems in emulsion flows with drops as large as the constrictions, this dissertation presents modeling and experimental observations of buoyancy-induced drop motion through tight constrictions. It concludes determining the critical conditions, below which a drop becomes trapped in the throat of a constriction, and above which the drop passes through a constriction. The key dimensionless parameter is the Bond number, representing a ratio of gravitational and interfacial forces.

It is found that the drop velocity in the constriction throat typically decelerates a 100-fold or more, and the drop-solid gap thickness typically decreases to 0.1%–1% of the undeformed drop radius. A power-law scaling is obtained, so that the time for a drop to pass through the constriction is inversely proportional to the square of the difference between the Bond number and its critical value, when a drop becomes trapped in the constriction.

Highly-accurate critical Bond numbers and statically trapped drop shapes for axisymmetric constrictions are efficiently calculated by a special static algorithm, and for three-dimensional constrictions, similar results are presented using a different solution approach of an artificial “time-dependent” process to reach the steady state. For both the axisymmetric and three-dimensional steady-state solution methods, a desirable benefit is that prior knowledge of the drop-solid contact is nonessential. Observed for both axisymmetric and three-dimensional constrictions, the critical Bond number nearly linearly increases with an increase in the most significant factor, the undeformed drop-to-hole size ratio. The critical Bond number decreases weakly, with an increase in the constriction cross-section, due to a smoother constriction pathway. Unexpectedly, increasing the tilt angle between the gravity vector and the normal to the plane of the constriction containing the minimum hole size, decreases the critical Bond number, even though the horizontal projection of the hole is decreased.

To Kim, John and Susan

## CONTENTS

## CHAPTER

1	Introduction.....	1
	1.1 Background.....	1
	1.2 Drop Squeezing and Static Entrapment in an Axisymmetric Constriction.....	4
	1.3 Drop Shapes Statically Trapped in a Three-dimensional Constriction .....	7
	1.4 Dissertation Approach .....	8
2	Buoyancy-induced squeezing of a deformable drop through an axisymmetric ring constriction .....	12
	2.1 Introduction.....	13
	2.2 Formulation of the Problem.....	16
	2.3 Boundary-integral Algorithm .....	17
	2.3.1 Formulation.....	19
	2.3.2 Handling Singularities in the Integrands .....	21
	2.3.2.1 Drop Self-interactions.....	22
	2.3.2.2 Solid Self-interactions .....	22
	2.3.2.3 Double-layer Solid-drop Contribution.....	22
	2.3.2.4 Single-layer Solid-drop Contribution .....	25
	2.3.3 Azimuthal Integrations .....	25

2.3.4 Additional Numerical Details .....	29
2.4 Static Algorithm Based on the Young–Laplace Equation .....	33
2.5 Numerical Results.....	38
2.5.1 Testing of the BI Algorithm .....	38
2.5.2 The Effect of a Geometric Barrier on Squeezing .....	38
2.5.3 Squeezing versus Trapping.....	41
2.5.4 Drop Squeezing Dynamics and Exit Times.....	45
2.5.5 Drop “Dripping” Dynamics.....	58
2.5.6 Critical Bond Number and Steady Drop Shapes for Trapping.....	62
2.6 Concluding Remarks .....	65
2.7 Acknowledgements.....	68
3 Trapping of a deformable drop in a three-dimensional constriction.....	69
3.1 Introduction.....	70
3.1.1 Problem Description .....	72
3.2 Numerical Methods .....	76
3.2.1 Three-dimensional Young-Laplace Solution Approach.....	77
3.2.2 Meshing Details.....	78
3.2.3 Algorithm Details .....	78
3.2.4 Solution Details of the Drop-solid Clearances .....	79
3.4 Results.....	83
3.4.1 Interaction of the Drop and Solid .....	83

3.4.2 Effect of Constriction Shape and Tilt Angle .....	92
3.5 Concluding Remarks .....	99
4 Experimental observation of drop squeezing and trapping .....	103
4.1 Introduction.....	103
4.2 Meterials and Methods.....	104
4.3 Experiment results.....	104
4.3.1 O-ring constriction.....	106
4.3.2 Agglomerate of three, touching spheres.....	114
4.4 Sphere radius vs Bond number scaling.....	118
4.5 Concluding Remarks.....	117
5 Drops statically trapped in rings with varying contact angle.....	119
5.1 Introduction.....	119
5.2 Numerical Methods.....	120
5.3 Numerical Results.....	122
5.4 Concluding Remarks.....	126
6 Concluding Remarks and Recommendations for Future Work.....	128
6.1 Buoyancy-induced Drop Motion in an Axisymmetric Ring.....	129
6.2 Trapping of a Deformable Drop in a Three-dimensional Constriction .....	132
6.3 Experiments .....	133
6.4 Future Related Research.....	134
<b>Bibliography</b>	<b>135</b>
<b>Appendix</b>	

## Figures

### Figure

2.1: Buoyancy-driven drop squeezing through circular torus.....	18
2.2: Drop velocity vs time for $B = 0.96$ , $a/b_s = 2$ , $a_s/b_s = 3$ and $\lambda = 1$ . The solid curve is for 300 nodes on $S_d$ and 450 nonadaptive nodes on $S_p$ ; the dashed line is for 300 nodes on $S_d$ and 450 adaptive nodes on $S_p$ .....	32
2.3: Static drop shape trapped in a ring.....	34
2.4: Drop velocity vs distance from constriction with $\lambda = 4$ , $a/b_s = 1.5$ and $a_s/b_s = 1.5$ .....	39
2.5: Drop velocity vs time for three $\varepsilon = 0.004$ , $0.005$ , and $0.006$ , with $B = 0.45$ , $a_s/b_s = 3$ , $a/b_s = 1.5$ , and $\lambda = 1$ , 300 nodes on $S_d$ and 600 nodes on $S_p$ .....	42
2.6: Drop velocity for squeezing through a ring constriction with $a_s/b_s = 2.25$ , $a/b_s = 1.5$ , $\lambda = 0.8$ , and $B = 2, 1, 0.75$ , and $0.35$ ; 600 node points were used on each surface, except for $B = 0.35$ , where 300 node points were used on $S_d$ and 500 on $S_p$ .....	43
2.7: The temporal dynamics of the drop-solid spacing for squeezing through a ring constriction with $a_s/b_s = 2.25$ , $a/b_s = 1.5$ , $\lambda = 0.8$ , and $B = 2, 1, 0.75$ , and $0.35$ ; the surface discretizations are the same as in Fig. 2.6.....	44
2.8: (a) Snapshots of the drop motion through a ring constriction with $a_s/b_s = 2.25$ , $a/b_s = 1.5$ , $\lambda = 0.8$ , $B = 1$ , and 600 node points used on both surfaces $S_d$ and $S_p$ . (b) Snapshots of the drop motion leading to trapping in a ring constriction with $a_s/b_s = 2.25$ , $a/b_s = 1.5$ , $\lambda = 0.8$ , and $B = 0.35$ , and 600 and 1000 node points used on surfaces $S_d$ and $S_p$ , respectively.....	46
2.9: (a) Drop velocity and (b) drop-solid minimum spacing for drop squeezing through a ring constriction, with $a_s/b_s = 3$ , $a/b_s = 2$ , $B = 1.1$ , and $\lambda = 0.8, 2$ , and $4$ (left to right). The squeezing duration $T_s$ is shown for $\lambda = 4$ .....	48

2.10: Squeezing time vs viscosity ratio for $a_s/b_s = 3$ , $a/b_s = 2$ , and $B = 0.75, 1$ , and $2$ (top to bottom).....	49
2.11: Squeezing time vs ring cross-section-to-drop size for $a/b_s = 2$ , $\lambda = 4$ , and $B = 1.25, 1.375$ , and $1.5$ (top to bottom).....	50
2.12: Squeezing time vs resolution for $B = 0.6$ , $a/b_s = 1.5$ , $a_s/b_s = 3$ , and $\lambda = 1$ , with the total number of nodes ( $N_s$ ) distributed in the ratio 2:1 on $S_p$ and $S_d$ .....	52
2.13: Nonlinear regression for Bond number vs reciprocal of squeezing time for $a/b_s = 1.5$ , $a_s/b_s = 3$ , and $\lambda = 1$ .....	53
2.14: Determination of the power-law exponent $\alpha$ using YL for $B_c$ and BI for $T_s$ when $B < B_c$ . The circles represent simulation results for $a/b_s = 1.5$ , $a_s/b_s = 3$ , and $\lambda = 1$ , and the squares represent simulation results for $a/b_s = 1.5$ , $a_s/b_s = 1$ , and $\lambda = 1$ .....	54
2.15: Steady-state trapped drop shapes for (a) $a_s/b_s = a/b_s = 2.5$ and $B = 0.001$ (dotted line), $0.5$ (solid line), and $1.584$ (dashed line); (b) $a_s/b_s = a/b_s = 2$ and $B = 0.001$ (dotted line), $0.7$ (solid line), and $1.025$ (dashed line); (c) $a_s/b_s = a/b_s = 1.5$ and $B = 0.001$ (dotted line), $0.3$ (solid line), and $0.482$ (dashed line); and (d) $a_s/b_s = a/b_s = 1.25$ and $B = 0.001$ (dotted line), $0.15$ (solid line), and $0.213$ (dashed line).....	57
2.16: BI dynamically calculated drop interface shapes at the time moments $t = 375$ (dashed line), $t = 750$ (dotted line), and $t = 2438$ (solid line), and (b) comparison between the BI dynamically calculated ( $t = 2438$ , squares) and the YL calculated (solid line) static drop shapes, at $B = 0.885$ , $a_s/b_s = 3$ , and $a/b_s = 2$ , with $\lambda = 1$ for the BI trial.....	59
2.17: Snapshots of drop motion for dripping around a ring with $a/b_s = 11.7$ , $a_s/b_s = 5$ , $\lambda = 1$ , $B = 3.25$ ( $B_c = 3.19$ ), with 200 nodes on $S_d$ and 400 nodes on $S_p$ .....	60
2.18: Snapshots of drop motion for dripping around a ring with $a/b_s = 3.2$ , $a_s/b_s = 0.567$ , $\lambda = 1$ , and $B = 2.2$ ( $B_c = 1.9$ ) with 200 nodes on $S_d$ and 400 nodes on $S_p$ .....	61
2.19: Critical Bond number values vs drop-to-hole ratio $a/b_s$ at cross-section-to-hole ratio $a_s/b_s = 1, 2, 3, 4$ , and $10$ (top to bottom).....	63

- 2.20: Critical Bond number vs drop-to-total ring radius for  $a_s/b_s = 0.05, 1, 5$  and  $10$  (bottom to top).  
The insets show two steady-state, slightly subcritical drop shapes for  $a_s/b_s = 5$ , with  $B = 7.35$ ,  $a/(2a_s+b_s) = 0.5545$  (top) and  $B = 2.38$ ,  $a/(2a_s+b_s) = 1.28$  (bottom).....64
- 2.21: The vertical position of wetting points  $W_1$  and  $W_2$  for  $a_s/b_s = 5$  as the critical Bond number is approached for the (a) squeezing, with  $B_c = 7.35$  and  $a/(2a_s+b_s) = 0.55$ , and (b) dripping, with  $B_c = 2.38$  and  $a/(2a_s+b_s) = 1.28$ , branches.....66
- 3.1: (a) Deformable drop settling toward spheres.  
(b) Drop trapping inside the constriction at the steady-state shape for Bond number = 1, drop-to-hole radius ratio = 2.8 and sphere-to-hole radius ratio = 2.6.....74
- 3.2: (a) Ring constriction has length parameters of the hole and cross-sectional radii  $b_s$  and  $a_s$ , respectively.  
(b) Cross section of a hyperbolic tube is represented by solid lines, and the surface is described by the quadratic equation  $\frac{x^2}{b_s^2} + \frac{y^2}{b_s^2} - \frac{z^2}{c_s^2} = 1$ ,  $b_s$  is the skirt (hole) radius and  $c_s$  is the vertical length scale.  
(c) Three non-touching spheres are described by an inscribed circular radius  $b_s$  and a sphere radius  $a_s$ .....75
- 3.3: The distance  $\delta$ , in the outward-normal direction to the drop, is between the drop surface, represented by a triangular mesh, and the solid surface, represented by a solid gray surface, with a close-up view.....80
- 3.4: Snapshots of the drop motion approaching three spheres (nearly touching) to steady-state of trapping with  $a/b_s = 2.8$ ,  $a_s/b_s = 2.6$ ,  $B = 1$  ( $B_{cr} \approx 1.45$ ) and 8640 triangles used on each surface  $S_d$  and  $S_p$ , respectively at (a)  $\tau = 2.5$ , (b)  $\tau = 6.25$ , (c)  $\tau = 10$  and (d)  $\tau = 100$ .....84
- 3.5: Snapshots of the drop motion approaching three spheres (nearly touching) for squeezing with  $a/b_s = 2.8$ ,  $a_s/b_s = 2.6$ ,  $B = 1.7$  ( $B_{cr} \approx 1.45$ ) and 8640 triangles used on each surface  $S_d$  and  $S_p$ , respectively at (a)  $\tau = 3.75$ , (b)  $\tau = 25$ , (c)  $\tau = 46.25$  and (d)  $\tau = 67.5$ .....85

3.6: The root mean square velocity of the drop surface versus simulation time using a 3-sphere constriction and the three-dimensional Young-Laplace algorithm with  $a/b_s = 2.8$  and  $a_s/b_s = 2.6$ , for  $B = 1.8, 1.7, 1.6, 1.5$  and  $1.45$  from top to bottom. Simulations using 5120 triangles for the drop surface are represented by solid lines and ones using 8640 triangles for the drop surface are represented by dashed lines.....88

Fig. 3.7: The root mean square velocity of the drop surface versus simulation time using a 3-sphere constriction and the three-dimensional boundary-integral algorithm with  $a/b_s = 2.8$  and  $a_s/b_s = 2.6$ , for  $B = 1.75, 1.7, 1.65$  and  $1.6$  from top to bottom. For  $B = 1.75$  and  $1.7$ , simulations using 5120 triangles on the drop and sphere surfaces are represented by solid lines and ones with 8640 triangles on the drop and sphere surfaces are represented by dashed lines. For  $B = 1.65$  and  $1.6$ , simulations using 11520 triangles on the drop and sphere surfaces are represented by solid lines and ones using 15360 triangles for the drop and sphere surfaces are represented by dashed lines. Of note is that for the two  $B = 1.65$  trials, the two curves are almost identical and are very hard to distinguish.....89

Fig. 3.8: Critical Bond number extrapolation from results using the three-dimensional Young-Laplace algorithm for a 3-sphere constriction with  $a/b_s = 2.8$  and  $a_s/b_s = 2.6$  and 8640 surface triangles representing the drop surface. The minimum observed root mean square velocity during each simulation versus Bond number is shown with solid circles representing simulation results and the line representing the extrapolation curve. The resulting critical Bond number determined is  $B_{cr} = 1.42 \pm 0.04$  90% CI.....90

Fig. 3.9: Critical Bond number extrapolation from results using the three-dimensional boundary-integral algorithm for a 3-sphere constriction with  $a/b_s = 2.8$  and  $a_s/b_s = 2.6$  and 8640 or 15360 surface triangles representing the drop and solid surfaces. The minimum

- observed root mean square velocity during each simulation versus Bond number is shown with solid circles representing simulation results and the line representing the extrapolation curve. The resulting critical Bond number determined is  $B_{cr} = 1.45 \pm 0.07$ .....91
- 3.10 (a): Critical Bond numbers versus the drop-to-hole ratio for multiple constrictions including a ring with  $a_s/b_s =$  , a hyperbolic tubes with  $c_s \approx 0.26$ , four spheres (touching) with  $a_s/b_s \approx 6.5$ , and three spheres (touching)  $a_s/b_s \approx 2.4$ .....94
- 3.10 (b): Critical Bond numbers versus drop-to-hole size ratio for hyperbolic tubes with  $a_s \approx 0.26$  and tilt angles  $\alpha = 0, 5, 10$  and  $25^\circ$ , from top to bottom.....95
- 3.11: The 3D YL algorithm and the highly-accurate axisymmetric YL algorithm are compared for drop shapes statically trapped in a hyperbolic tube, with solid black curves, representing the cross-section of the tube, gray surfaces representing drop shapes from the 3D algorithm, and dotted curves represents the drop contours from the axisymmetric algorithm using geometry parameters  $a/b_s \approx 3.22$  and  $c_s/b_s \approx 0.84$ , and using 8640 triangles for all the 3D drop shape calculations, also for (a)  $B = 0.5$ , (b)  $B = 1.5$  and (c)  $B = 2$  ( $B_{cr} = 2.62$ ).....95
- 3.11: Static drop shapes trapped in a hyperbolic tube, represented by solid black lines with  $a/b_s = 2.84$ ,  $c_s/b_s = 0.84$  and tilt angle  $\alpha = 25^\circ$ , and  $B = 0.5, 1$  and  $B = 2$ , with a close-up view of the  $B = 2$  case showing the triangular meshing and leading edge protruding into the hole. The critical Bond number is  $B_{cr} = 2.1$ .....97
- Fig. 3.12: Critical Bond numbers versus drop-to-hole size ratio for hyperbolic tubes with  $a_s/b_s = 0.52$  and tilt angles  $\alpha = 0, 5, 10$  and  $25^\circ$ , from top to bottom.....96
- Fig. 3.13: Critical Bond numbers versus drop-to-hole size ratio for hyperbolic tubes with  $a_s/b_s \approx 0.52$  and tilt angles " =  $0, 5, 10$  and  $25^\circ$ , from top to bottom.....98

- Fig. 3.14: Static drop shapes trapped in a hyperbolic tube, represented by solid black lines with  $a/b_s = 2.84$ ,  $c_s/b_s = 0.84$  and tilt angle  $\theta = 25^\circ$ , and  $B = 0.5, 1$  and  $B = 2$ , with a close-up view of the  $B = 2$  case showing the triangular meshing and leading edge protruding into the hole. The critical Bond number is  $B_c = 2.1$ .....100
- 4.1: The experimental agglomerate of three Spheres (touching), with a dimensional sphere radius  $a_s \approx 0.95$  cm, also from geometry  $a_s/b_s \approx 6.46$  so, consequently,  $b_s \approx 0.15$  cm.....105
- 4.2: Experimental stills of a 75% water drop squeezing through an O-ring constriction with  $a/b_s = 1.22$ ,  $a_s/b_s = 0.567$ ,  $\lambda = 0.026$ , and  $B = 0.29$ ; the successive photos were taken about 2 s apart.....108
- 4.3: Experimental stills of a 100% water drop being trapped in an O-ring constriction with  $a/b_s = 1.22$ ,  $a_s/b_s = 0.567$ ,  $\lambda = 0.013$ , and  $B = 0.21$ ; the first three drop stills were taken alone 2 s apart, and the last still was taken after a 20 s interval.....109
- 4.4: Experimental determination of the critical Bond number for different ring sizes using 100% water drops and the four different O-rings from Table 4.2: O-ring 1 with  $a_s/b_s = 0.773$  (theoretical  $B_c$  is dashed curve and triangles represent drop sizes), O-ring 2 with  $a_s/b_s = 0.864$  (theoretical  $B_c$  is solid curve and circles represent experimental drop sizes), O-ring 3 with  $a_s/b_s = 0.567$  (theoretical  $B_c$  is dotted curve and squares represent experimental drop sizes), and O-ring 4 with  $a_s/b_s = 0.444$  (theoretical  $B_c$  is dashed-dotted curve and diamonds represent experimental drop sizes). The open symbols are for drops that pass through the O-ring, the closed symbols are for drops that become trapped in the O-ring, and the  $\times$  symbols are for drop sizes where both trapping and squeezing are observed in repeated trials.....111
- 4.5: Experimental determination of the critical Bond number for three different drop phases using O-ring 3 from Table 4.2 with  $a_s/b_s = 0.567$ . The circles represent 100% water drops, the squares represent 75% water drops, the triangles are for 16% water drops, and the solid curve is the predicted critical Bond number. The open symbols are drops that pass the through the O-ring, the closed symbols are for the drops that become

trapped in the O-ring, and the $\times$ symbols are for the drop sizes where both trapping and squeezing is observed in repeated trials.....	112
4.6: Comparison of theoretical (axisymmetric YL algorithm) and experimental trapped drop interfaces for $a_s/b_s \approx 0.773$ , $a/b_s \approx 1.3$ , $\lambda \approx 0.013$ (experiment, only), and $B \approx 0.13$ , where the dotted white curve is the theoretical drop interface and the gray circles represent the 2D cross section of the torus.....	113
4.7: Experimental determination of the critical Bond number for three different drop phases using an agglomerate of three spheres from Figure 4.1 with $a_s/b_s \approx 6.46$ . The squares represent 100% water drops, the triangles represent 75% water drops, the diamonds are for 16% water drops, and the solid curve is the predicted critical Bond number from the 3D YL algorithm in Chpt. 3. The open symbols are drops that pass through the agglomerate, the closed symbols are for the drops that become trapped in the agglomerate, and the $\times$ symbols are for the drop sizes where both trapping and squeezing is observed in repeated trials.....	115
4.8: A deformable drop statically trapped in an agglomerate of three spheres with $a_s/b_s \approx 6.46$ , $a/b_s \approx 3.65$ and $B \approx 2.0$ using the 75% water phase for the drop.....	116
5.1: The Critical Bond number vs the drop-to-hole radius ratio for rings with $a_s/b_s = 3$ , and contact angles of $180^\circ$ , $175^\circ$ , $165^\circ$ and $155^\circ$ from top to bottom.....	123
5.2: Drops trapped just below the critical Bond number in a ring with $a/b_s = 1.5$ , $a_s/b_s = 3$ and contact angles $165^\circ$ and $B = 0.376$ , $145^\circ$ and $B = 0.252$ and $135^\circ$ and $B = 0.1723$ from top to bottom.....	124
5.3: A neutrally-buoyant (Bond number $B = 0$ ) deformable drop, with arbitrary interfacial tension $\sigma$ , statically trapped in a ring constriction, where the black curves represent the drop and solid gray circles represent the cross section of the ring constriction. The drop is and the contact angle $\alpha = 127^\circ$ , the drop-to-hole radius ratio $a/b_s = 1.5$ and the solid cross-section-to-hole radius ratio is $a_s/b_s = 3$ .....	125

## Chapter 1

### Introduction

#### 1.1 Background

An emulsion is composed of two or more immiscible fluids, including an external, continuous phase and a dispersed, drop phase. The earliest research performed to understand the rheology of emulsions was primarily empirical, but with the advancement of computational resources the problem is now studied extensively using first principles. This dissertation is motivated by emulsion flows through porous media or other confined geometries with solid obstacles on boundaries. The primary research topic is on the motion of individual emulsion drops interacting with solid constrictions, under conditions when viscous forces dominate over inertia.

Most research to date has used continuum models of the porous medium and emulsion fluid. For example, Darcy's law,  $q = -(k/\mu)\nabla P$ , where  $q$ ,  $k$ ,  $\mu$  and  $\nabla P$  are the flux in units of volume per area time, the permeability, the viscosity and the pressure gradient, respectively, states that the fluid flux is proportional to the pressure gradient. The disadvantage of continuum models is that the details of microstructure of the medium are ignored and the fluid is assumed as a pseudosingle phase, with an oversimplified rheology. When the emulsion drops are much smaller than the typical constriction diameter, treating the emulsion as one continuous phase may be valid; however, when both the drops and constriction sizes are comparable in size, continuum

models fail (Kokal 1992). Moreover, continuum models are not able to address complex drop phenomena associated with emulsion flow through confined geometries, such as pore blockage by emulsion drops, circuitous flow pathways of the drops, and dynamics of drop squeezing through constrictions.

There are many applications for emulsion flows through confined geometries (i.e., packed beds, porous media, and the cardiovascular system), including food and pharmaceutical manufacturing, oil recovery, and fixed-bed catalytic reactors. Some key objectives for modeling emulsion flows through a confined geometry are determining the relationship between pressure drop and flow rate of each phase and determining the conditions when emulsion drops become trapped in the throats of the constriction pathways.

A prototype problem for studying emulsion flow through confined geometries, related to the present research, is the pressure-driven creeping flow of a liquid containing a freely suspended, deformable drop or bubble through a channel, with or without a constriction. When the drop diameter is comparable to the channel diameter, the channel walls affect the drop shape and motion. Most research to date on this problem has been on drop breakup, rather than on drop trapping. Drop breakup in a constricted capillary tube has been studied and observed by both experimental and computational methods for large capillary numbers, which is a dimensionless ratio of viscous to interfacial forces [Goldsmith & Mason (1963), Olbricht and Kung (1992), Chi (1986) and Tsai & Miksis (1994)].

The drop-breakup mechanism in a capillary tube is different than that of the one in an unbounded velocity field and is caused by a viscous jet entering the trailing end of the drop that entrains outer-phase fluid within the drop. The effects from the flow of an emulsion drop through a tube on the resistance to flow and drop deformation have been studied experimentally

and computationally [Martinez & Udell (1989) and (1990) and Olbricht and Leal (1983)]. A comprehensive literature review on the motion of a single drop through a channel is provided by Olbricht (1996). The work of Leyrat-Maurin & Barthés-Biesel (1994) was the first attempt to simulate trapping of a deformable capsule in an axisymmetric hyperbolic constriction, but difficulties were encountered with resolving near-contact, drop-wall interactions inherent in this phenomenon, which is probably a major reason the drop trapping has been studied in less detail than drop breakup.

Zinchenko and Davis (2006) simulated three-dimensional, flow-induced drop-trapping mechanisms for different interparticle constrictions and were able to determine the critical capillary number, below which trapping occurs, for a given set of conditions. A combination of their boundary-integral techniques, capable of resolving close drop-particle interactions, with multipole acceleration has allowed simulations of a pressure-driven flow of a periodic three-dimensional emulsion through a cubic lattice of spheres at maximum packing [Zinchenko & Davis *POF* (2008)] and a flow of many deformable, three-dimensional drops through a random granular material [Zinchenko & Davis *JCP* (2008)], with calculation of pressure-gradient/flow-rate relationships. Simulations close to trapping, though, are extremely computationally expensive, and so drop trapping was not included in this prior work [Zinchenko & Davis *POF* (2008) and *JCP* (2008)]. Moreover, a complete model for emulsion flow through a granular material needs to account for both flow-induced and buoyancy-induced squeezing and trapping mechanisms to accurately predict the relationship of flow rate to pressure drop, and there is an important difference, making gravity-induced squeezing/trapping more difficult to study. Nemer *et al.* (2004) considered two drops being pushed together due to either an external flow or buoyancy settling. The fluid-film gap between the two drops was shown to reach a steady-state

value for the flow-induced case, but it decays asymptotically to zero for the buoyancy-induced case [Nemer *et al.* (2004)]. Similar trends are expected for the fluid-film gap between a drop and a solid constriction during trapping; specifically, the gap will reach a steady-state value during flow-induced trapping [confirmed by 3D simulations of Zinchenko and Davis (2006)] but asymptotically decay to zero for buoyancy-induced trapping. Less work has been accomplished on modeling buoyancy-induced motion through constrictions because the problem is more lubrication sensitive than flow-induced squeezing, due to the smaller solid-drop spacing that occurs. Thus, it requires an algorithm with a high efficiency to accurately handle small drop-solid separations.

This dissertation considers the buoyancy-induced motion of a drop in another viscous fluid as it settles toward a solid constriction containing a hole that is smaller than the drop. Of particular interest is determining conditions under which the drop is trapped by the constriction instead of passing through the constriction. Both axisymmetric and three-dimensional constrictions are considered.

## **1.2 Drop Squeezing and Static Entrapment in an Axisymmetric Constriction**

The first major objective of this dissertation is to study the problem of buoyancy-driven squeezing and trapping of a single deformable drop in a constriction having an axisymmetric configuration (e.g., a circular torus or ring). It is motivated by 3D drop squeezing and trapping in porous media, but the axisymmetric configuration allows for much more efficient and accurate numerical calculations. Under near-critical conditions, the drop passes through the constriction with very small solid-drop separation and high resistance, making calculations challenging. The

study of this model problem allows us to elucidate some relevant aspects of buoyancy-driven emulsion squeezing through a granular material and also determine the resolution necessary to simulate buoyancy-induced slow squeezing and trapping mechanisms. An axisymmetric configuration reduces a three-dimensional problem to a two-dimensional problem and allows for much finer resolution, which is especially beneficial for buoyancy-induced drop squeezing due to the lubrication sensitivity of the problem. This simplification makes it possible to study near-critical squeezing and scaling for the squeezing time in a much greater detail than in 3D simulations[Zinchenko & Davis (2006) and (2008)]. The drop-torus geometry is also convenient for physical experiments and comparisons with theory.

Dynamical drop motion in a porous medium or other confined geometry is also important, both as a precursor to drop trapping and for conditions under which the drop deforms enough to squeeze through the constriction. The dynamics of the motion of deformable drops near solid obstacles and boundaries has been studied using boundary-integral simulations. Boundary-integral equations are derived by applying Green's theorem to change the form of the Stokes equations governing flow for Reynolds numbers (dimensionless ratio of inertial to viscous forces) approaching zero, from partial-differential equations over a volume to integrals over the boundary of the domain, including the drop interfaces. A system of algebraic equations, representing different locations on the drop surface(s), is solved for the normal component of the surface velocities, and the drop shape is updated by numerically integrating the velocities using a time-stepping routine.

Determining the critical conditions, separating the boundary between drop squeezing from drop trapping, by dynamical boundary-integral simulations is especially difficult for gravity-driven motion, because the drop motion becomes very lubrication-sensitive as the critical

conditions are approached. The near-critical, dynamical simulations require a high resolution on both the drop and solid surfaces, as well as long simulation times to accurately handle the extremely small drop-solid fluid gaps. Development of a special static algorithm, in the present research, is meaningful to avoid very costly boundary-integral calculations, and to improve the accuracy of the calculations of the critical conditions for trapping and the shapes of drops trapped in constrictions[Chi (1986) and Tsai & Miksis (1994)].

Under trapping conditions, the drop reaches a steady-state (static) shape. To solve the problem of an axisymmetric, static drop in contact with solids involves numerical integration of the Young–Laplace equation from the drop tip to the point of intersection between the drop and solid, but most research to date uses empirical information in simulations (i.e., the contact angle or the drop-solid contact area) [O’Brien (1991) and Hodges *et al.* (2004)]. Most research to date for determining the static shapes of deformable drops has been on the classical problems of a drop either resting on or hanging from a solid surface. Bashforth and Adams (1892) performed the first calculation of the axisymmetric shape of a drop, through numerical integration of the Young-Laplace equation. Rotenberg *et al.* (1983) developed a method for determining the interfacial tension and contact angle, by fitting empirical data, from either a pendant or a sessile drop, to a shape calculation, performed by numerical integration of the Young-Laplace equation.

The important, practical applications of the previous research are measurements of the interfacial tension of the fluid-fluid interface and the contact angle at the three-phase contact. Past research by Hartland & Hartley (1976) has shown that axisymmetric, drop shape calculations can achieve accuracy to within one part in a million. A paper of considerable relevance is the work of Padday (1971), who solves different axisymmetric drop profiles and uses perturbations of the profiles to determine if the shape is stable or unstable by monitoring the

energy equations for the meniscus. A practical applications of calculating static drop shapes is that they may be compared to an experimentally measured drop shape to indirectly determine surface tension or contact angle, as illustrated by Padday & Pitt (1972), Shanahan (1982) and O'Brien van den Brule (1991). Another application is determining how to remove oil drops from surfaces [Chatterjee (2002)].

A static drop trapped in a solid constriction is a prototypical model for the steady-state consequence of an emulsion settling through confined geometries such as packed beds or porous media. The important applications, related to the settling of an emulsion into solid constrictions, include drop infiltration into a highly porous surface, fixed-bed catalytic reactors and liquid-liquid separation. Of particular engineering interest is determining the critical conditions delineating the boundary between the phenomena of a drop trapping within a constriction and a drop squeezing through a constriction.

Previous related research has been performed on solving two menisci in a capillary tube. The top interface is found through fitting of empirical data, and the bottom interface is found through a coupled set of Young-Laplace equations [Chatterjee (2007)]. A major difference in the former problem and the trapping of a drop in a constriction within a porous medium is that the external fluid is disconnected in a capillary tube.

### **1.3 Drop Shapes Statically Trapped in a Three-dimensional Constriction**

The second major objective of this dissertation is to develop a method to determine drop trapping conditions and static shapes in three-dimensional (3D) constrictions. In the absence of body forces, the shape of a three-dimensional interface between two static fluids is also

described by the Young-Laplace equation. For the axisymmetric problem, the solution is reduced to solving for the contour of the drop by numerically integrating the Young-Laplace equation from the tips along the drop arc length to the wetted points, which is the three-phase contact, for both the sessile and pendant portions, and calculating the free parameters in the equations by Newton-Raphson iterations. The free parameters are found so that the pressure continuity throughout the drop and the total drop volume constraints are satisfied. Such an approach, however, cannot be generalized for 3D constrictions, for example, when the constriction is made of nonaxisymmetric objects or is tilted. It is not clear how to accurately calculate the three-phase boundaries, because the wetting points for an axisymmetric constriction become wetting curves for 3D constrictions, or to calculate cumbersome derivatives of the drop surface necessary for Newton-Raphson iterations.

Less work has been performed on solving for 3D, fluid-fluid interfaces, but work by Brown *et al.* (1980) determined the shape of a 3D drop resting on an inclined plane, through use of a finite-element solution for the Young-Laplace equations along with empirical data for the wetted area of drop-solid contact [Brown *et al.* 1980]. The present goal is determination of trapping conditions and shapes without requiring empirical data.

## **1.4 Dissertation Approach**

The focus of this dissertation is elucidating the lubrication-sensitive behavior of buoyancy-induced motion of deformable emulsion drops through tight constrictions. Both dynamic simulations, using necessary numerical techniques to improve the accuracy of boundary-integral calculations, and static simulations using the Young-Laplace equation are performed to

understand the behavior of drop squeezing and trapping, respectively in solid constrictions. Also, experiments were performed to validate the results obtained in the numerical simulations. For an axisymmetric geometry, an additional problem studied is how the contact angle at the three-phase boundary affects the shape and critical conditions for static drop trapping.

Chapter 2 describes the dynamics of a single drop settling through an axisymmetric ring constriction using boundary-integral methods. The algorithm uses the Hebeker representation for the solid-particle contribution, and a high-order, near-singularity subtraction technique, which are both essential for near-critical squeezing. For a large dynamic parameter space, the average drop velocity and minimum drop-solid clearance are monitored versus time, to observe the effects of changing ring cross section and hole sizes, the fluid viscosity ratio, and Bond number, where the latter is the ratio of the gravitational and interfacial forces. The critical Bond number may be determined by extrapolation of the squeezing times from dynamic boundary-integral simulations, which requires a large number of trials and long simulation times. Instead, an axisymmetric, static algorithm combines two Young-Laplace interface solutions with a single drop-solid interface, and iteratively solves for the complete steady-state shape by employing volume and pressure continuity constraints. This method has high accuracy and is efficiently able to calculate statically-trapped drop shapes and critical Bond numbers. A major advantage of this algorithm is that no a priori, empirical knowledge is needed to determine the drop shapes. The trends of the geometric parameters versus the critical Bond number are studied in detail, and the drop-to-hole radius ratio is determined to be the most important factor affecting the conditions demarcating trapping and squeezing.

For Chapter 3, statically-trapped drop shapes for three-dimensional constrictions are calculated using a novel “time-dependent” process. The solution method uses a specifically

tailored artificial velocity function to advance the drop surface until the drop-fluid interface satisfies the Young-Laplace equation and the drop shape conforms to the solid surface in the area of near contact. It is also of importance to note that the algorithm does not need prior empirical knowledge, because the designed, artificial “velocity” automatically determines the drop-solid contact area. The 3D algorithm also determines critical Bond numbers through extrapolation for many constriction types, including rings, hyperbolic tubes and agglomerates of three or four spheres. Again, the drop-to-hole size is determined to be the most important factor affecting the critical Bond number. Interestingly, increasing the tilt of the constriction decreases the critical Bond number, perhaps because the minimum horizontal hole in a plane normal to the isolated drop motion increases. It has been observed that the type of constriction (e.g., ring versus hyperbolic tube) has only a weak effect on the critical Bond number. Importantly, for validation of the novel method, static drop shapes and critical Bond numbers show excellent agreement between the axisymmetric and three-dimensional algorithms, and static drop shapes show good agreement between the dynamic 3D boundary-integral methods and the 3D Young-Laplace solution methods.

Chapter 4 verifies the simulations in Chapters 2 and 3 by describing experiments for a deformable drop settling through an axisymmetric ring or a 3D constriction formed by three spheres joined together. Drop stills at successive time intervals illustrate the differences between the dynamics of drop squeezing through the constriction and the approach to the steady state of a trapped drop. Also, by varying the size of drops for a given constriction, critical Bond number intervals are presented that are in good agreement with calculations from the axisymmetric and 3D Young-Laplace algorithms.

Chapter 5 describes how to solve, for axisymmetric geometries, the statically-trapped drop

shapes with an arbitrary contact angle. This study presents the trends of the critical Bond number versus the contact angle. The drop shapes for a partially wetting drop are quite different than the shapes of “nonwetting” drops. For example, the static shape of a partially wetting drop may have a pendant, or sessile, wetting point below the center of the hole. Since this observation was never observed for “nonwetting” drops, it suggests that a different mechanism is possible for partially wetting drops for the loss of the steady-state of drop trapping.

In Chapter 6, concluding remarks are given to discuss the key findings for both the theoretical and experimental studies. Future research is recommended that extends upon and/or is related to the present dissertation.

## Chapter 2

### **Buoyancy-induced squeezing of a deformable drop through an axisymmetric ring constriction**

This chapter was adapted from a publication in the *Physics of Fluids* [Ratcliffe *et al.* (2010)]

#### **Abstract**

Axisymmetric boundary-integral (BI) simulations were made for buoyancy-induced squeezing of a deformable drop through a ring constriction. The algorithm uses the Hebecker representation for the solid-particle contribution. A high-order, near-singularity subtraction technique is essential for near-critical squeezing. The drop velocity and minimum drop-solid spacing were determined for different ring and hole sizes, viscosity ratios, and Bond numbers, where the latter is a dimensionless ratio of gravitational to interfacial forces. The drop velocity decelerates typically 100-fold or more, and the drop-solid spacing reduces to typically 0.1%–1% of the nondeformed drop radius as the drop passes through the constriction. The critical Bond number (below which trapping occurs) was determined for different conditions. For supercritical conditions, the nondimensional time required for the drop to pass through the ring increases for a

fixed drop-to-hole size with increasing viscosity ratio and decreasing Bond number, but it has a nonmonotonic dependence on the ratio of the radii of the drop and ring cross section. Numerical results indicate that the square of the drop squeezing time is inversely proportional to the Bond number minus the critical Bond number for near-critical squeezing. Another dynamic phenomenon, in addition to drop squeezing, is a drop “dripping” around the outer edge of the ring constriction. The initial stages of drop dripping are numerically simulated using a boundary-integral method for slightly supercritical Bond numbers. For very large ratios of the drop-to-hole radii, however, a sharp maximum in the critical Bond number is reached, as there is a transition from the drop passing through the inside hole to dripping over the outside edge of the ring for Bond numbers above the critical value.

## 2.1 Introduction

Emulsion flows through confined geometries (i.e., packed beds or porous media) have many important applications including food and pharmaceutical manufacturing, oil recovery, and fixed-bed catalytic reactors. The key objectives for modeling emulsion flows through a confined geometry are determining the relationship between pressure drop and flow rate of each phase and determining the conditions when emulsion drops become trapped in the throats of the constriction pathways. Most research to date has used continuum models of the porous medium and emulsion fluid, which ignore microstructure details of the medium and treat the fluid as a pseudosingle phase with oversimplified rheology. When the emulsion drops are much smaller than the typical constriction diameter, treating the emulsion as one continuous phase may be valid; however, when the emulsion drops have a comparable size to the typical constriction

diameter, continuum models fail [Kokal (1992)]. Moreover, continuum models are not able to address complex phenomena associated with emulsion flow through confined geometries, such as pore blockage by emulsion drops, circuitous flow pathways of the drops, and dynamics of drop squeezing through constrictions.

One prototype problem for studying emulsion flow through confined geometries is the pressure-driven creeping flow of a liquid containing a freely suspended, deformable drop or bubble through a channel, with or without constriction. When the drop diameter is comparable to the channel diameter, the drop shape and motion are affected by the channel walls. Drop breakup in a constricted capillary tube has been studied and observed by both experimental and computational methods for large capillary numbers ( $Ca = \mu U / \sigma$ , where  $\mu$ ,  $U$ , and  $\sigma$  are the external fluid viscosity, drop velocity, and interfacial tension between the drop and the external fluid, respectively [Goldsmith & Mason (1963), Olbricht & Kung (1992), Chi (1986) and Tsai & Miksis (1994)]. The drop-breakup mechanism in a capillary tube is different than that in an unbounded velocity field and is caused by a viscous jet entering the trailing end of the drop that entrains outer-phase fluid within the drop. The effects from the flow of an emulsion drop through a tube on the resistance to flow and drop deformation has been studied experimentally and computationally [Martinez & Udell (1989) and (1990) and Olbricht and Leal (1983)]. A comprehensive literature review on the motion of a single drop through a channel is found in Olbricht (1996). The work of Leyrat-Maurin and Barthés-Biesel (1994) was the first attempt to simulate trapping of a deformable capsule in an axisymmetric hyperbolic constriction, but difficulties were encountered with resolving near-contact, drop-wall interactions inherent in this phenomenon.

Zinchenko & Davis (2006) simulated three-dimensional (3D), flow-induced drop-trapping

mechanisms for different interparticle constrictions and were able to determine the critical  $Ca$ , below which trapping occurs, for a given set of conditions. A combination of their boundary-integral techniques, capable of resolving close drop-particle interactions, with multipole acceleration has allowed simulations of a pressure-driven flow of a periodic 3D emulsion through a cubic lattice of spheres at maximum packing [Zinchenko & Davis *POF* (2008)] and a flow of many deformable 3D drops through a random granular material [Zinchenko & Davis *JCP* (2008)], with calculation of pressure-gradient/flow-rate relationships; simulations close to trapping, though, are extremely difficult. One limitation of the prior studies [Zinchenko & Davis *POF* (2008) and *JCP* (2008)] is that a complete model for emulsion flow through a granular material needs to account for both flow-induced and buoyancy-induced squeezing and trapping mechanisms to accurately predict the relationship of flow rate to pressure drop, and there is an important difference, making gravity-induced squeezing/trapping more difficult to study. Nemer *et al.* (2004) considered two drops being pushed together due to either an external flow or buoyancy settling. The fluid-film gap between the two drops was shown to reach a steady-state value for the flow-induced case but decay asymptotically to zero for the buoyancy-induced case.<sup>14</sup> Similar trends are expected for the fluid-film gap between a drop and a solid constriction during trapping; specifically, the gap will reach a steady-state value during flow-induced trapping [confirmed by 3D simulations of Zinchenko & Davis (2006)] but asymptotically decay to zero for buoyancy-induced trapping. Less work has been accomplished on modeling buoyancy-induced motion through constrictions because the problem is more lubrication sensitive than flow-induced squeezing due to the smaller solid-drop spacing that occurs and requires an algorithm with a high level of resolution.

## 2.2 Formulation of the Problem

In the present work, we study the problem of buoyancy-driven squeezing of a single deformable drop through a constriction (circular torus or ring) in an axisymmetric configuration. It is motivated by 3D drop squeezing and trapping in porous media, but the axisymmetric configuration allows for much more efficient numerical calculations. Under near-critical conditions, the drop passes through the constriction with very small solid-drop separation and high resistance, making calculations challenging. The study of this model problem allows us to elucidate some relevant aspects of buoyancy-driven emulsion squeezing through a granular material and also determine the resolution necessary to simulate buoyancy-induced slow squeezing and trapping mechanisms. An axisymmetric configuration reduces a 3D problem to a two-dimensional (2D) problem and allows for much finer resolution, which is necessary for buoyancy-induced drop squeezing due to the lubrication sensitivity of the problem. This simplification makes it possible to study near-critical squeezing and scaling for the squeezing time in a much greater detail than in 3D simulations [Zinchenko & Davis (2006) and *POF* (2008)]. The drop-torus geometry is also convenient for physical experiments and comparisons with theory.

The ring constriction is held stationary in the bulk-phase Newtonian fluid, which is an unbounded, quiescent medium. The drop motion has a negligibly small Reynolds number, and both the constriction geometry and fluid motion are symmetric around the vertical  $z$ -axis. (As shown in Figure 2.1), the two parameters that describe the geometry of the ring torus are the ring cross-sectional radius  $a_s$  and the hole radius  $b_s$ . A constant interfacial tension  $\sigma$  between the drop and the external medium is assumed (no surfactants). It is also assumed that the bulk-phase fluid wets the ring so that there is always a film of this fluid between the drop interface and the solid

surface. The nondimensional parameters that affect the drop squeezing characteristics, the drop velocity in the throat, the solid-drop gap thickness, and the squeezing time  $T_s$ , are the Bond number ( $B = \Delta\rho g a^2 / \sigma$ , where  $g$  is the gravitational acceleration and  $\Delta\rho = \rho_d - \rho_e$  is the density difference), viscosity ratio ( $\lambda = \mu_d / \mu_e$ ), cross-section-to-hole radius ratio ( $a_s / b_s$ ), and drop-to-hole radius ratio ( $a / b_s$ ). The squeezing time  $T_s$  is defined explicitly as the interval between the moment when the leading drop edge is level with the torus top and the moment when the trailing drop edge becomes level with the torus bottom. Critical Bond numbers, below which trapping occurs, are accurately determined for different conditions. The calculations show the squeezing dynamics, including drop velocity and minimum solid-drop spacing trends inside the constriction, and the critical Bond number ( $B_c$ ), below which trapping occurs. The high-order, near-singularity subtraction technique developed in the work by Zinchenko and Davis (2006) is modified for the axisymmetric algorithm, allowing for simulations of near-critical squeezing. One important goal of this work is to determine the scaling for the squeezing time, as  $B \rightarrow B_c$ . Also, we developed an alternative and highly efficient static algorithm for subcritical Bond numbers based on the Young–Laplace equation, capable of calculating trapped drop shapes and the critical squeezing conditions (See Ch. 3).

### 2.3 Boundary-integral Algorithm

An axisymmetric boundary-integral (BI) formulation simulates the drop deformation and velocity as it passes through the constriction. BI methods are useful for objects with varying shape because they reduce the problem to solving for the velocity on the surfaces. An axisymmetric geometry allows the surface integrals to be further reduced to contour integrals,

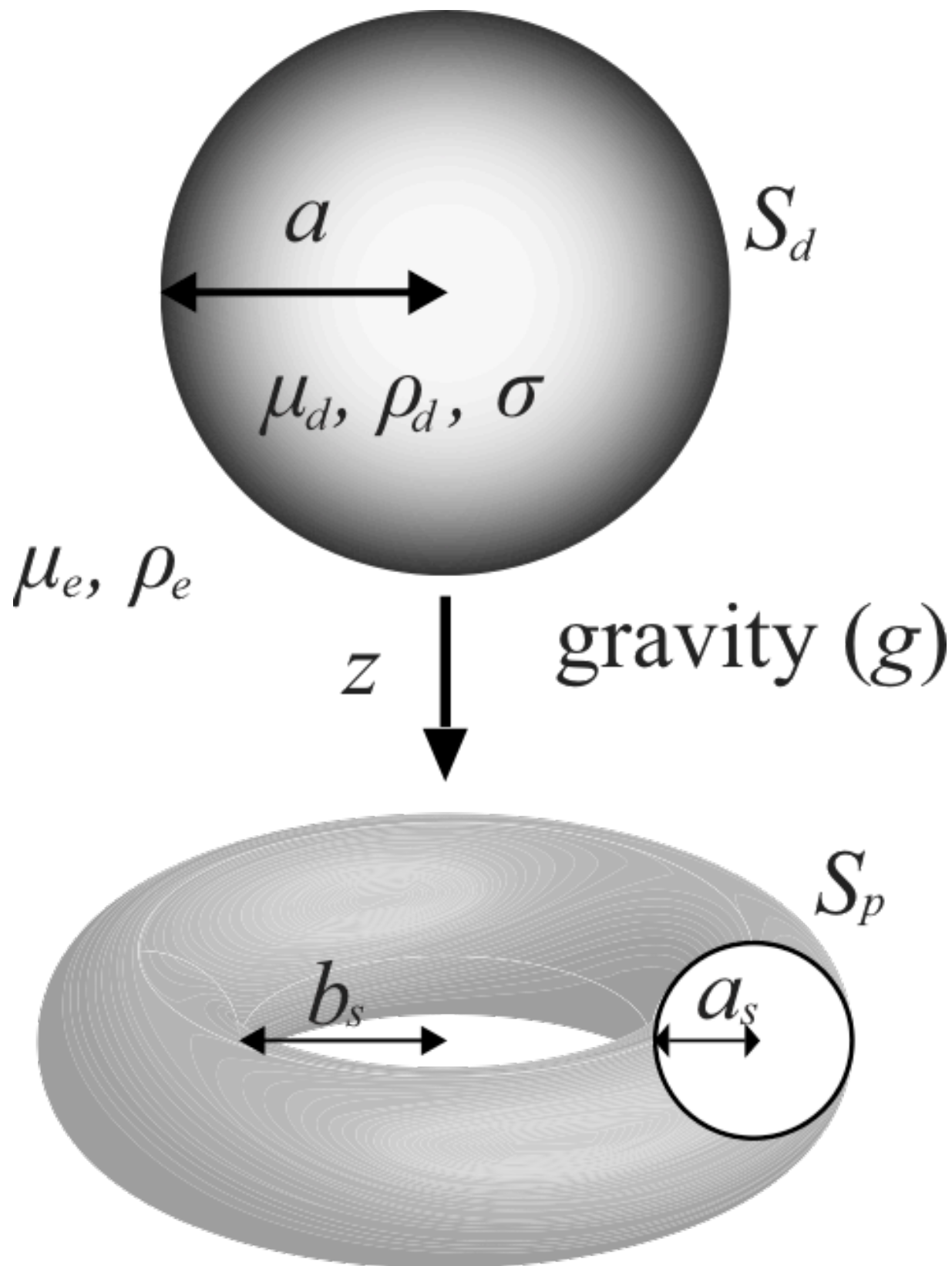


Figure 2.1: Buoyancy-driven drop squeezing through circular torus.

allowing for a much finer resolution than in 3D algorithms. Unless noted otherwise, lengths [Rallison & Acrivos (1978), Lee & Leal (1982), Davis (1999) and Pozrikidis (1992)], velocities and times are nondimensionalized by the undeformed drop radius  $a$ , the isolated drop settling velocity,  $U_0=2(\lambda+1)\Delta\rho ga^2/[3\mu_e(3\lambda+2)]$ , and the length-to-velocity ratio  $a/U_0$ .

### 2.3.1 Formulation

By combining previous ideas for a solitary drop [Rallison & Acrivos (1978)] and a single solid particle [Hebeker (1986)], a system of second-kind integral equations is derived based on the Green's function,

$$\mathbf{G}(\mathbf{r}) = -\frac{1}{8\pi} \left[ \frac{\mathbf{I}}{r} + \frac{\mathbf{r}\mathbf{r}}{r^3} \right], \quad (2.1)$$

where  $\mathbf{r} = \mathbf{x} - \mathbf{y}$  (integration minus observation vector), and its associated stress tensor (fundamental stresslet),

$$\boldsymbol{\tau}(\mathbf{r}) = \frac{3}{4\pi} \frac{\mathbf{r}\mathbf{r}\mathbf{r}}{r^5}. \quad (2.2)$$

The equations for the internal and external velocities are related by taking the limits as the observation point approaches the drop ( $S_d$ ) or constriction ( $S_p$ ) surface and applying the boundary conditions, including velocity continuity at the drop surface, stress jump condition across  $S_d$ , velocity and stress equal to zero far away from both surfaces, and no-slip on  $S_p$ . The fluid velocity  $\mathbf{u}$  at location  $\mathbf{y}$  outside of the drop interface and the torus can be represented as

$$\mathbf{u}(\mathbf{y}) = (\lambda - 1) \int_{S_d} \mathbf{u}(\mathbf{x}) \cdot \boldsymbol{\tau}(\mathbf{r}) \cdot \mathbf{n}(\mathbf{x}) dS_x + SPC(\mathbf{y}) + \mathbf{F}(\mathbf{y}), \quad (2.3)$$

where

$$\mathbf{F}(\mathbf{y}) = \frac{1}{\mu_e} \int_{S_d} f(\mathbf{x}) \mathbf{n}(\mathbf{x}) \cdot \mathbf{G}(\mathbf{r}) dS_x, \quad (2.4)$$

$$f(\mathbf{x}) = 2\sigma k(\mathbf{x}) - \Delta\rho g z, \quad (2.5)$$

$k(\mathbf{x})$  is the mean surface curvature at location  $\mathbf{x}$  on  $S_d$ , and  $\mathbf{n}(\mathbf{x})$  is the outward unit normal at  $\mathbf{x}$  on  $S_d$  or  $S_p$ .

The presence of a solid, stationary constriction creates an additional boundary-integral term, **SPC** (for “solid-particle contribution”),

$$\mathbf{SPC}(\mathbf{y}) = \int_{S_d} \left[ \frac{1}{\mu_e} \mathbf{G}(\mathbf{r}) \cdot \mathbf{T}^e(\mathbf{x}) \cdot \mathbf{n}(\mathbf{x}) - \mathbf{u}(\mathbf{x}) \cdot \boldsymbol{\tau}(\mathbf{r}) \cdot \mathbf{n}(\mathbf{x}) \right] dS_x \quad (2.6)$$

where  $\mathbf{T}^e(\mathbf{x})$  is the external fluid stress at integration point  $\mathbf{x}$ . The second term inside the brackets vanishes due to the no-slip boundary condition. Using the single-layer form of Eq. (2.6) for the **SPC** would lead to a system of integral equations of the second kind for  $\mathbf{u}$  on  $S_d$ , but of first kind for unknown tractions  $\mathbf{T}^e(\mathbf{x})$  on the solid boundary. Judging by our experience [Zinchenko & Davis (2006)], such an approach would be quite unsuccessful in drop squeezing problems due to ill-conditioning, especially for near-critical  $B$ , when high levels of surface discretization are required. Alternatively, representing the **SPC** term as a double-layer potential could not accommodate nonzero torque or force on the constriction.

The Hebeker representation [Hebeker (1986)] of the **SPC** is used instead in our algorithm because it is robust for calculating the slow-squeezing and trapping cases, as observed in Zinchenko & Davis (2006). Namely,  $\mathbf{SPC}(\mathbf{y})$  is sought as a combination of single- and double-layer potentials over  $S_p$ , with a proportionality factor,  $\eta > 0$ ,

$$\mathbf{SPC}(\mathbf{y}) = \int_{S_p} \mathbf{q}(\mathbf{x}) \cdot \left[ 2\boldsymbol{\tau}(\mathbf{r}) \cdot \mathbf{n}(\mathbf{x}) + \eta \mathbf{G}(\mathbf{r}) \right] dS_x, \quad (2.7)$$

where  $\mathbf{q}(\mathbf{x})$  is an unknown Hebeker density on  $S_p$ , which is determined simultaneously with the interfacial velocity  $\mathbf{u}$ . From numerical experiments, optimal convergence is achieved by

choosing a value of  $\eta \sim a/a_s$ . Wielandt's deflation is used to avoid ill-conditioning for extreme viscosity ratios  $\lambda \ll 1$  or  $\lambda \gg 1$ . The deflated velocity is related to the interfacial fluid velocity on  $S_d$  by  $\mathbf{w}(\mathbf{y}) = \mathbf{u}(\mathbf{y}) - (\lambda-1) \langle \mathbf{u} \rangle / (\lambda+1)$ , the angular brackets denoting averaging over the drop surface. Thus, the coupled system of second-kind integral equations to solve for  $\mathbf{w}$  and  $\mathbf{q}$  at each time step is

$$\mathbf{w}(\mathbf{y}) = \frac{2\mathbf{F}(\mathbf{y})}{\lambda+1} + \kappa \left[ 2 \int_{S_d} \mathbf{w}(\mathbf{x}) \cdot \boldsymbol{\tau}(\mathbf{r}) \cdot \mathbf{n}(\mathbf{x}) dS_x - \langle \mathbf{w} \rangle + \mathbf{n}(\mathbf{y}) \langle \mathbf{w} \cdot \mathbf{n} \rangle \right] + \frac{2}{\lambda+1} \mathbf{SPC}(\mathbf{y}) \quad (2.8)$$

on the drop surface ( $\mathbf{y} \in S_d$ ) and

$$\mathbf{q}(\mathbf{y}) = \mathbf{F}(\mathbf{y}) + (\lambda-1) \int_{S_d} \mathbf{w}(\mathbf{x}) \cdot \boldsymbol{\tau}(\mathbf{r}) \cdot \mathbf{n}(\mathbf{x}) dS_x + \mathbf{SPC}(\mathbf{y}) \quad (2.9)$$

on the solid surface ( $\mathbf{y} \in S_p$ ), where  $\kappa = (\lambda-1)/(\lambda+1)$  [Zinchenko & Davis (2006)]. The physical interfacial fluid velocity is calculated from the deflated velocity by

$$\mathbf{u}(\mathbf{y}) = \mathbf{w}(\mathbf{y}) + \frac{\lambda-1}{2} \langle \mathbf{w} \rangle. \quad (2.10)$$

### 2.3.2 Handling Singularities in the Integrand

In the kernels  $\mathbf{G}(\mathbf{r})$  and  $\boldsymbol{\tau}(\mathbf{r})$  found in the boundary-integral terms, singularities and near singularities are present when the observation point is near the integration point. Truly singular behavior is observed when  $\mathbf{x}$  and  $\mathbf{y}$  are on the same surface, while the second case is a characteristic of a drop in close contact to the solid surface. The (near) singularities, if untreated, would make numerical solutions extremely difficult, requiring impractically large meshes, especially for near-critical squeezing. Following mostly the work by Zinchenko and Davis (2006), various subtraction methods are used to eliminate/alleviate the singular behavior of the integrands when the observation point nears the integration surface, as outlined below.

### 2.3.2.1 Drop Self-interactions

For  $\mathbf{y}$  and  $\mathbf{x}$  on the drop surface ( $S_d$ ), the  $O(r^{-1})$  singular behavior of the integrands is removed from the integrals Eq. (2.4) and Eq. (2.8) over  $S_d$  using standard subtractions

$$\begin{aligned} \int_{S_d} f(\mathbf{x}) \mathbf{n}(\mathbf{x}) \cdot \mathbf{G}(\mathbf{r}) dS_x &= \int_{S_d} [f(\mathbf{x}) - f(\mathbf{y})] \mathbf{n}(\mathbf{x}) \cdot \mathbf{G}(\mathbf{r}) dS_x, \\ 2 \int_{S_d} \mathbf{w}(\mathbf{x}) \cdot \boldsymbol{\tau}(\mathbf{r}) \cdot \mathbf{n}(\mathbf{x}) dS_x &= 2 \int_{S_d} [\mathbf{w}(\mathbf{x}) - \mathbf{w}(\mathbf{y})] \cdot \boldsymbol{\tau}(\mathbf{r}) \cdot \mathbf{n}(\mathbf{x}) dS_x + \mathbf{w}(\mathbf{y}). \end{aligned} \quad (2.11)$$

### 2.3.2.2 Solid Self-interactions

For  $\mathbf{y}$  and  $\mathbf{x}$  on the solid surface ( $S_p$ ), singularity subtraction is also made in the integral Eq. (2.7),

$$\begin{aligned} \int_{S_p} \mathbf{q}(\mathbf{x}) \cdot [2\boldsymbol{\tau}(\mathbf{r}) \cdot \mathbf{n}(\mathbf{x}) + \eta \mathbf{G}(\mathbf{r})] dS_x &= \mathbf{q}(\mathbf{y}) + \\ \int_{S_p} [\mathbf{q}(\mathbf{x}) - \mathbf{q}(\mathbf{y})] \cdot [2\boldsymbol{\tau}(\mathbf{r}) \cdot \mathbf{n}(\mathbf{x}) + \eta \mathbf{G}(\mathbf{r})] dS_x &+ \eta \mathbf{q}(\mathbf{y}) \cdot \int_{S_d} \mathbf{G}(\mathbf{r}) dS_x. \end{aligned} \quad (2.12)$$

The final integral term in Eq. (2.12) is analytically calculated for a circular torus by expansions in toroidal harmonics [for details see the Appendix in Ratcliffe *et al.* (2010)].

### 2.3.2.3 Double-layer Drop-solid Contribution

Modifying the 3D approach of Zinchenko and Davis (2006), an axisymmetrical version of high-order near-singularity subtraction is used in the algorithm so that slow-squeezing and trapping cases can be successfully simulated. For  $\mathbf{y}$  on  $S_d$  and  $\mathbf{x}$  on  $S_p$ , the near-singular behavior  $O(r^{-2})$  in  $\boldsymbol{\tau}(\mathbf{r})$ , when  $\mathbf{y}$  is close to  $S_p$ , is removed from the double-layer part of the integrand in Eq. (2.7) by locally approximating the Hebecker density term as

$$\mathbf{q}(\mathbf{x}) \approx \mathbf{q}(\mathbf{x}_i) + \mathbf{A}x' + \mathbf{B}y' \quad (2.13)$$

The  $\mathbf{q}(\mathbf{x}_i)$  term is the Hebecker density in the mesh node  $\mathbf{x}_i$ , on the solid surface contour, closest to the observation point,  $\mathbf{y}$  (without a loss of generality,  $\mathbf{y}$  and the contour are assumed to lie in the same plane). A local intrinsic coordinate system  $(x', y', z')$  with right orientation is used for the approximation of the Hebecker density, where the point  $\mathbf{x}_i$  is the origin, the  $z'$ -axis direction is prescribed by the surface normal vector,  $\mathbf{n}(\mathbf{x}_i)$ , and the  $x'$ -axis in the meridian half-plane is tangent to  $S_p$  at  $\mathbf{x}_i$ . The coefficient  $\mathbf{A}$  is evaluated by numerical differentiation of  $\mathbf{q}(\mathbf{x})$  along the meridian at  $\mathbf{x} = \mathbf{x}_i$ , while  $\mathbf{B}$  is found exactly using the axial symmetry. The expression for  $\mathbf{A}$  is

$$\mathbf{A} = \frac{\Delta \mathbf{q}_{i+1} (x'_{i-1})^2 - \Delta \mathbf{q}_{i-1} (x'_{i+1})^2}{x'_{i+1} (x'_{i-1})^2 - x'_{i-1} (x'_{i+1})^2}, \quad (2.14)$$

where

$$\Delta \mathbf{q}_j = \mathbf{q}(\mathbf{x}_j) - \mathbf{q}(\mathbf{x}_i) \quad (2.15)$$

and

$$\mathbf{B} = \left( 0, \left. \frac{q_\rho}{\rho} \right|_{x_i}, 0 \right) \quad (2.16)$$

in the intrinsic coordinates. Here,  $x'_{i-1}$  and  $x'_{i+1}$  are the intrinsic  $x$ -coordinates of the mesh nodes adjacent to  $\mathbf{x}_i$  on the torus contour, and  $\rho$  refers to cylindrical coordinate (not to be confused with fluid density used earlier). Now, the integral (2.7) is fully desingularized as

$$\int_{S_p} \left\{ \mathbf{q}(\mathbf{x}) - \mathbf{q}(\mathbf{x}_i) - \mathbf{A}x' - \mathbf{B}y' \right\} \cdot \boldsymbol{\tau}(\mathbf{r}) \cdot \mathbf{n}(\mathbf{x}) dS_x + [\mathbf{A}\mathbf{e}'_1 + \mathbf{B}\mathbf{e}'_2] \cdot \frac{3}{4\pi} \int_{S_p} \frac{[\mathbf{r} \cdot \mathbf{n}(\mathbf{x})] \mathbf{r} \mathbf{r} \mathbf{r}}{r^5} dS_x, \quad (2.17)$$

where  $\mathbf{e}'_1$  and  $\mathbf{e}'_2$  are the unit vectors of the  $x'$ - and  $y'$ -axes, respectively. The added-back integral term,

$$\Psi(\mathbf{y}) = \frac{3}{4\pi} \int_{S_p} \frac{[\mathbf{r} \cdot \mathbf{n}(\mathbf{x})] \mathbf{r} \mathbf{r} \mathbf{r}}{r^5} dS_x, \quad (2.18)$$

is analytically calculated for a circular torus by expansion in toroidal harmonics (see the Appendix in Ratcliffe *et al.* (2010) for details). With  $\mathbf{A} = \mathbf{B} = \mathbf{0}$ , the form (2.17) would reduce to the leading-order subtraction method of Loewenberg and Hinch (1996). It was found [Zinchenko & Davis (2006)], though, that such a simpler technique, which does not completely eliminate the singularity in integrals (2.7), is insufficient in drop squeezing problems, especially for near-critical and subcritical squeezing conditions, although it works well in other applications. This conclusion was also confirmed in the present calculations; with higher-order subtraction disabled, successful drop squeezing simulations could only succeed for much higher resolutions, making runs extremely slow.

For the solid-drop single-layer contribution, a simple regularization method is used

$$\int_{S_p} \mathbf{q}(\mathbf{x}) \cdot \mathbf{G}(\mathbf{r}) dS_x = \int_{S_p} [\mathbf{q}(\mathbf{x}) - \mathbf{q}(\mathbf{x}_i)] \cdot \mathbf{G}(\mathbf{r}) dS_x + \mathbf{q}(\mathbf{x}_i) \cdot \int_{S_p} \mathbf{G}(\mathbf{r}) dS_x, \quad (2.19)$$

when  $\mathbf{y} \in S_d$ . The additional integral in Eq. (2.19), handled analytically, has already appeared in Eq. (2.12).

A leading-order subtraction could be made differently, using, instead of  $\mathbf{q}(\mathbf{x}_i)$ , the value of  $\mathbf{q}(\mathbf{x}^*)$  at the point on  $S_p$  nearest to  $\mathbf{y}$  found by interpolation. Our experience shows that such a modification, which still leaves a singular behavior of  $O(r^{-1})$  in the double-layer integrand, does not perform better than the simplest choice of  $\mathbf{q}(\mathbf{x}^*) = \mathbf{q}(\mathbf{x}_i)$  and is not a substitute for the high-order subtraction technique.

### 2.3.2.4 Single-layer Drop-solid Contribution

For the drop-solid single-layer contribution, a similar approach is used as in Eq. (2.11),

$$\int_{S_d} f(\mathbf{x}) \mathbf{n}(\mathbf{x}) \cdot \mathbf{G}(\mathbf{r}) dS_x = \int_{S_d} [f(\mathbf{x}) - f(\mathbf{x}_i)] \mathbf{n}(\mathbf{x}) \cdot \mathbf{G}(\mathbf{r}) dS_x, \quad (2.20)$$

where  $\mathbf{x}_i$  is the mesh node on  $S_d$  closest to the observation point  $\mathbf{y} \in S_p$ .

The drop-solid double-layer contribution subtraction technique is

$$\int_{S_d} \mathbf{w}(\mathbf{x}) \cdot \boldsymbol{\tau}(\mathbf{r}) \cdot \mathbf{n}(\mathbf{x}) dS_x = \int_{S_d} [\mathbf{w}(\mathbf{x}) - \mathbf{w}^*] \cdot \boldsymbol{\tau}(\mathbf{r}) \cdot \mathbf{n}(\mathbf{x}) dS_x, \quad (2.21)$$

where  $\mathbf{y} = \mathbf{x} + \mathbf{r} \in S_p$  and, following the approach of Zinchenko and Davis (2002), the subtracted quantity  $\mathbf{w}^*$  is calculated by minimizing the Euclidean norm of the discretized double-layer (2.21) after subtraction. The calculation of  $\mathbf{w}^*$  for the axisymmetric problem is discussed further in the following Sec. 2.3.4

### 2.3.3 Azimuthal Integrations

For axisymmetric creeping flow, the cylindrical components of the velocity, surface unit normal, and local mean curvature of the drop are independent of the azimuthal angle  $\varphi$ . Consequently, the surface boundary-integrals can be reduced to contour integrals in the  $\varphi = 0$  plane by analytically integrating along rings centered about the axis of symmetry. The boundary integral terms can be represented as contour integrals containing coefficient matrices produced from the analytical integration. The single-layer integrals over  $S_d$  and  $S_p$  are expressed as

$$\int_{S_d} \mathbf{G}(\mathbf{r}) \cdot \mathbf{n}(\mathbf{x}) [f(\mathbf{x}) - f(\mathbf{x}_i)] dS_x = \int_{C_d} \mathbf{M} \cdot \mathbf{n}(\mathbf{x}) [f(\mathbf{x}) - f(\mathbf{x}_i)] dl, \quad (2.22)$$

$$\int_{S_p} \mathbf{G}(\mathbf{r}) \cdot [\mathbf{q}(\mathbf{x}) - \mathbf{q}(\mathbf{x}_i)] dS_x = \int_{C_p} [\mathbf{M} \cdot \mathbf{q}(\mathbf{x}) - \mathbf{M}' \cdot \mathbf{q}(\mathbf{x}_i)] dl_x, \quad (2.23)$$

where  $\mathbf{x}_i$  is the closest node point to  $\mathbf{y}$  on an integration surface (including the case  $\mathbf{x}_i = \mathbf{y}$ ), on and  $\mathbf{M}$  and  $\mathbf{M}'$  are 2x2 matrices, and  $C_d$  and  $C_p$  are the surface traces of the drop and constriction, respectively, in the  $\varphi = 0$  half-plane. The double-layer integral over  $S_d$ , when  $\mathbf{y} \in S_d$ , is expressed as

$$\int_{S_d} \boldsymbol{\tau}(\mathbf{r}) \cdot \mathbf{n}(\mathbf{x}) \cdot [\mathbf{w}(\mathbf{x}) - \mathbf{w}(\mathbf{y})] dS_x = \int_{C_d} [\mathbf{Q} \cdot \mathbf{w}(\mathbf{x}) \cdot \mathbf{n}(\mathbf{x}) - \mathbf{Q}' \cdot \mathbf{w}(\mathbf{y}) \cdot \mathbf{n}(\mathbf{x})] dl_x, \quad (2.24)$$

and the double-layer integral over  $S_p$ , when  $\mathbf{y} \in S_p$ , is

$$\int_{S_p} \boldsymbol{\tau}(\mathbf{r}) \cdot \mathbf{n}(\mathbf{x}) \cdot [\mathbf{q}(\mathbf{x}) - \mathbf{q}(\mathbf{y})] dS_x = \int_{C_p} [\mathbf{Q} \cdot \mathbf{q}(\mathbf{x}) \cdot \mathbf{n}(\mathbf{x}) - \mathbf{Q}' \cdot \mathbf{q}(\mathbf{y}) \cdot \mathbf{n}(\mathbf{x})] dl_x. \quad (2.25)$$

For the high-order, near-singularity subtraction BI term Eq. (2.17) (when  $\mathbf{x} \in S_p$  and  $\mathbf{y} \in S_d$ ), the equation is expressed as

$$\begin{aligned} & \int_{S_p} \left\{ \mathbf{q}(\mathbf{x}) - \mathbf{q}(\mathbf{x}_i) - A\mathbf{x}' - B\mathbf{y}' \right\} \cdot \boldsymbol{\tau}(\mathbf{r}) \cdot \mathbf{n}(\mathbf{x}) dS_x = \\ & = \int_{C_p} \left\{ \mathbf{Q} \cdot \mathbf{q}(\mathbf{x}) \cdot \mathbf{n}(\mathbf{x}) - \mathbf{Q}' \cdot \mathbf{q}(\mathbf{x}_i) \cdot \mathbf{n}(\mathbf{x}) - V \cdot A \cdot \mathbf{n}(\mathbf{x}) - P \cdot B \cdot \mathbf{n}(\mathbf{x}) \right\} dl_x. \end{aligned} \quad (2.26)$$

The cylindrical components of the matrices  $\mathbf{M}$  and  $\mathbf{M}'$  and the third-rank tensors  $\mathbf{Q}$  and  $\mathbf{Q}'$  depend only on the cylindrical  $\rho$ - and  $z$ -components of  $\mathbf{x}$  and  $\mathbf{y}$  in the half-plane  $\varphi = 0$ . The components of  $\mathbf{M}$ ,  $\mathbf{Q}$ , and  $\mathbf{Q}'$  are available elsewhere [Davis (1999) and Pozrikidis (1992)]. The new matrices,  $\mathbf{M}'$ , due to singularity subtraction in the single-layer integral over the particle surface  $S_p$  are

$$M'_{\rho\rho} = \rho(I_{10} + \rho^2 I_{32} - 2\rho\rho_0 I_{31} + \rho_0^2 I_{30}), \quad (2.27a)$$

$$M'_{\rho z} = M_{\rho z} = \rho(z-z_0)(\rho I_{31} - \rho_0 I_{30}), \quad (2.27b)$$

$$M'_{zz} = M_{zz} = \rho(I_{10} + (z-z_0)^2 I_{30}), \quad (2.27c)$$

$$M'_{z\rho} = M_{z\rho} = \rho(z-z_0)(\rho I_{31} - \rho_0 I_{30}), \quad (2.27d)$$

where  $\mathbf{x} = (z, \rho)$ ,  $\mathbf{y} = (z_0, \rho_0)$ ,

$$I_{mn}(\rho, \rho_0, z-z_0) \equiv \int_0^{2\pi} \frac{\cos^n \phi}{\left[ (z-z_0)^2 + \rho^2 + \rho_0^2 - 2\rho\rho_0 \cos \phi \right]^{m/2}} d\phi = \frac{4k^m}{(4\rho\rho_0)^{m/2}} \int_0^{\pi/2} \frac{(2 \cos^2 \phi - 1)^n}{(1 - k^2 \cos^2 \phi)^{m/2}} d\phi, \quad (2.28)$$

and  $k^2 = 4\rho\rho_0 / ((z-z_0)^2 + (\rho + \rho_0)^2)$ .

The cylindrical components of the additional third-rank tensors  $\mathbf{V}$  and  $\mathbf{P}$  depend on the  $\rho$ - and  $z$ -components of  $\mathbf{x}$ ,  $\mathbf{y}$ ,  $\mathbf{x}_i$ , and  $\mathbf{n}(\mathbf{x}_i)$ . The components of  $\mathbf{V}$  due to high-order near-singularity subtraction in the double-layer integral over  $S_p$  are

$$V_{\rho\rho\rho} = \rho \left\{ \begin{array}{l} \rho^3 \rho_0 n_z^i I_{54} - [n_z^i (\rho^4 + 2\rho^2 \rho_0^2 + \rho^2 \rho_0 \rho^i) + n_\rho^i \rho^2 \rho_0 (z-z^i)] I_{53} + \\ \left\{ \rho^3 [n_z^i (2\rho_0 + \rho^i) + n_\rho^i (z-z^i)] + \rho\rho_0^2 [n_z^i (2\rho^i + \rho_0) + 2n_\rho^i (z-z^i)] \right\} I_{52} \\ - \left\{ [\rho^2 \rho_0 + \rho_0^3] [n_z^i \rho^i + n_\rho^i (z-z^i)] + n_z^i (\rho^2 \rho_0^2 + \rho^2 \rho_0 \rho^i) + n_\rho^i \rho^2 \rho_0 (z-z^i) \right\} I_{51} \\ + \rho\rho_0^2 [n_z^i \rho^i + n_\rho^i (z-z^i)] I_{50} \end{array} \right\}, \quad (2.29a)$$

$$V_{\rho\rho z} = \rho(z-z_0) \left\{ \begin{array}{l} -n_z^i \rho^3 I_{53} + \rho^2 [n_z^i (\rho^i + 2\rho_0) + n_\rho^i (z-z^i)] I_{52} \\ - \left\{ \rho_0 \rho [n_z^i \rho^i + n_\rho^i (z-z^i)] + \rho_0 [n_z^i (\rho\rho_0 + \rho\rho^i) + \rho n_\rho^i (z-z^i)] \right\} I_{51} \\ + \rho_0^2 [n_z^i \rho^i + n_\rho^i (z-z^i)] I_{50} \end{array} \right\}, \quad (2.29b)$$

$$V_{\rho z\rho} = \rho(z-z_0) \left\{ \begin{array}{l} n_z^i \rho^2 \rho_0 I_{53} - [n_z^i (\rho^3 + \rho\rho_0^2) + \rho\rho_0 (n_\rho^i (z-z^i) + n_z^i \rho^i)] I_{52} + \\ \left[ (\rho^2 + \rho_0^2) (n_\rho^i (z-z^i) + n_z^i \rho^i) n_z^i \rho^2 \rho_0 \right] I_{51} + \rho\rho_0 [n_z^i \rho^i + n_\rho^i (z-z^i)] I_{50} \end{array} \right\}, \quad (2.29c)$$

$$V_{\rho zz} = \rho(z - z_o)^2 \left\{ \begin{array}{l} -n_z^i \rho^2 I_{52} + \left[ \rho \left( n_\rho^i (z - z^i) + n_z^i \rho^i \right) + n_z^i \rho \rho_o \right] I_{51} \\ -\rho_o \left( n_\rho^i (z - z^i) + n_z^i \rho^i \right) I_{50} \end{array} \right\}, \quad (2.29d)$$

$$V_{zzz} = \rho(z - z_o)^3 \left\{ -n_z^i \rho I_{51} + \left( n_\rho^i (z - z^i) + n_z^i \rho^i \right) I_{50} \right\}, \quad (2.29e)$$

$$V_{zz\rho} = \rho(z - z_o)^2 \left\{ \begin{array}{l} n_z^i \rho \rho_o I_{52} - \left[ n_z^i (\rho^2 + \rho_o \rho^i) + \rho_o n_\rho^i (z - z^i) \right] I_{51} \\ + \left( n_\rho^i (z - z^i) \rho + n_z^i \rho \rho^i \right) I_{50} \end{array} \right\}, \quad (2.29f)$$

$$V_{z\rho z} = \rho(z - z_o)^2 \left\{ \begin{array}{l} -n_z^i \rho^2 I_{52} + \left[ n_z^i (\rho \rho_o + \rho \rho^i) + \rho n_\rho^i (z - z^i) \right] I_{51} \\ -\rho_o \left[ n_z^i \rho^i + n_\rho^i (z - z^i) \right] I_{50} \end{array} \right\}, \quad (2.29g)$$

$$V_{z\rho\rho} = \rho(z - z_o) \left\{ \begin{array}{l} n_z^i \rho^2 \rho_o I_{53} - \left[ n_z^i (\rho^3 + \rho \rho_o \rho^i + \rho \rho_o^2) + \rho \rho_o n_\rho^i (z - z^i) \right] I_{52} \\ + \left[ n_z^i (\rho^2 \rho^i + \rho^2 \rho_o + \rho_o^2 \rho^i) + (\rho^2 + \rho_o^2) n_\rho^i (z - z^i) \right] I_{51} \\ -\rho \rho_o \left[ n_z^i \rho^i + n_\rho^i (z - z^i) \right] I_{50} \end{array} \right\}, \quad (2.29h)$$

where  $\mathbf{x}_i = (z^i, \rho^i)$  and  $\mathbf{n}(\mathbf{x}_i) = (n_z^i, n_\rho^i)$  in cylindrical coordinates.

The components of  $\mathbf{P}$  due to high-order near-singularity subtraction in the double-layer over  $S_p$  are

$$P_{\rho\rho} = \rho^3 \left\{ \rho \rho_o (I_{54} - I_{50}) + (\rho^2 + \rho_o^2) (I_{51} - I_{53}) \right\}, \quad (2.30a)$$

$$P_{\rho z} = \rho^3 \left\{ \rho (z - z_o) (I_{51} - I_{53}) + \rho_o (z - z_o) (I_{52} - I_{50}) \right\}, \quad (2.30b)$$

$$P_{zz} = \rho^3 (z - z_o)^2 (I_{50} - I_{52}), \quad (2.30c)$$

$$P_{z\rho} = \rho^3 (z - z_o) \left\{ \rho (I_{50} - I_{52}) + \rho_o (I_{53} - I_{51}) \right\}. \quad (2.30d)$$

The integrals  $I_{mn}$  can be expressed [Lee & Leal (1982)] in terms of complete elliptical integrals of the first and second kind with argument  $k$ . The elliptical integrals are calculated using recursive formulas found in Pozrikidis (1992) and by asymptotic formulas ( $k \rightarrow 1$ ) found in Lee

and Leal (1982). In Eq. (2.26), the matrix operation with  $V$  is understood as  $(V \cdot \mathbf{A} \cdot \mathbf{n}) = V_{ijk} A_{jn} k$ ; similarly for the  $\mathbf{P} \cdot \mathbf{B} \cdot \mathbf{n}$  term. The free index  $l$  refers to the  $\rho$ - or  $z$ -component, and the repeated indices  $j$  and  $k$  summed over the  $\rho$ - and  $z$ -components.

Based on the same azimuthal integration as in Eq. (2.24), the integral in Eq. (2.21) is numerically approximated as

$$\sum_{x_m} (\mathbf{Q} \cdot \mathbf{w} \cdot \mathbf{n} - \mathbf{Q}' \cdot \mathbf{w}^* \cdot \mathbf{n}) \Delta l_m, \quad (2.31)$$

where  $x_m$  are the mesh nodes on the drop contour and  $\Delta l_m$  are the arc lengths associated with  $x_m$  by the trapezoidal integration rule. Accordingly, the subtracted quantities  $\mathbf{w}^*$  are required to minimize

$$\sum_{x_m} [\mathbf{Q} \cdot \mathbf{w} \cdot \mathbf{n} - \mathbf{Q}' \cdot \mathbf{w}^* \cdot \mathbf{n}]^2 (\Delta l_m)^2, \quad (2.32)$$

which gives a 2x2 system of equations for  $w_\rho^*$  and  $w_z^*$ . Using  $\mathbf{w}^*$  instead of  $\mathbf{w}(x_i)$  in Eq. (2.21) was necessary for near-critical squeezing simulations to alleviate difficulties with drop-solid overlapping in the near contact region.

### 2.3.4 Additional Numerical Details

The unit normals and curvatures on  $S_d$  were found for each node point by fitting a locally oriented parabola through it and its adjacent neighbors [Davis (1999)]. The unit normals  $S_p$  are calculated analytically.

The instantaneous drop velocity  $\mathbf{U}$  is defined as the volume-averaged fluid velocity inside the drop and is calculated using the Gauss theorem,

$$\mathbf{U} = \frac{1}{V_d} \int_{S_d} (\mathbf{u} \cdot \mathbf{n})(\mathbf{x} - \mathbf{x}_d^c) dS, \quad (2.33)$$

where  $V_d$  is the drop volume and  $\mathbf{x}_d^c$  is the drop surface centroid.

For the algorithm based on the coupled set of Eqs. (2.8) and (2.9), successive substitutions are divergent. Therefore, a minimal residual method is employed instead (the same version of the generalized minimal residual method, as in the previous calculations) [Zinchenko & Davis (2006) and (2002)].

A nonadaptive moving mesh is used on the deformable drop contour, and an adaptive stationary mesh is used on the constriction contour. Following the work of Davis (1999), a simple mesh-redistribution algorithm is used on the drop contour to eliminate mesh-node accumulation, by checking the mesh spacing every few time steps and redistributing the nodes evenly along the drop contour when necessary.

Both uniform and adaptive stationary meshing on the solid constriction were tested for the BI algorithm. For the adaptive meshing, the density of the mesh points on  $S_p$  scales with the distance to the center of the constriction raised to a power (typically  $-0.4$ , giving slightly more than twice as many node points in the interior of the constriction as the exterior). These meshings are weakly adaptive to avoid the loss of accuracy for global results including squeezing time. Next, global results are compared for the BI simulations using different meshing on  $S_p$ . In Fig. 2.2, two drop velocity curves are shown for a squeezing case, corresponding to uniform and adaptive meshes on  $S_p$ . The graph shows that the adaptive mesh provides a more stable and accurate drop velocity than does the uniform mesh.

A stable time step  $\Delta t$  is chosen as

$$\Delta t = K \frac{\mu_e}{\sigma} \min_i \left\{ \frac{\Delta x_i}{a |k(\mathbf{x}_i)|} \right\}, \quad (2.34)$$

where  $K = O(1)$  is a numerical factor and the minimum is taken over all node points,  $\mathbf{x}_i$  on  $S_d$ ,  $\Delta x_i$  is the minimum distance between  $\mathbf{x}_i$  and neighboring mesh node points,  $a$  is the nondeformed drop radius, and  $k(\mathbf{x}_i)$  is the local mean curvature at  $\mathbf{x}_i$ . The drop shape was updated using a first-order Euler method. The economical first-order time integration scheme is justified in the present calculations since the drop moves very slowly, with high resistance, through the constriction [Zinchenko & Davis (2006)].

In the BI algorithm, drop squeezing calculations near the critical  $B$  are very lubrication sensitive, with drop-to-constriction minimum gaps observed as low as 0.1%–0.01% of the undeformed drop radius. Therefore, a geometric barrier ( $\varepsilon$ , defined as the minimum drop-solid dimensionless gap allowed) is sometimes employed in the present simulations to avoid numerical drop-solid overlapping when using a lower number of surface nodes. If a drop node point  $\mathbf{x}_i$  moves closer to the constriction than a set barrier value, then the node point is pushed back along the normal  $\mathbf{n}(\mathbf{x}_i)$  to the barrier value.

It must be stressed that only a small portion (1%–2%) of the mesh nodes on the drop [near the wetting points,  $W_1$  and  $W_2$  (see Fig. 2.3), where lubrication is difficult to resolve] needed this correction, so the geometric barrier did not have an appreciable effect on the overall process of drop squeezing. Instead of the geometric barrier, we also investigated incorporation of an artificial, singular molecular repulsion term in the normal-stress balance to prevent drop-solid overlap. We performed extensive testing based on this more physical approach, but found it to be unsatisfactory. To prevent overlapping and also to have a negligible effect on the overall process of drop squeezing, the length scale of the “molecular” repulsion has to be very small, but in this range numerical instability could not be avoided.

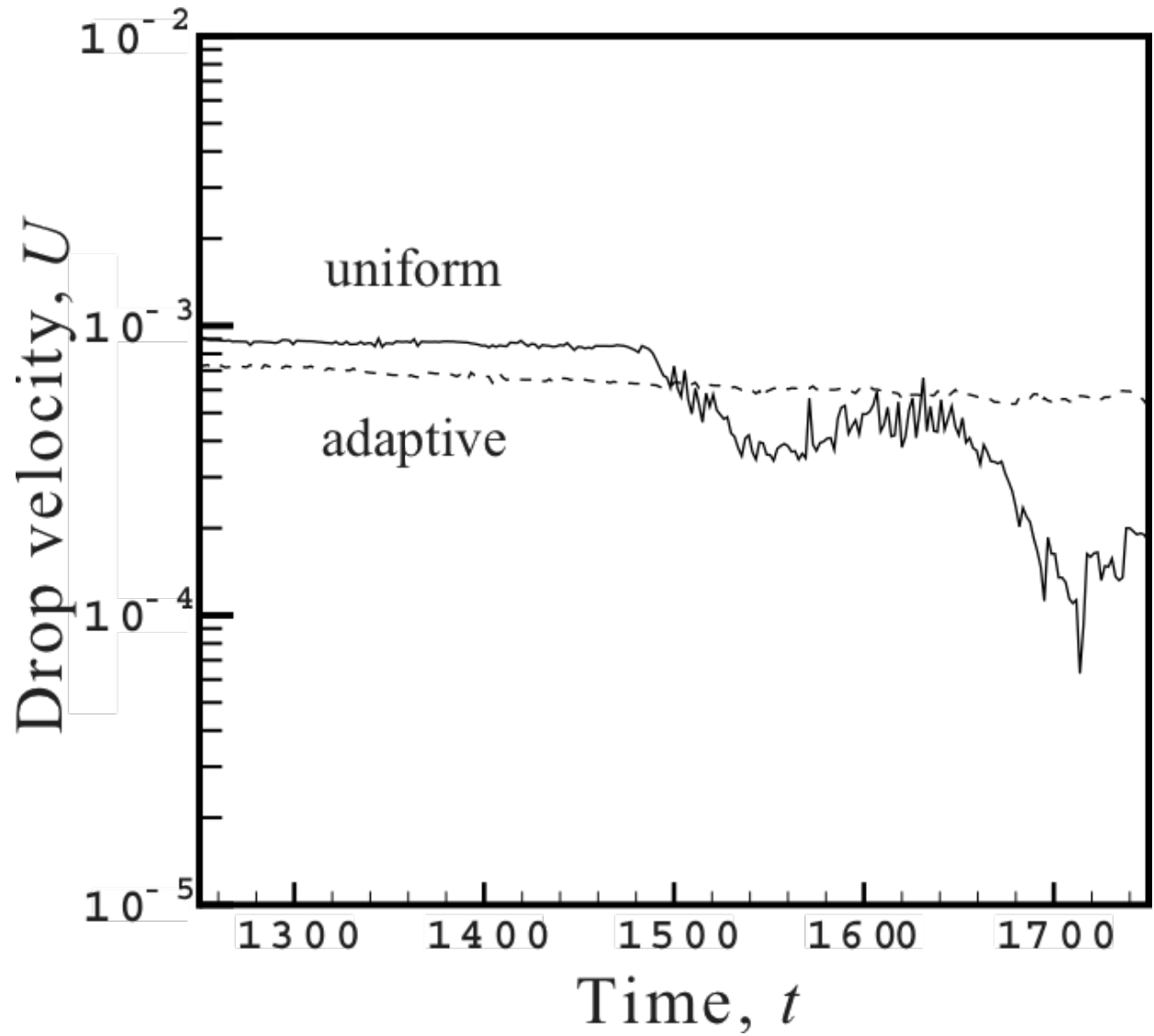


Fig. 2.2: Drop velocity vs time for  $B = 0.96$ ,  $a/b_s = 2$ ,  $a_s/b_s = 3$ , and  $\lambda = 1$ . The solid curve is for 300 nodes on  $S_d$  and 450 nonadaptive nodes on  $S_p$ ; the dashed line is for 300 nodes on  $S_d$  and 450 adaptive nodes on  $S_p$ .

## 2.4 Static Algorithm Based on the Young–Laplace Equation

In addition to the boundary-integral algorithm for a moving drop, we developed an alternative and very efficient static algorithm for subcritical Bond numbers based on the Young–Laplace (YL) equation. When  $B < B_c$  and  $t \rightarrow \infty$ , the nonwetting drop asymptotically reaches a trapped configuration to be determined, consisting of the sessile and pendant parts plus the “wetted” area in contact with the torus. In Fig. 2.3, the drop (assumed to be heavier than the surrounding fluid) rests on the torus, and the wetted area is formed by rotating the arc  $W_1W_2$  about the torus axis of symmetry; the sessile and pendant parts are tangent to the solid surface at  $W_1$  and  $W_2$ , respectively. Although axisymmetric static analysis based on the Young–Laplace equation has been widely used in literature to study equilibrium drop shapes on a plane substrate [see O’Brien (1991) and Hodges et al. (2004)], the novelty of the present case is that the sessile and pendant curves are connected through the wetted area, the solutions for the top and bottom parts are coupled, and there is a critical Bond number for squeezing to occur. Accordingly, this situation has required a new algorithm described below.

We work with two cylindrical coordinate systems  $(\rho, z_1)$  and  $(\rho, z_2)$  with the origins  $O_1, O_2$  at the drop tips (Fig. 2.3) and use the nondeformed drop radius as the length scale to nondimensionalize the equations. Indices 1 and 2 mark the values related to the sessile and pendant parts, respectively. The equilibrium condition is the Young–Laplace equation (written in terms of the Bond number),  $C_1 + Bz_1 = 2k$  (sessile part) and  $C_2 - Bz_2 = 2k$  (pendant part), where  $k$  is the local mean curvature of the drop surface. Constants  $C_1$  and  $C_2$  are yet to be determined. One obvious limitation on  $C_1$  and  $C_2$  is the total volume constraint,

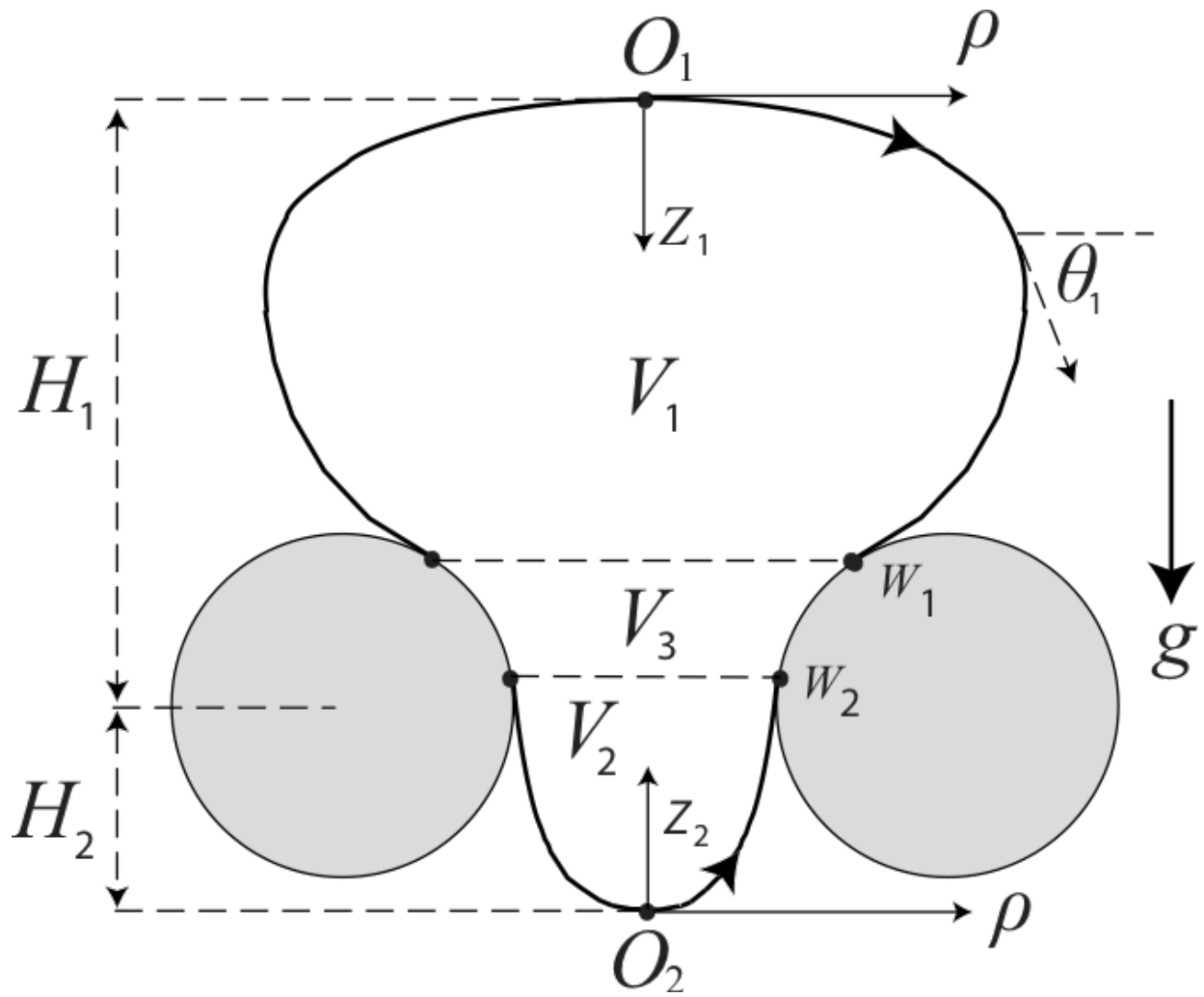


Fig. 2.3: Static drop shape trapped in a ring.

$$F_1 = V_1 + V_2 + V_3 - \frac{4\pi}{3} = 0 \quad (2.35)$$

where  $V_3$  is the (nondimensional) volume of the drop part wetting the constriction (Fig. 2.3). Since the pressures inside and outside the drop are continuous, the Young–Laplace equations for the sessile and pendant parts, if rewritten in the same coordinate system, would be identical, which gives another constraint on  $C_1$  and  $C_2$ ,

$$F_2 = C_1 + B(H_1 + H_2) - C_2 = 0 \quad (2.36)$$

where  $H_1$  and  $H_2$  are the distances from the drop tips to the plane of symmetry of the torus (Fig. 2.3). If  $O_2$  is above this plane,  $H_2$  is taken with the minus sign. The directions on the sessile and pendant parts are chosen from the tip to the corresponding wetting point, as indicated by arrows in Fig. 2.3. Let  $\theta_i (i=1,2)$  be the angle between the directional tangent vector to the sessile/pendant curve and the  $\rho$ -axis (note: only  $\theta_1$  is shown in Fig. 2.3). The solution is first constructed on the assumptions that (i) neither the sessile nor the pendant part has an inflection point, (ii)  $\theta_1 = \theta_1^* > \pi/2$  at  $W_1$ , and (iii)  $\theta_2 = \theta_2^* < \pi/2$  at  $W_2$ . All these assumptions [(ii) is self-evident] are obviously true at  $B = 0$ , when the spherical drop rests on the torus and  $W_1 = W_2$ . It turns out, however (see below), that the same holds for *all* subcritical Bond numbers. The Young–Laplace equation yields the differential equations for the sessile and pendant parts [O’Brien (1991)],

$$\frac{d\rho}{d\theta_i} = \frac{\rho \cos\theta_i}{\rho(C_i \pm Bz_i) - \sin\theta_i}, \quad \frac{dz_i}{d\theta_i} = \frac{\rho \sin\theta_i}{\rho(C_i \pm Bz_i) - \sin\theta_i}, \quad (2.37)$$

where the plus and minus signs are taken for  $i = 1$  and  $2$ , respectively; for convex shapes, the denominator in Eq. (2.37) is always positive. Eq. (2.37) is complemented by asymptotic initial conditions at  $\theta_i \rightarrow 0$ , derived from Eq. (2.37) by Taylor expansion,

$$\rho = \frac{2}{C_i} \theta_i - \left( \frac{1}{3C_i} \pm \frac{B}{C_i^3} \right) \theta_i^3 + O(\theta_i^5), \quad z_i = \frac{1}{C_i} \theta_i^2 - \left( \frac{1}{12C_i} \pm \frac{3B}{4C_i^3} \right) \theta_i^4 + O(\theta_i^6). \quad (2.38)$$

Since the drop surface is tangent to the torus at the wetting points, we have

$$\rho = a_s + b_s - a_s \sin \theta_i \quad \text{at } \theta_i = \theta_i^*. \quad (2.39)$$

The algorithm works in the following manner. With an initial guess  $(C_1, C_2)$ , Eqs. (2.37) are integrated numerically from sufficiently small  $\theta_i$  using the asymptotic initial condition (2.38), until Eq. (2.39) is satisfied; for the sessile-part integration, the first root of Eq. (2.39) with  $\theta_1 < \pi/2$  is skipped. These integrations give  $\theta_i^*(C_i)$ ,  $V_i(C_i)$ ,  $H_i(C_i)$ , and  $V_3(C_1, C_2)$  and allow us to formulate (2.35) and (2.36) as systems of equations  $F(C) = \mathbf{0}$  for  $C_1$  and  $C_2$ . In addition to  $\rho(\theta_i, C_i)$  and  $z(\theta_i, C_i)$ , the derivatives  $\partial\rho/\partial C_i$ ,  $\partial z/\partial C_i$ , and  $d\theta_i^*/dC_i$  are calculated from an extended system of equations, obtained by differentiating Eqs. (2.37)-(2.39) with respect to  $C_i$ . The latter procedure, although somewhat cumbersome, allows us to calculate  $\partial F_i/\partial C_j$  and solve Eqs. (2.35) and (2.36) for  $C_1, C_2$  by Newton iterations. In numerical implementation, an explicit second-order Runge–Kutta integration with a small step  $\Delta\theta_i$  and linear interpolation for the roots of Eq. (2.39) was sufficient. With small increments in the Bond number, starting from  $B = 0$  (when  $C_1 = C_2 = 2$ ), the previous solution provides a good initial approximation for  $C_1, C_2$ , requiring just a few Newton iterations (except at the critical conditions, see below).

The critical Bond number  $B_c$  is detected with high precision as a value when the Jacobian,  $\det[\partial F_i/\partial C_j]$ , for the solution of Eqs. (2.35) and (2.36) approaches zero. Geometrically, this value of  $B$  corresponds to touching of the curves  $F_1(C_1, C_2) = 0$  and  $F_2(C_1, C_2) = 0$  so that the solution of Eqs. (2.35) and (2.36) cannot be extended beyond  $B_c$ . Our calculations show that this critical Bond number can also be characterized by  $\theta_2^* \rightarrow \pi/2$  and the wetting point  $W_2$  (Fig. 2.3) approaching the plane of symmetry of the torus. Both the sessile and pendant shapes are

observed to remain convex up to  $B = B_c$ . One can question if an equilibrium trapped state would exist for higher Bond numbers, with the wetting point  $W_2$  below the plane of symmetry and a sessile/pendant part having an inflection point. We explored such a possibility by modifying the above algorithm and using an alternative form of the Young–Laplace equation (2.37) with the arc length as an independent variable [O’Brien (1991)]. However, no solution of this kind was found to exist. So,  $B_c$  found by our static algorithm represents, indeed, the threshold for squeezing to occur, which is confirmed by the boundary-integral simulations in Sec. 2.5. Note that integrating the YL equations (2.37) from  $\theta_i = 0$  does not require knowledge of the absolute position of the tip. Also, this approach allows us to avoid nested Newton iterations (which would be inevitable, had we chosen a different direction of integration, from the wetting point to the tip). The algorithm can be generalized to other axisymmetrical problems, e.g., of a nonwetting drop trapped under gravity in the throat of a constricted tube with arbitrary cross section.

Rotenberg *et al.* (1983) used axisymmetrical analysis based on the YL equation for best fitting of the theoretical single-piece meniscus (sessile or pendant) to the experimental shape. Although their task is vastly different from ours, there are some similarities in the numerics. Both algorithms integrate YL equations from the tip(s) [with fewer terms in Rotenberg *et al.* (1983) compared to our Eq. (2.38) to start integration] and use the Bond number as a loading parameter. The task [Rotenberg *et al.* (1983)], though, requires calculating up to second derivatives of  $\rho$  and  $z$  with respect to parameters; the present algorithm is much less cumbersome.

## 2.5 Numerical Results

### 2.5.1 Testing of the BI Algorithm

The code was first tested by showing that the drop velocity far away from the constriction equals the Hadamard–Rybizynski value. The drop was placed below the constriction and allowed to settle away from it using 700 nodes on each surface. As shown in Fig. 2.4, the drop velocity (made dimensionless with the Hadamard–Rybizynski value for an isolated drop) asymptotically approaches unity. As another test, the code was modified to handle flow-induced squeezing, and the resulting calculated drag force on the ring constriction, when the drop is far away, was compared with the analytical solution for the drag force on a solitary torus rigidly held in a uniform Stokes flow [Majumdar & O’Neill (1977)]. Table 2.1 shows that the boundary-integral calculation of the hydrodynamic force calculation is accurate for multiple torus sizes to within about 0.1%. The hydrodynamic force is calculated from the BI solution as [Hebeker (1986)]

$$F_{simulation}^* = \eta \int_{torus} q dS. \quad (2.40)$$

### 2.5.2 The Effect of a Geometric Barrier on Squeezing

It is expected that increasing the size of the geometric barrier will lower the squeezing time because the drop will not approach the constriction as closely and will experience less resistance.

In Fig. 2.5, the drop velocity for squeezing of a drop with  $B = 0.45$  through a ring with geometry parameters of  $a_s/b_s = 3$  and  $a/b_s = 1.5$  is shown for three barrier values. It is observed that increasing  $\varepsilon$  speeds up squeezing, but the overall effect of varying this artificial parameter  $\varepsilon$  on the squeezing time is small. For the conditions in Fig. 2.5, not more than 6–7 drop mesh nodes, out of 300, required the geometrical correction at any time step. Overall, using the barrier can slightly lower the accuracy of the calculations, but allows for cruder resolutions and, hence,

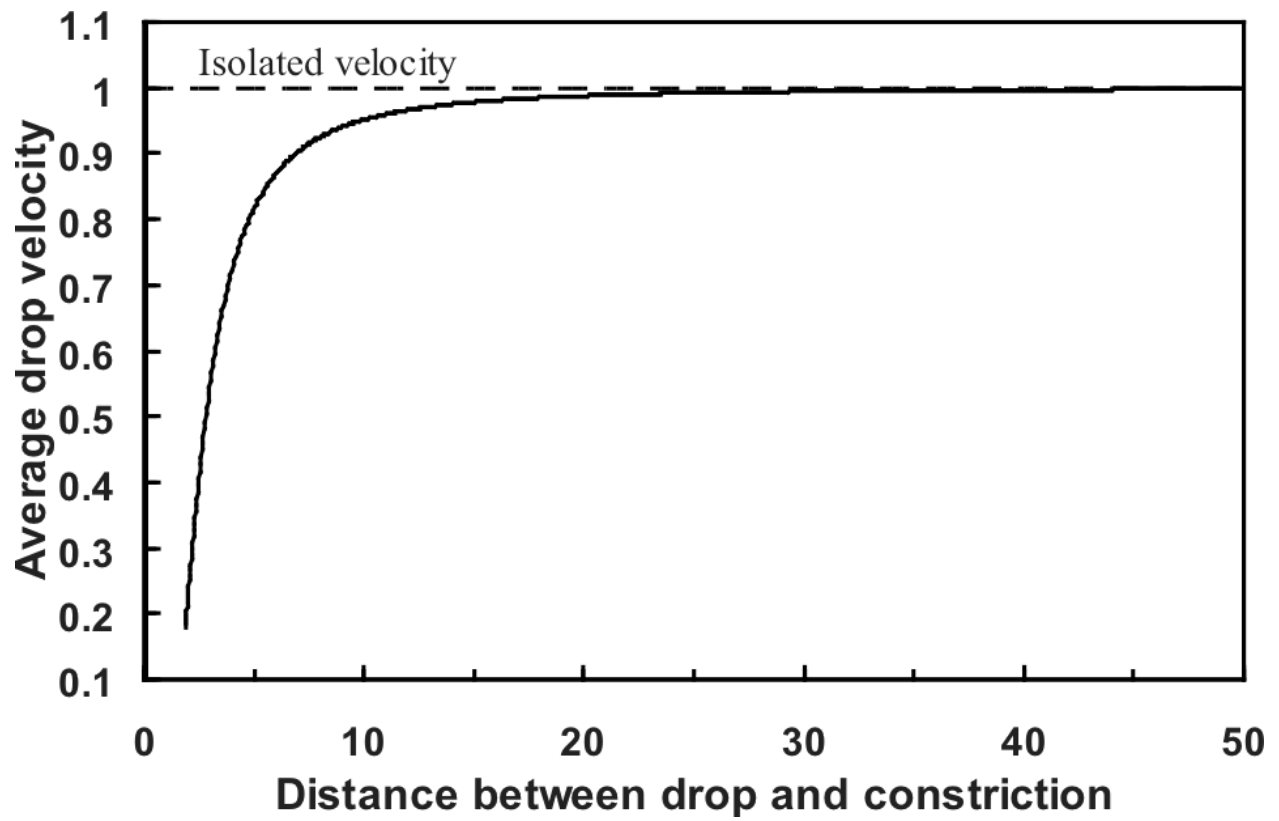


Fig. 2.4: Drop velocity vs distance from constriction with  $\lambda = 4$ ,  $a/b_s = 1.5$ , and  $a_s/b_s = 1.5$ .

Table 2.1: Comparison of the analytical solution vs boundary-integral calculation for the dimensionless hydrodynamic force on a torus held in a uniform external flow.

$1 + b_s/a_s$	<b>F*</b> analytical	<b>F*</b> simulation	<b>Percent</b> <b>error</b>
1.3	40.13	40.18	0.13
1.5	43.35	43.40	0.12
2	51.30	51.35	0.11
3	66.69	66.75	0.09
4	81.49	81.55	0.08

much faster simulations of near-critical squeezing. As the resolution increases, there is no need for this correction.

### 2.5.3 Squeezing versus Trapping

The effect of drop deformability on the squeezing and trapping process was studied by plotting the drop velocity and drop-solid spacing versus time for varying  $B$ . As shown in Figs. 2.6 and 2.7, the drop velocity and drop-solid spacing decrease as the drop penetrates the hole before increasing as the drop exits the hole. The minimum velocity and gap decrease with decreasing Bond number, as the drop becomes more difficult to deform. Accordingly, the squeezing time is larger for smaller Bond numbers. A second minimum in the drop velocity is observed just before the drop exits the constriction due to competing effects of the drop nose elongating while the drop tail is still “pinned” in the constriction (a similar behavior of the drop velocity was observed in 3D flow-induced squeezing simulations [Zinchenko & Davis 2006])). The  $B = 0.35$  run in Figs. 2.6 and 2.7 demonstrates the trapping mechanism, where both the drop velocity and drop-solid spacing asymptotically decay to zero. The critical Bond number for this geometry is  $B_c = 0.44$ , defined such that for  $B$  above this value, the drop is able to deform and slowly squeeze through the constriction. For  $B$  below the critical value, the drop becomes stuck inside the constriction and reaches a steady-state, trapped configuration.

One of the examples demonstrating the power of higher-order, near-singularity subtraction in the solid-to-drop double-layer contribution is a tight-squeezing case  $a/b_s = 1.5$ ,  $a_s/b_s = 3$ ,  $\lambda = 1$ , and  $B = 0.55$ , with the drop velocity decelerating about 100 times in the constriction. Using 300 node points on the drop and 600 points on the solid surface, pass-through was successfully simulated. In contrast, with higher-order subtraction disabled, we could not proceed beyond the initial stage, when the drop velocity decelerates to its minimum.

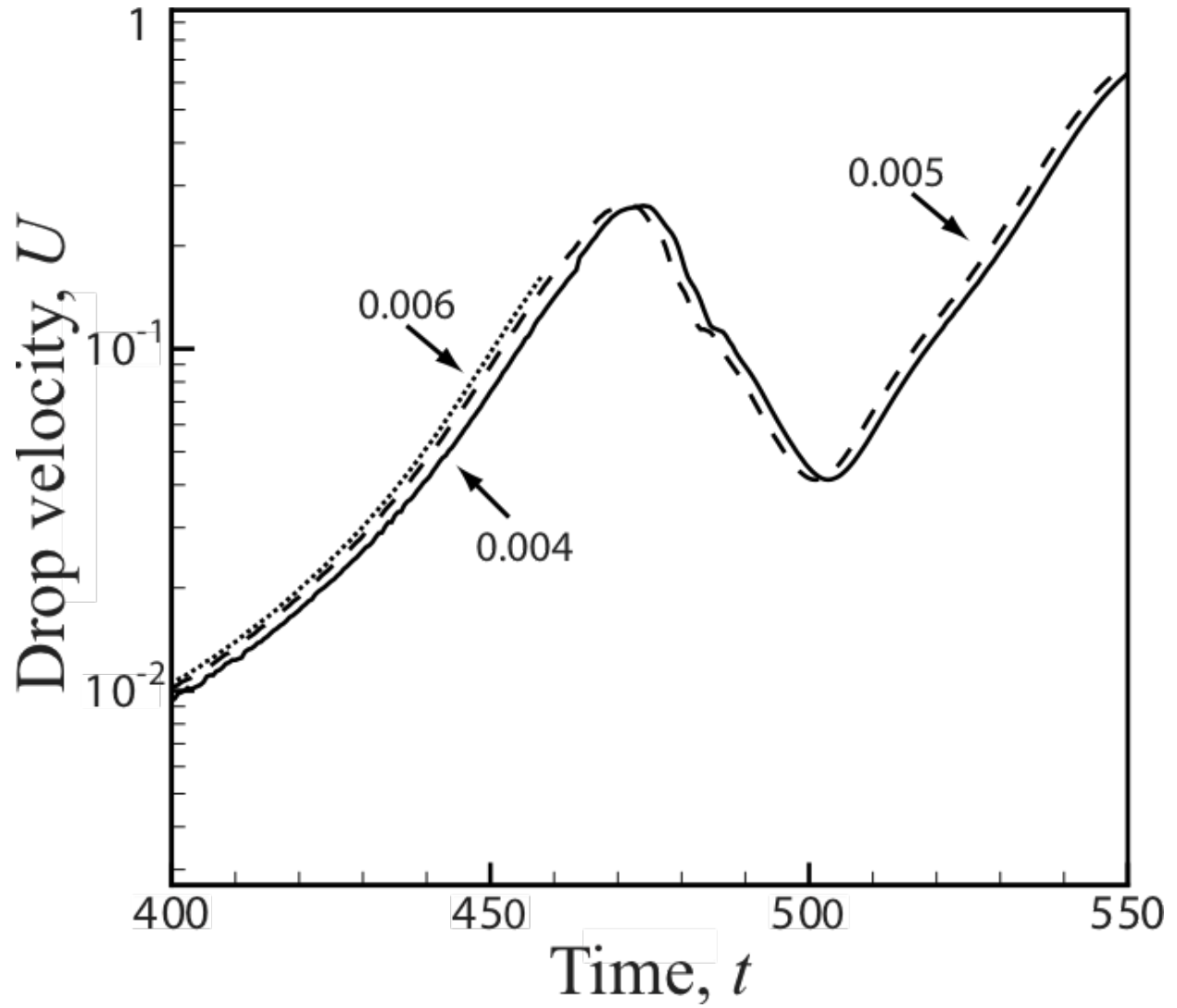


Fig. 2.5: Drop velocity vs time for three  $\varepsilon = 0.004, 0.005,$  and  $0.006$ , with  $B = 0.45, a_s/b_s = 3, a/b_s = 1.5,$  and  $\lambda = 1$ , 300 nodes on  $S_d$  and 600 nodes on  $S_p$ .

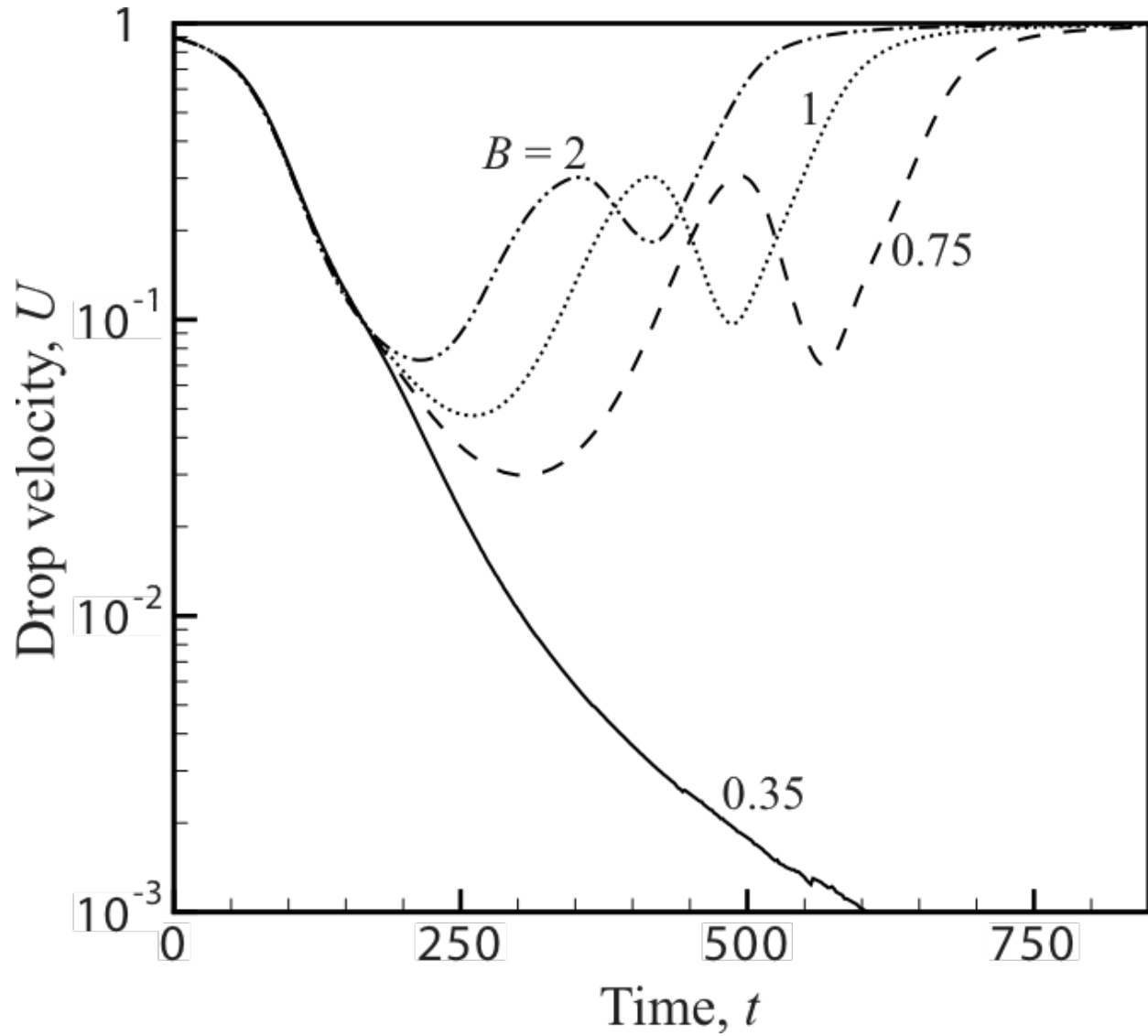


Fig. 2.6: Drop velocity for squeezing through a ring constriction with  $a_s/b_s = 2.25$ ,  $a/b_s = 1.5$ ,  $\lambda = 0.8$ , and  $B = 2, 1, 0.75$ , and  $0.35$ ; 600 node points were used on each surface, except for  $B = 0.35$ , where 300 node points were used on  $S_d$  and 500 on  $S_p$ .

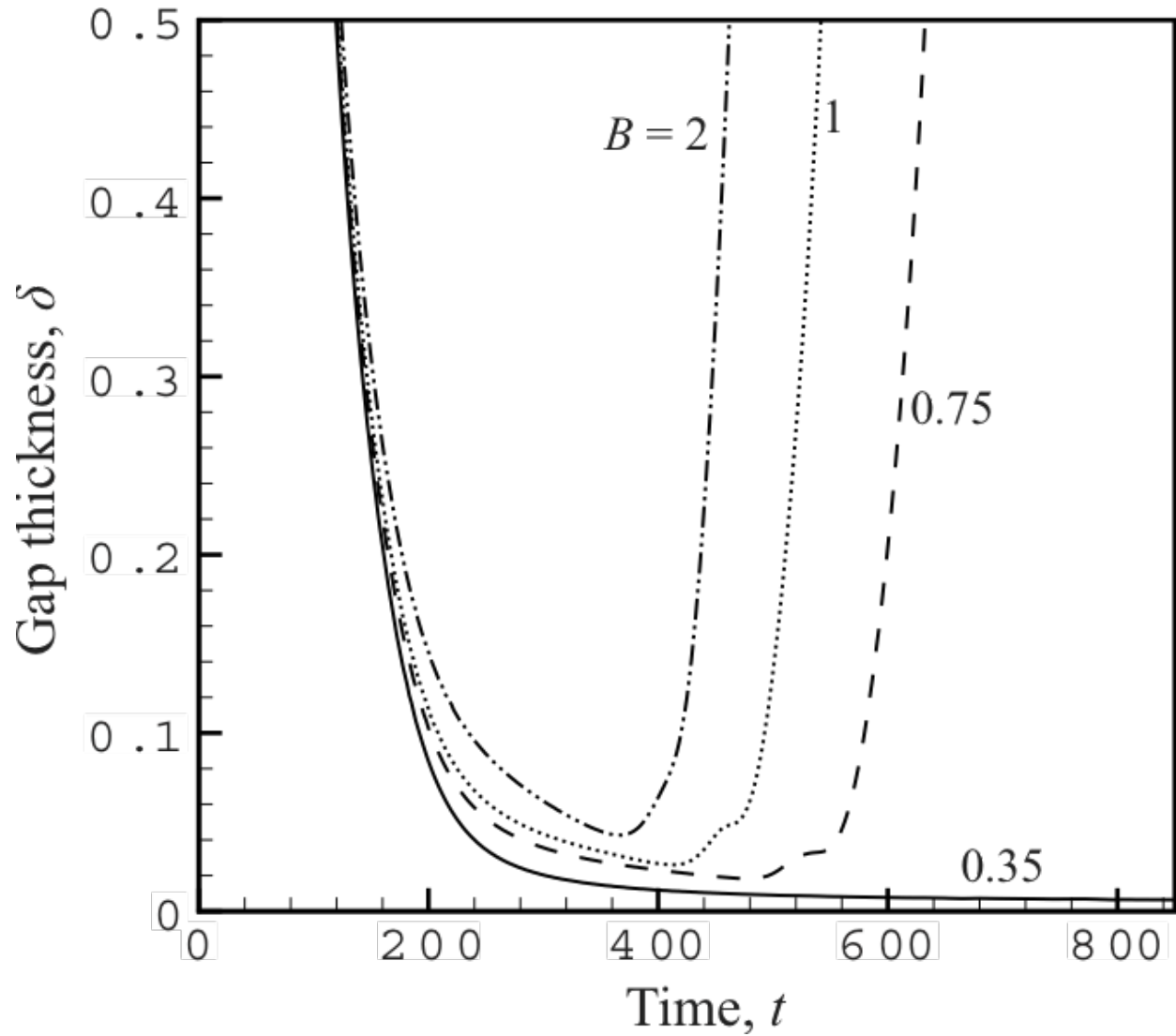


Fig. 2.7: The temporal dynamics of the drop-solid spacing for squeezing through a ring constriction with  $a_s/b_s = 2.25$ ,  $a/b_s = 1.5$ ,  $\lambda = 0.8$ , and  $B = 2, 1, 0.75$ , and  $0.35$ ; the surface discretizations are the same as in Fig. 2.6.

#### 2.5.4 Drop Squeezing Dynamics and Exit Times

Next, the squeezing mechanism is described in detail. In Fig. 2.8(a), the drop positions and shapes are shown at equally spaced times during squeezing. First, as the drop approaches the constriction, its velocity decreases and the drop flattens due to the presence of the constriction. Next, the leading edge pushes through the entrance of the constriction and the sides of the drop deform to the shape of the constriction. If  $B$  is above the critical value, then the drop slowly pushes through the constriction, which requires the drop to deform substantially as it passes through. Then, as the drop exits, the leading edge pulls on the elongating drop because the velocity is much higher outside the constriction. However, the trailing edge slows the drop down due to the drop-solid gap being so small. The competing effects of the leading and trailing edges of the drop account for the local maximum of the average drop velocity observed as the drop passes through the constriction. In Fig. 2.8(b), for the same size drop and ring but lower Bond number, the drop becomes trapped in the constriction and reaches a steady-state shape. In this case, the interfacial tension is too high to allow the drop to deform enough to pass through the constriction.

The effect of viscosity ratio on drop velocity, squeezing time, and the minimum drop-solid gap was studied by performing runs with constant  $B$  and constriction geometry at different  $\lambda$  values. As shown in Fig. 2.9, drops of higher viscosity take longer to pass through the constriction because of higher lubrication shear stresses in the narrow gap due to the lower mobility of the drop interface. As a result, a more viscous drop reaches a smaller minimum gap and a smaller minimum velocity (for 3D flow-induced squeezing [Zinchenko & Davis (2006)], though an opposite trend for the gap was observed, namely, the minimum separation increases with  $\lambda$ ). As shown in Fig. 2.10, the squeezing time increases not only with viscosity ratio but also

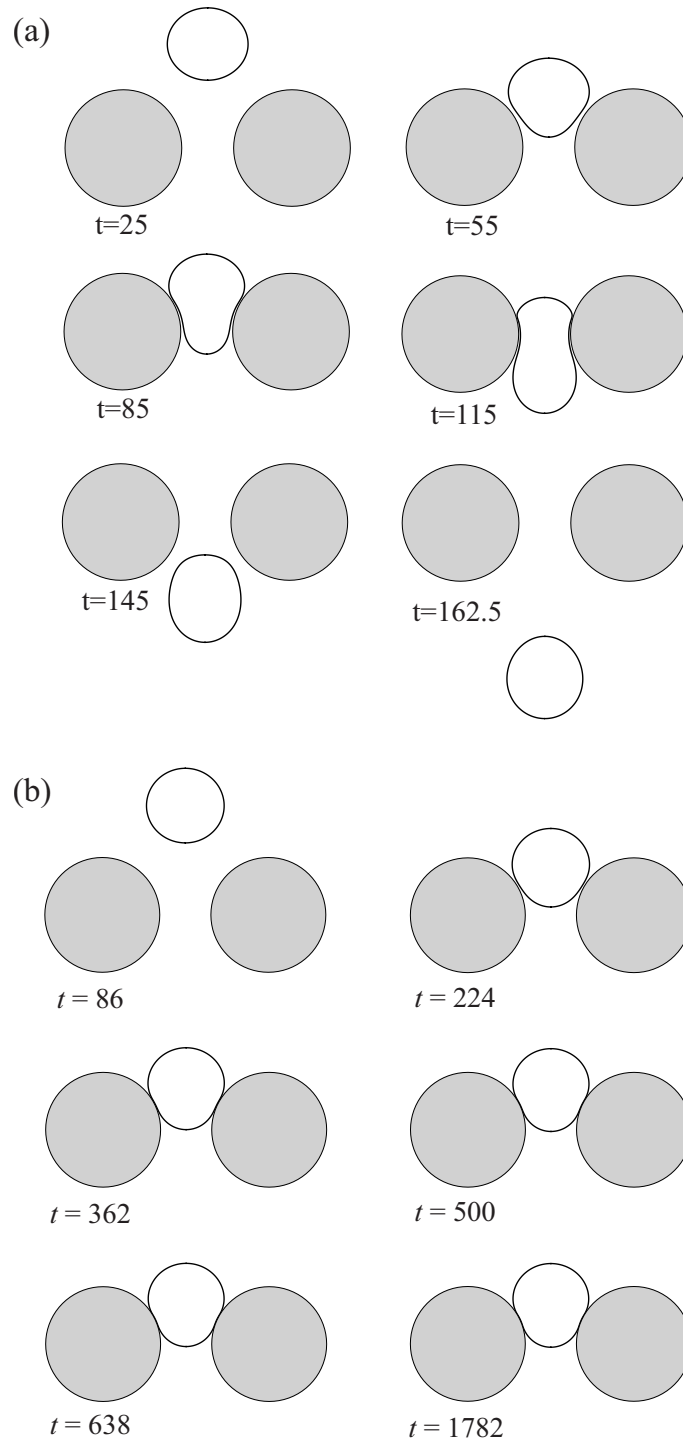


Fig. 2.8: (a) Snapshots of the drop motion through a ring constriction with  $a_s/b_s = 2.25$ ,  $a/b_s = 1.5$ ,  $\lambda = 0.8$ ,  $B = 1$ , and 600 node points used on both surfaces  $S_d$  and  $S_p$ . (b) Snapshots of the drop motion leading to trapping in a ring constriction with  $a_s/b_s = 2.25$ ,  $a/b_s = 1.5$ ,  $\lambda = 0.8$ , and  $B = 0.35$ , and 600 and 1000 node points used on surfaces  $S_d$  and  $S_p$ , respectively.

with decreasing Bond number because drops with higher interfacial tension do not deform as easily and so are more difficult to squeeze through the constriction.

Next, the effect of the cross-sectional size ( $a_s/a$ ) on  $T_s$  is explored for  $a/b_s = 2$ ,  $\lambda = 4$ , and varying  $B$ , as shown in Fig. 2.11. A nonmonotonic behavior is observed with a minimum  $T_s$  when the drop and the ring cross-sectional radius are roughly the same,  $a_s/a = O(1)$ . For a constant hole size and Bond number, smaller rings slow down squeezing because of the higher local mean curvature, whereas larger rings slow down squeezing due to a longer pathway. Of interest is size exploring if a minimum squeezing time can be observed for other constriction types when the size of the drop and constriction are similar.

A further test of the boundary-integral algorithm is to use it to determine the critical Bond number and then compare the result to that from the highly accurate and efficient Young–Laplace algorithm of Sec. 2.4. To do so, accurate values of the squeezing times were found for slightly supercritical Bond numbers, and then the critical Bond number was determined by extrapolation to where the squeezing time becomes infinitely long. For a given constriction geometry, accurate drop squeezing times were determined for different supercritical  $B$  using the BI algorithm by varying the total number of surface nodes ( $N_s$ ) at each  $B$  and plotting  $T_s$  versus  $1/N_s$  to extrapolate to infinite resolution. As shown in Fig. 2.12, a linear relationship is determined from  $T_s$  versus  $1/N_s$ . The  $y$ -intercept gives the converged value of  $T_s$ , and the result for the conditions of Fig. 12 is  $T_s = 234.73 \pm 0.06$  at the 95% confidence level.

Once accurate values of the squeezing times were determined, a plot of  $B$  versus  $1/T_s$  yields the critical Bond number as the limit where  $1/T_s \rightarrow 0$ . As shown in Fig. 2.13, there appears to be a

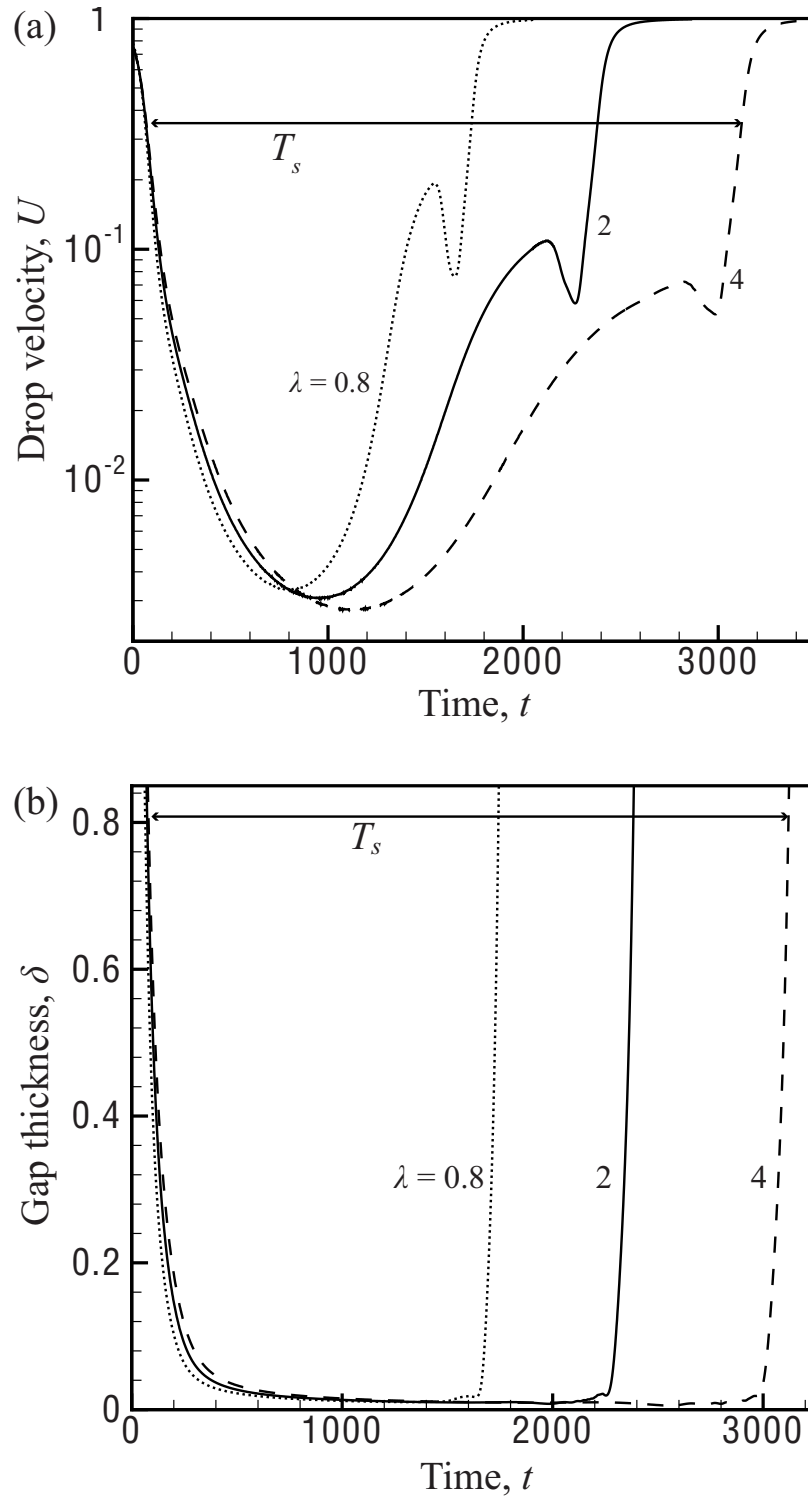


Fig. 2.9: (a) Drop velocity and (b) drop-solid minimum spacing for drop squeezing through a ring constriction, with  $a_s/b_s = 3$ ,  $a/b_s = 2$ ,  $B = 1.1$ , and  $\lambda = 0.8, 2$ , and  $4$  (left to right). The squeezing duration  $T_s$  is shown for  $\lambda = 4$ .

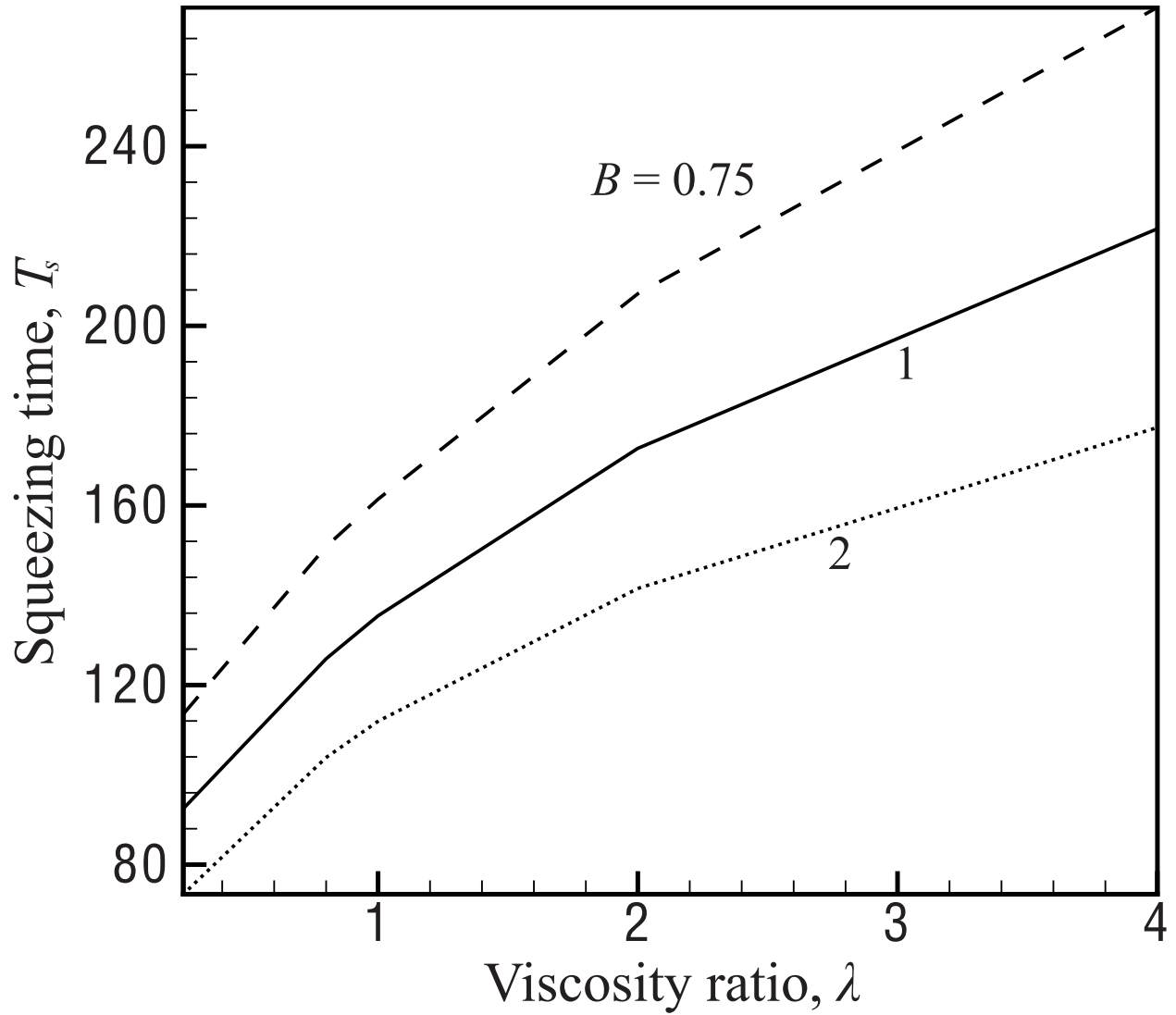


Fig. 2.10: Squeezing time vs viscosity ratio for  $a_s/b_s = 3$ ,  $a/b_s = 2$ , and  $B = 0.75, 1$ , and  $2$  (top to bottom).

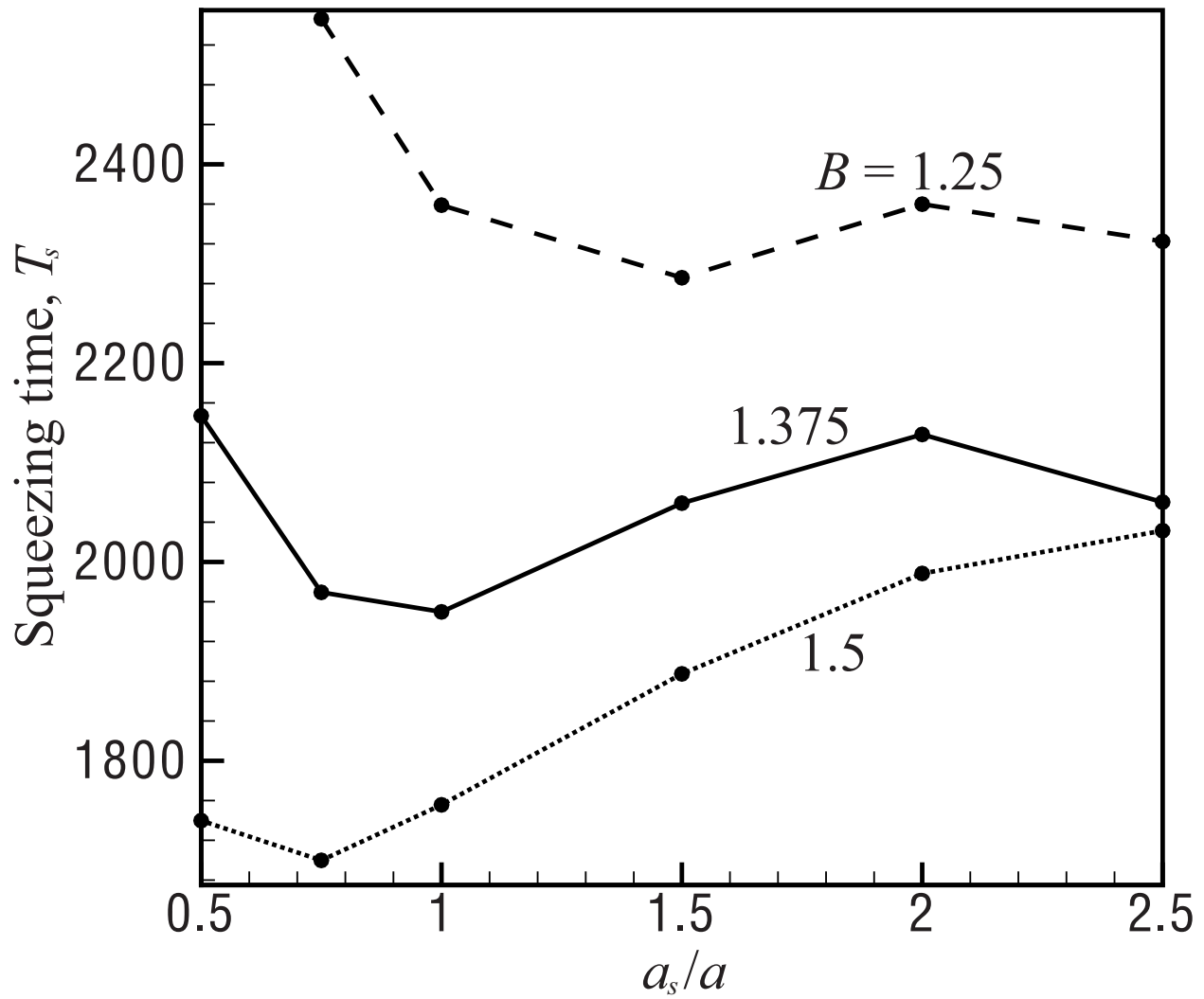


Fig. 2.11: Squeezing time vs ring cross-section-to-drop size for  $a/b_s = 2$ ,  $\lambda = 4$ , and  $B = 1.25$ , 1.375, and 1.5 (top to bottom).

power-law dependence of the form

$$B - B_c \propto \frac{1}{T_s^\alpha} \quad (2.41)$$

near the critical Bond number. From a nonlinear regression, the best-fit exponent is  $\alpha = 2.00 \pm 0.01$  and the best-fit intercept is  $B_c = 0.41 \pm 0.01$ , both at the 95% confidence level. Excellent agreement with the value of  $B_c = 0.410$  from the Young–Laplace algorithm is obtained for  $a/b_s = 1.5$  and  $a_s/b_s = 3$  (independent of the viscosity ratio since the critical value is based on a static configuration). This procedure was repeated for  $a/b_s = 1.5$  and  $a_s/b_s = 1.5$ , yielding  $\alpha = 1.998 \pm 0.002$  and  $B_c = 0.48 \pm 0.03$  at the 95% confidence level from the BI results, again in excellent agreement with  $B_c = 0.482$  from the YL algorithm.

The value of the exponent  $\alpha$  may be confirmed with the aid of the results from the Young–Laplace algorithm (see Sec. 2.4). First, an accurate value of  $B_c$  is determined from the YL algorithm. Then, the natural logarithm of  $(B - B_c)$ ,  $\ln(B - B_c)$ , is plotted versus  $\ln(1/T_s)$ , as shown in Fig. 2.14, and the resulting slope is  $\alpha$ . For  $a/b_s = 1.5$  and  $a_s/b_s = 3$ , it is found that  $\alpha = 1.9 \pm 0.2$  at the 95% confidence level. This approach was repeated for  $a/b_s = 1.5$  and  $a_s/b_s = 1.5$ , resulting in  $\alpha = 2.1 \pm 0.4$  at the 95% confidence level. This result confirms the scaling we assumed for when the Bond number approaches the critical value, namely,  $B - B_c$  is proportional to  $(1/T_s)^\alpha$ , where  $\alpha = 2.0$ .

It would be worthwhile to analytically derive the squeezing time scaling,  $T_s \propto (B - B_c)^{-1/2}$ . In a related study, Bretherton (1961) considered buoyancy-induced squeezing of a long bubble (with  $\lambda = 0$ ) through a vertical, straight, and circular tube sealed from one end. He found that the bubble motion is completely arrested for tube Bond numbers ( $B_t = \Delta\rho g r^2 / \sigma$ , where  $r$  is the tube radius) below  $(B_t)_c = 0.842$ . For  $B_t$  slightly above this critical value, he found the drop velocity

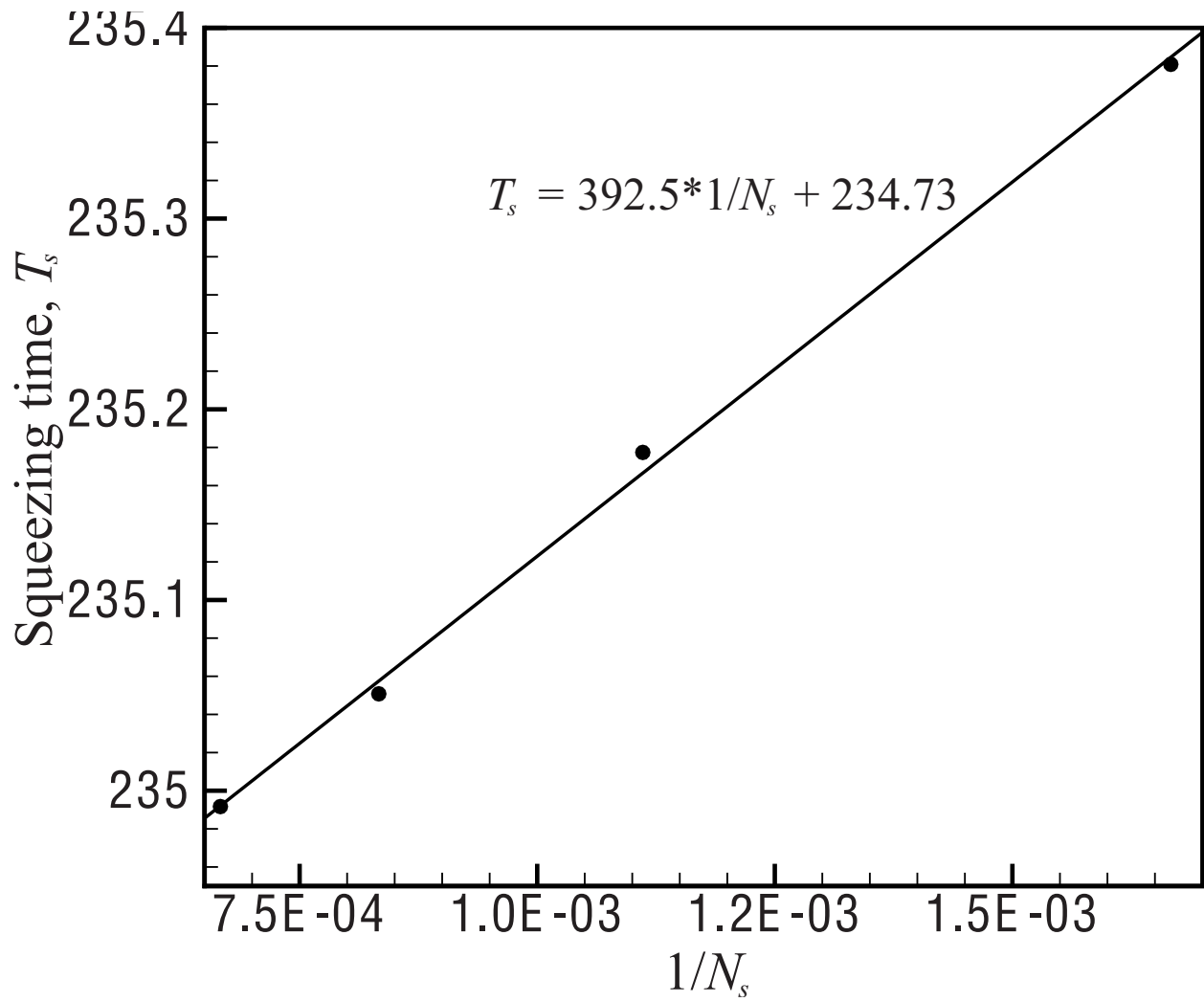


Fig. 2.12: Squeezing time vs resolution for  $B = 0.6$ ,  $a/b_s = 1.5$ ,  $a_s/b_s = 3$ , and  $\lambda = 1$ , with the total number of nodes ( $N_s$ ) distributed in the ratio 2:1 on  $S_p$  and  $S_d$ .

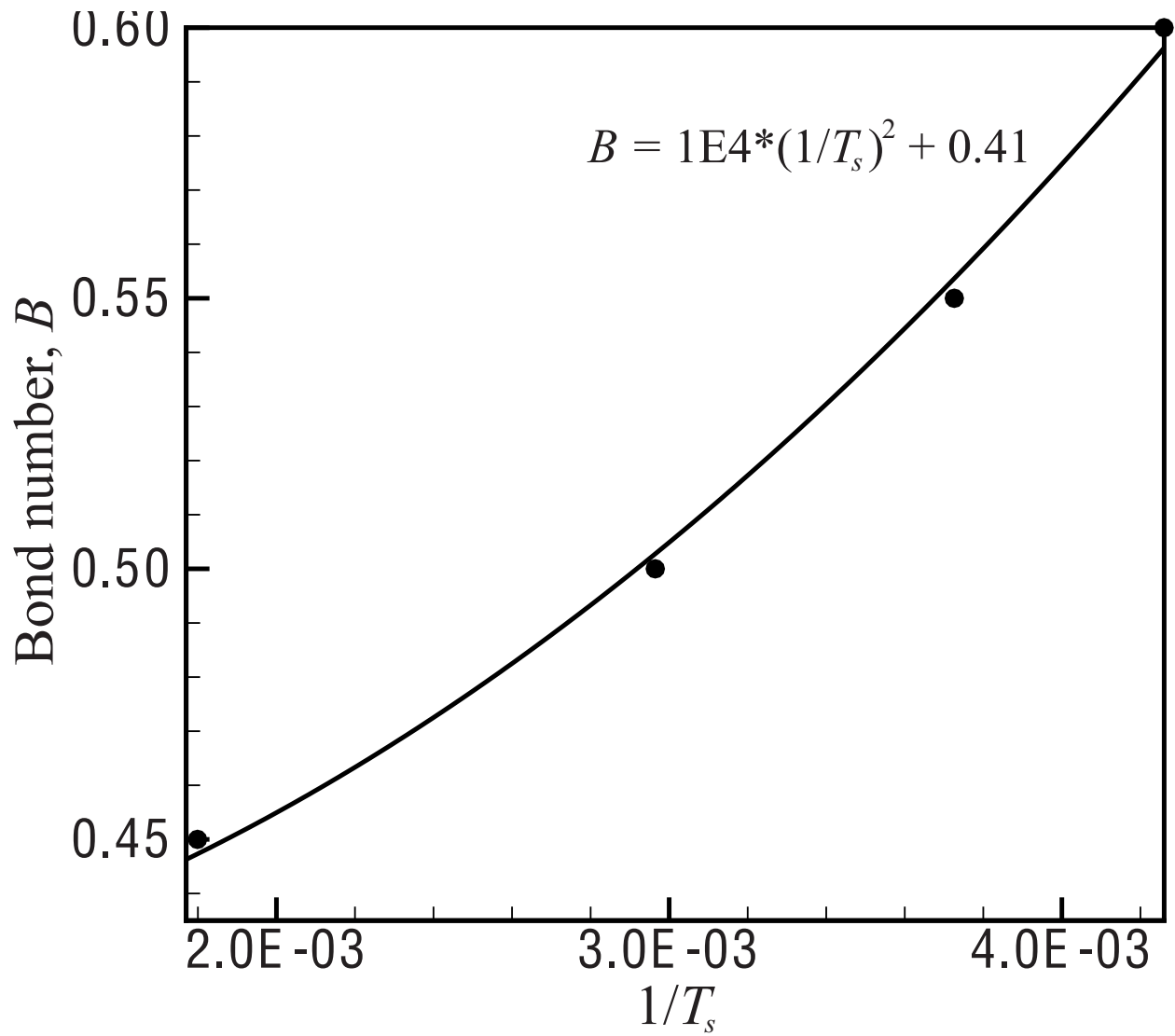


Fig. 2.13: Nonlinear regression for Bond number vs reciprocal of squeezing time for  $a/b_s = 1.5$ ,  $a_s/b_s = 3$ , and  $\lambda = 1$ .

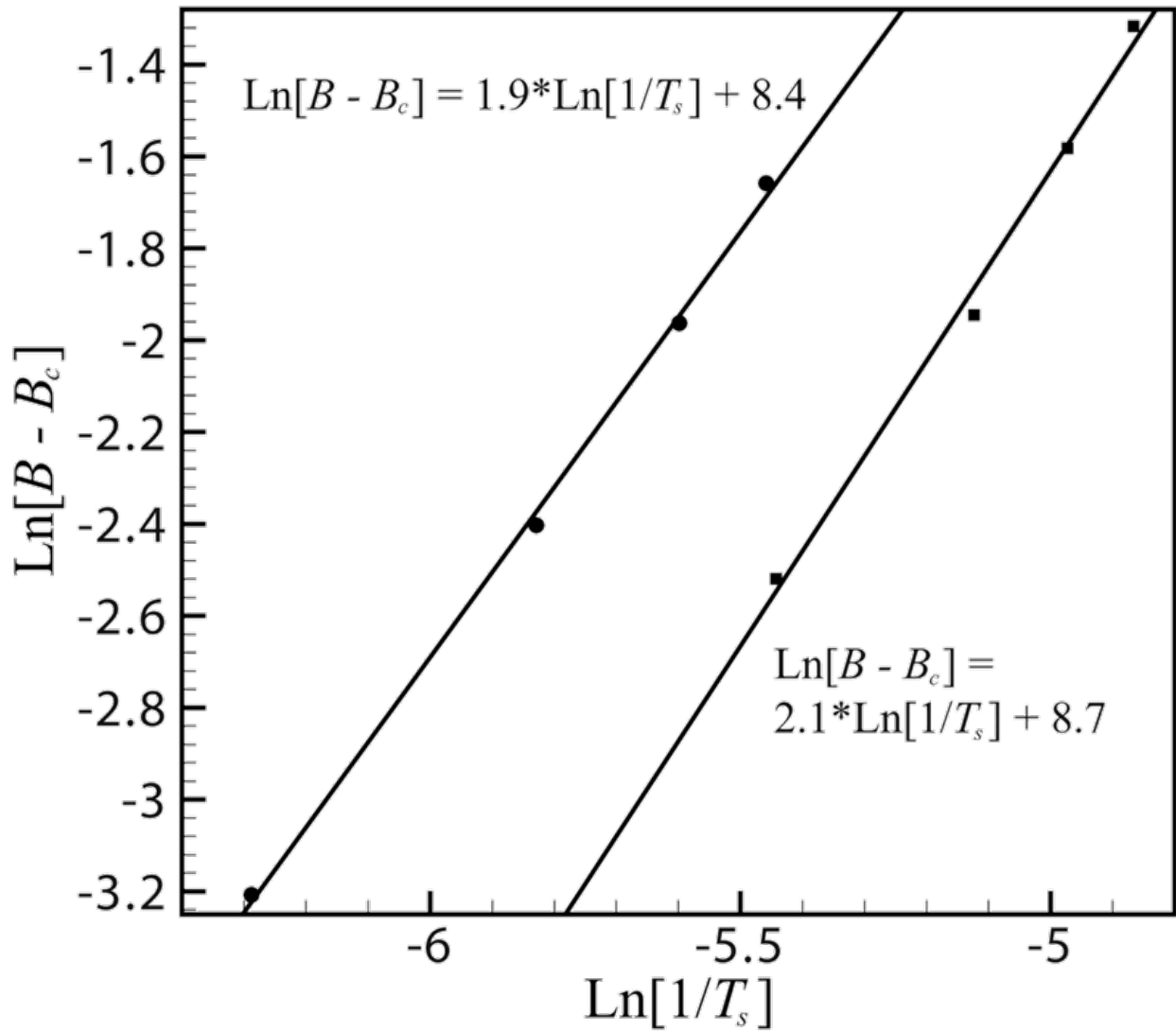


Fig. 2.14: Determination of the power-law exponent  $\alpha$  using YL for  $B_c$  and BI for  $T_s$  when  $B < B_c$ . The circles represent simulation results for  $a/b_s = 1.5$ ,  $a_s/b_s = 3$ , and  $\lambda = 1$ , and the squares represent simulation results for  $a/b_s = 1.5$ ,  $a_s/b_s = 1$ , and  $\lambda = 1$ .

scaling,  $U \propto [B_r - (B_r)_c]^{9/2}$ , by matched asymptotic expansions. It is tempting to apply Bretherton's approach to the present problem; however, there are many fundamental differences between the two problems, and we have not been able to succeed. First, the curved surface of the solid-ring constriction in the present problem contributes a nonzero, leading term to the dynamic pressure gradient along the lubrication area. Since the present problem is unsteady, the film-thickness evolution is described by a nonlinear, partial differential equation, which is quite different from the simpler ordinary differential equation in Bretherton's problem. The wetting points,  $W_1$  and  $W_2$ , limiting the lubrication area, are not known *a priori*, and they move as the drop squeezes through the constriction. So, we are unable to find the scale for the film thickness through matching with the outer solution, and Bretherton's technique could not be applied herein. It is not clear at all how the difference,  $B - B_c$ , enters the equations in the present case. The present problem deals with an arbitrary viscosity ratio  $\lambda$ , while Bretherton's analysis was developed for  $\lambda = 0$  only, so the internal drop motion could be ignored. Finally, in the present problem, the critical Bond number is found in a different manner. Equation (2.36) is a result of connectivity between the sessile and pendant surfaces both through the drop and external fluid domains. The latter does not hold for Bretherton's problem, where the tube is sealed from one end, and Eq. (2.36) could not be written.

It is interesting to compare the present scaling  $T_s \sim (B - B_c)^{-1/2}$  with the result  $T_s \sim (\text{Ca} - \text{Ca}_{\text{crit}})^{-1/3}$  for pressure-driven, 3D flow of a periodic emulsion through a cubic lattice, obtained by Zinchenko and Davis (*POF* 2008) from BI simulations, where  $\text{Ca}$  is the capillary number based on the pressure driving force and  $\text{Ca}_{\text{crit}}$  is the critical value below which trapping occurs. More studies need to be conducted to determine the physical reason for the differences in scaling observed for gravity and flow-induced squeezing. One possible explanation is the

different behaviors of the lubrication gap at  $B \rightarrow B_c$ . Curiously, the exponent  $\alpha$  found here is the same as in the scaling [Navot (1999) and Blawdziewicz *et al.* (2002)]  $Ca - Ca_{\text{crit}} \sim 1/T^2$  for the breakup time for a single drop in an unbounded linear flow near-critical conditions. The latter result was derived [Blawdziewicz *et al.* (2002)] from a general asymptotic analysis assuming an expansion for the capillary-driven drop response as a Taylor series in the deviation of the drop shape from the critical stationary shape. At present, though, the connection between the two, very different problems is not understood. More research is necessary to determine if any physical similarities exist between gravity-induced squeezing and flow-induced drop breakup to account for the similarities in scaling.

By keeping the cross-sectional radius of the ring constant at  $a_s/a = 1$  and varying the hole radius, different static drop shapes are generated using the YL algorithm by varying  $B$  below its critical value, as shown in Fig. 2.15. The dashed lines show the final drop interfaces for  $B \rightarrow B_c$ . The YL solution for trapped shapes ( $B < B_c$ ) is independent of the viscosity ratio because a static drop shape has no flow or viscosity effects and is independent of the drop motion to reach equilibrium. As  $B$  increases, so that the interfacial tension is weaker, the pendant portion of the drop hangs lower in the constriction, the trailing edge of the drop is lowered slightly, and the drop shape becomes more elongated. Also, by making the hole radius larger,  $B_c$  decreases and the drop cannot deform as much before passing through the constriction.

The highly accurate YL static drop shapes are compared to the long-term drop shapes obtained from the BI algorithm at the same Bond numbers and geometry parameters. Fig. 2.16(a) shows the BI dynamically calculated drop shapes as they approach the static, trapped shape at  $B = 0.9B_c$ , and the final BI calculated shape is compared to the YL statically calculated drop shape in Fig. 2.16 (b). In principle, the BI algorithm could always be used to determine the static drop

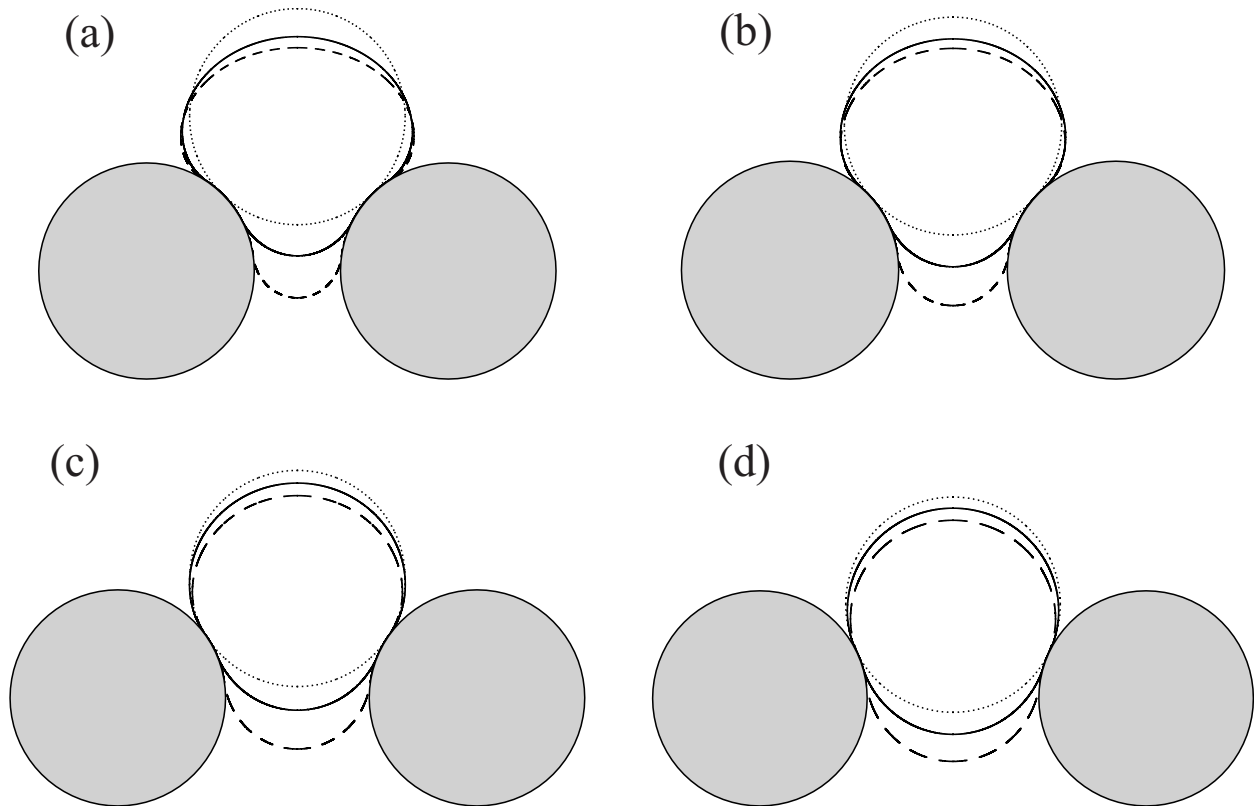


Fig. 2.15: Steady-state trapped drop shapes for (a)  $a_s/b_s = a/b_s = 2.5$  and  $B = 0.001$  (dotted line), 0.5 (solid line), and 1.584 (dashed line); (b)  $a_s/b_s = a/b_s = 2$  and  $B = 0.001$  (dotted line), 0.7 (solid line), and 1.025 (dashed line); (c)  $a_s/b_s = a/b_s = 1.5$  and  $B = 0.001$  (dotted line), 0.3 (solid line), and 0.482 (dashed line); and (d)  $a_s/b_s = a/b_s = 1.25$  and  $B = 0.001$  (dotted line), 0.15 (solid line), and 0.213 (dashed line).

shape for subcritical Bond numbers at large times and with high surface resolution, but the YL algorithm is much more efficient for this purpose. Figure 2.16(a) demonstrates that the BI simulation is sufficient to attain a steady-state shape before numerical crash due to a vanishingly small drop-solid gap, and this shape is in excellent agreement with the one obtained by the YL static algorithm, as observed in Fig. 2.16(b). Due to CPU time limitations on the BI simulations, we use the YL algorithm for all subsequent calculations of  $B_c$  and of steady shapes for  $B < B_c$ .

### 2.5.5 Drop “Dripping” Dynamics

The loss of a drop steady-state on a ring constriction may be due to not only squeezing through the interior hole but also dripping over the exterior edge for sufficiently large drops. We have observed, through numerical simulation, the initial stages of the drop dripping around the outer edge of the ring. For the mechanism shown in Figs. (2.17) and (2.18), as the drop approaches the constriction, its average velocity decreases, and its perimeter becomes unstable, which is quite different from the center of the drop becoming unstable (as in the case of drop squeezing). Next, the drop begins to deform around the exterior of the ring, and the Figs. (2.17) and (2.18) show the central part of the drop becoming increasingly thin. It is interesting to note that, in Fig. 2.17, the hole is so small that the drop never enters the interior of the ring, but the center of the drop instead arches away from the ring as the dripping proceeds. Quite differently from Fig. 2.17 is the case shown in Fig. 2.18, where the hole is large enough so that the center of the drop leading edge protrudes slightly into the interior of the ring as the drop perimeter “drips” around the exterior of the ring.

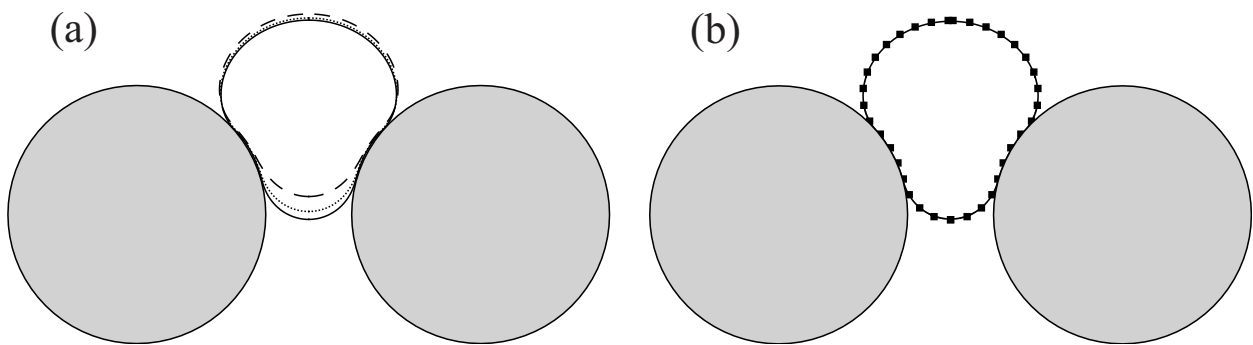


Fig. 2.16: BI dynamically calculated drop interface shapes at the time moments  $t = 375$  (dashed line),  $t = 750$  (dotted line), and  $t = 2438$  (solid line), and (b) comparison between the BI dynamically calculated ( $t = 2438$ , squares) and the YL calculated (solid line) static drop shapes, at  $B = 0.885$ ,  $a_s/b_s = 3$ , and  $a/b_s = 2$ , with  $\lambda = 1$  for the BI trial.

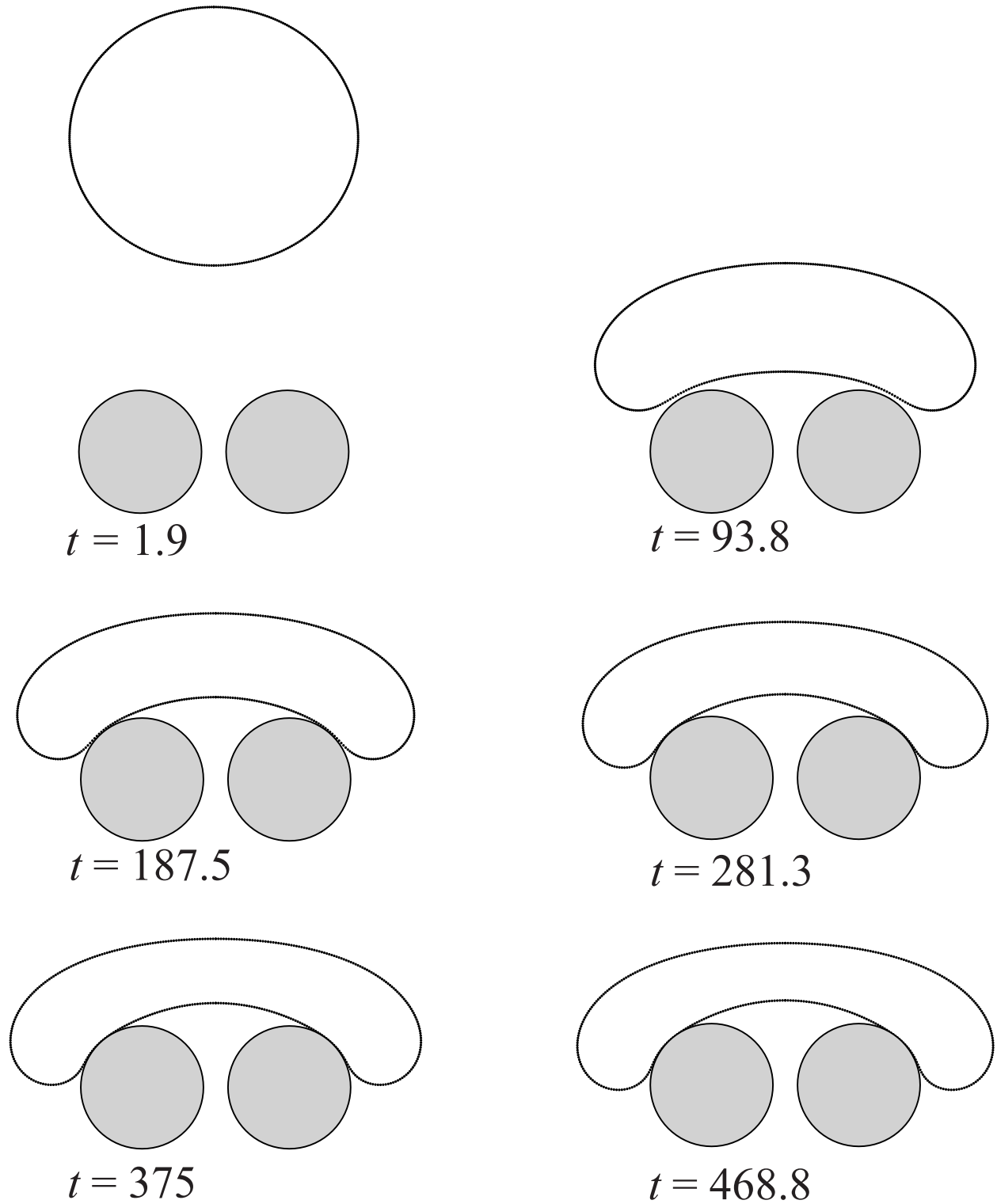


Fig. 2.17: Snapshots of drop motion for dripping around a ring with  $a/b_s = 11.7$ ,  $a_s/b_s = 5$ ,  $\lambda = 1$ ,  $B = 3.25$  ( $B_c = 3.19$ ), with 200 nodes on  $S_d$  and 400 nodes on  $S_p$ .

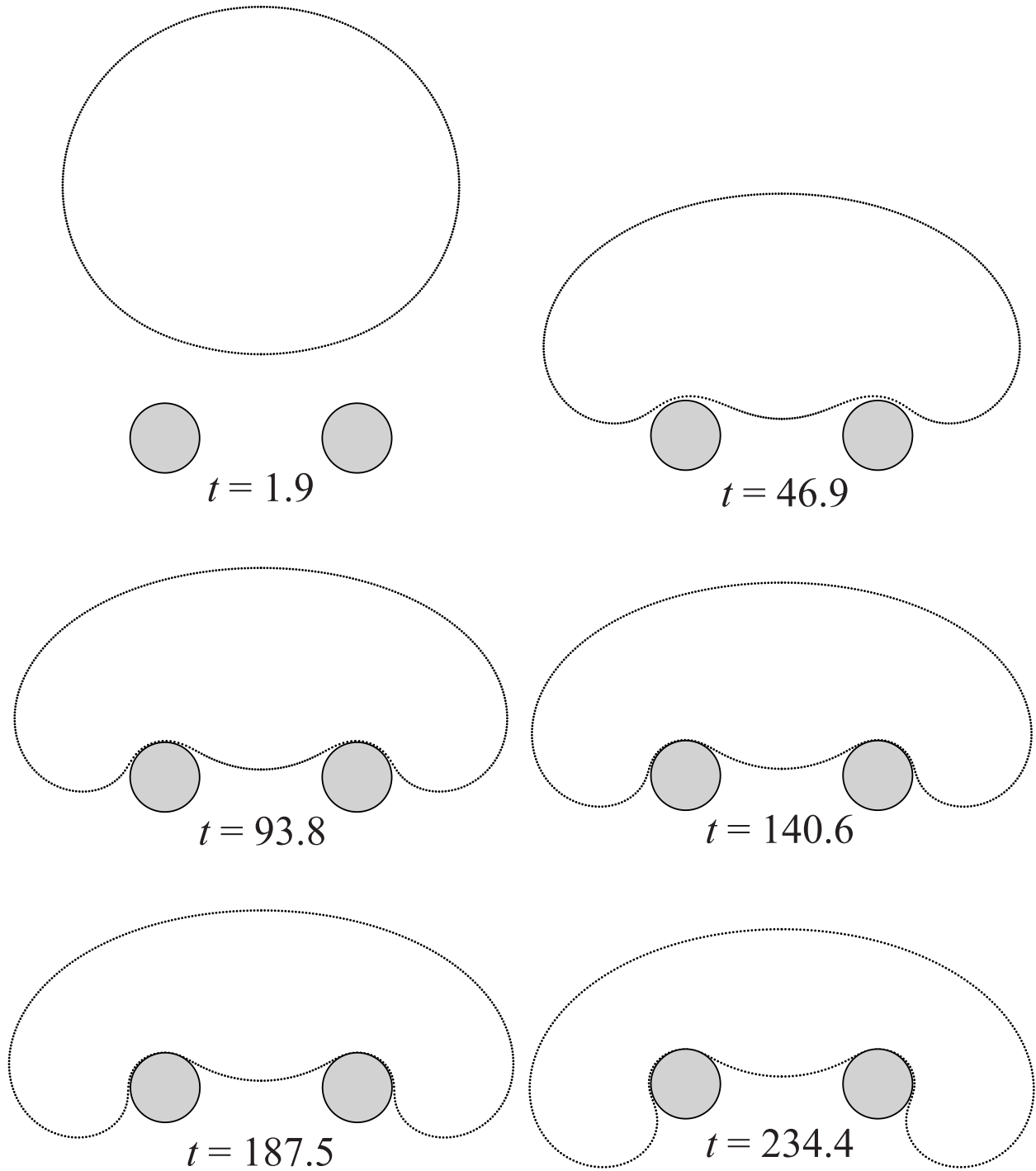


Fig. 2.18: Snapshots of drop motion for dripping around a ring with  $a/b_s = 3.2$ ,  $a_s/b_s = 0.567$ ,  $\lambda = 1$ , and  $B = 2.2$  ( $B_c = 1.9$ ) with 200 nodes on  $S_d$  and 400 nodes on  $S_p$ .

### 2.5.6 Critical Bond Number and Steady Drop Shapes for Trapping

Critical Bond numbers, demarcating drop steady states on a ring, are calculated with high speed and accuracy for a large constriction geometry parameter space using the axisymmetric YL algorithm. As shown in Fig. 2.19, for moderate  $a/b_s$  and  $a_s/b_s$  values, increasing the drop-to-hole size ratio increases the critical Bond number nearly linearly for multiple ring sizes. Under these conditions, the gravitational force required to push a drop through a ring increases with the inverse of the hole size. It is also observed that increasing the ring cross section weakly decreases the critical Bond number for both a fixed drop and ring sizes due to a smoother pathway. For a broader  $a/b_s$  and  $a_s/b_s$  parameter space, as shown in Fig. 2.20, a maximum critical Bond number is observed, for multiple rings (cross-section-to-hole values), by varying the ratio of the drop and the total ring radii,  $a/(2a_s+b_s)$ . The maximum  $B_c$  occurs at the drop size where there is a transition, when  $B > B_c$ , from the drop passing through the inside hole of the ring for smaller drop sizes to it dripping around the outside edge of the ring for large drop sizes.

The insets in Fig. 2.20 for  $a_s/b_s = 5$  show two typical steady-state drop shapes for slightly subcritical Bond numbers on the squeezing (top inset) and dripping (bottom inset) branches. Although the shapes for the dripping branch are different from the one depicted in Fig. 2.3, the generalization of the YL algorithm from Sec. 2.4 still applies. As shown in Fig. 2.21(a), when  $B_c = 7.35$  is approached from below, the wetting point  $W_1$  outside the ring hole is practically insensitive to changes in  $B$ , while the wetting point  $W_2$  inside the ring hole moves sharply to the center of the hole. In contrast, as follows from Fig. 2.21(b), when  $B_c = 2.38$  is approached from below,  $W_2$  inside the ring hole is practically insensitive to changes in  $B$ , while  $W_1$  outside the ring hole shows a strong variation. These results clarify the physical nature of the two branches for each line in Fig. 2.20.

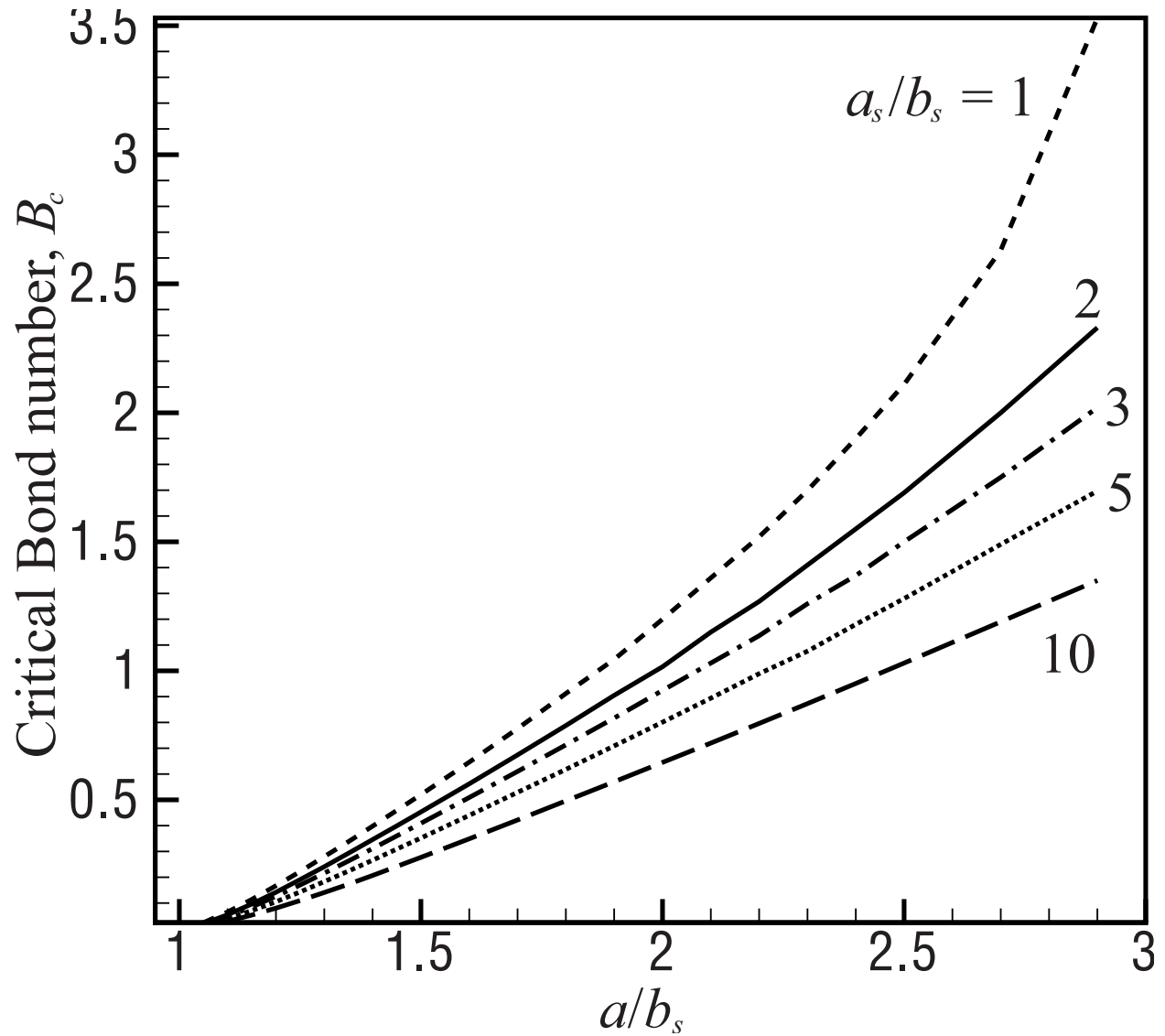


Fig. 2.19: Critical Bond number values vs drop-to-hole ratio  $a/b_s$  at cross-section-to-hole ratio  $a_s/b_s = 1, 2, 3, 4,$  and  $10$  (top to bottom).

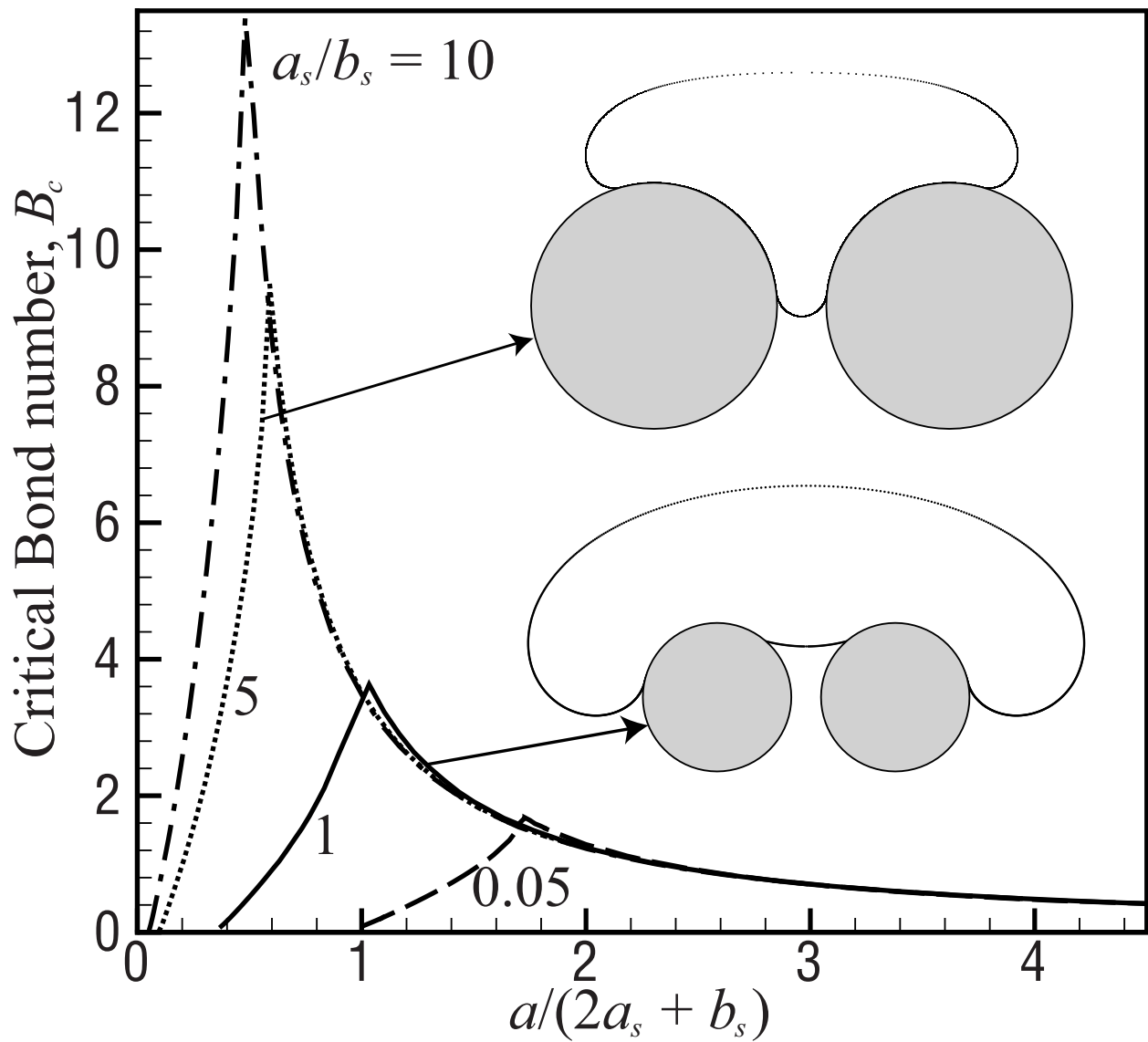


Fig. 2.20: Critical Bond number vs drop-to-total ring radius for  $a_s/b_s = 0.05, 1, 5$  and  $10$  (bottom to top). The insets show two steady-state, slightly subcritical drop shapes for  $a_s/b_s = 5$ , with  $B = 7.35$ ,  $a/(2a_s + b_s) = 0.5545$  (top) and  $B = 2.38$ ,  $a/(2a_s + b_s) = 1.28$  (bottom).

Overall, for realistic values of  $a/b_s$  and  $a_s/b_s$ , the critical Bond number is a strong, nearly linear function of drop-to-hole size, and a weak, decreasing function of constriction-to-drop size, whose effect could be ignored except for tight rings. Also, the critical Bond number reaches a maximum value versus the drop-to-total ring radius because the drop becomes too large for the ring and will start to drip around the edges instead of passing through the hole. The maxima are sharp due to the bifurcation that occurs at this junction between the drop passing through the hole (which becomes harder as the drop size increases) and dripping over the outside edge (which becomes easier as the drop size increases).

## 2.6 Concluding Remarks

An axisymmetric BI algorithm has been developed to study buoyancy-driven deformable drop squeezing through a ring constriction. This problem is a prototype for emulsions settling through porous media. Interesting features of the problem include the reduction in drop velocity as it passes through the constriction, the minimum drop-solid spacing during squeezing, and the conditions for which trapping occurs. The algorithm uses the Hebeker representation for the solid-particle contribution to the boundary-integral equations, which is a proportional combination of the single- and double-layer potentials. The high-order, near-singularity subtraction technique used in the solid-to-drop contributions was necessary to simulate slow-squeezing cases, when the Bond number is close to critical. The coupled system of equations for the fluid velocity on the drop and the Hebeker density on the ring constriction was successfully solved by a minimal residual technique, while traditional “successive substitutions” are divergent. For cases when the drop is trapped, an alternative, highly efficient static algorithm is developed based on YL equation for the sessile and pendant parts, coupled through the “wetted” area.

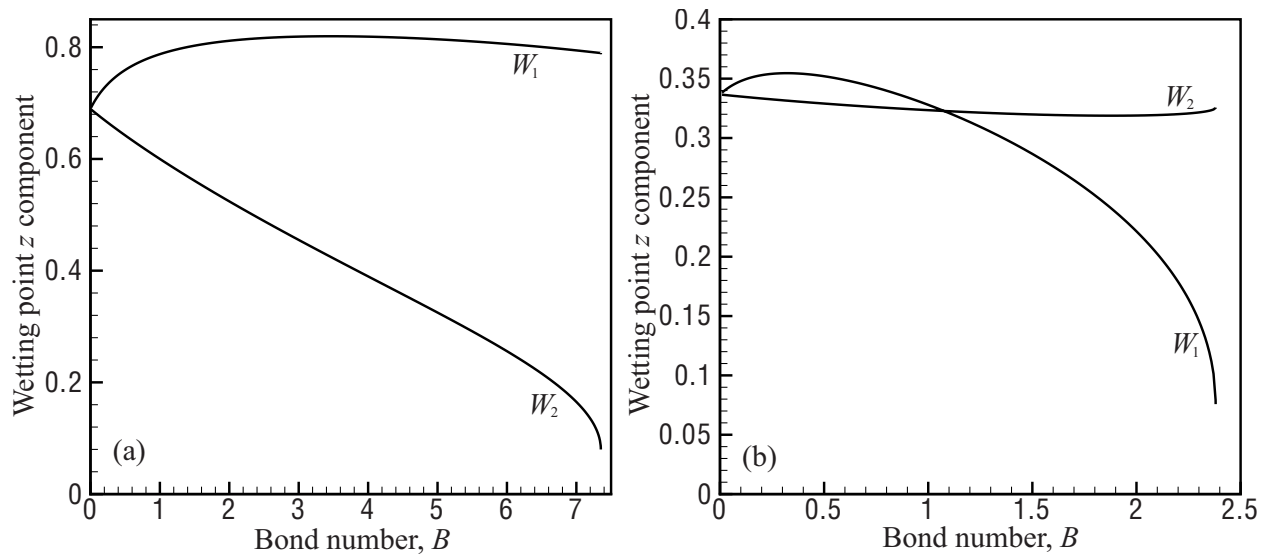


Fig. 2.21: The vertical position of wetting points  $W_1$  and  $W_2$  for  $a_s/b_s = 5$  as the critical Bond number is approached for the (a) squeezing, with  $B_c = 7.35$  and  $a/(2a_s+b_s) = 0.55$ , and (b) dripping, with  $B_c = 2.38$  and  $a/(2a_s+b_s) = 1.28$ , branches.

We found for gravity-induced squeezing that squeezing time for the drop to pass through the constriction is proportional to  $(B-B_c)^{-1/2}$ , as the Bond number  $B$  approaches the critical value  $B_c$  from above. The drop squeezing time increases and the minimum drop-solid spacing decreases with increasing viscosity ratio. The time for the drop to pass the constriction increases with increasing viscosity ratio and decreasing Bond number. The squeezing time scaling for gravity-induced drop motion through a constriction found herein differs from the scaling  $T_s \propto (\text{Ca} - \text{Ca}_{\text{crit}})^{-1/3}$  obtained from numerical simulations by Zinchenko and Davis (*POF* 2008) for flow-induced, 3D squeezing of a periodic emulsion through a cubic lattice of spheres near a critical capillary number  $\text{Ca}_{\text{crit}}$ . The present axisymmetric code, capable of higher accuracy, can be modified in future work for flow-induced drop squeezing through a ring constriction to verify the  $-1/3$  versus  $-1/2$  scaling exponent.

For two example geometries, the BI and YL calculations were shown to compare favorably (both for static trapped drop shapes and critical Bond numbers); however, since the critical  $B$  results generated from the YL algorithm are more accurate and computationally faster, the YL algorithm is used exclusively for calculating critical Bond numbers and static trapped drop shapes given a specific set of geometry parameters. For moderate and realistic geometry parameters,  $B_c$  increases nearly in proportion to  $a/b_s$ , but it is only a weakly decreasing function of  $a_s/a$ . For a larger parameter space, the critical Bond number is an increasing function of the relative drop size until a maximum value is reached. Larger drops drip over the edges of the ring instead of passing through it at supercritical Bond numbers.

Drop squeezing and trapping mechanisms were observed experimentally using an apparatus with canola oil bulk phase and water or water/glycerol drop phase. Critical Bond numbers  $B_c$  were experimentally determined by placing increasingly larger drops on a ring and detecting the

transition from squeezing to trapping. The experimentally determined  $B_c$  compares favorably with the theoretical values obtained from the axisymmetric YL algorithm. The transition between squeezing and trapping is strongly dependent on the hole size of the ring and the fluid properties of the drop but only weakly dependent on the cross-sectional size of the ring, in good agreement with theory. Also, experimental trapped drop shapes show good agreement with those calculated using the axisymmetric YL algorithm. Our future work will include development of a three-dimensional YL algorithm for trapped drop shapes in channels of complex geometry and interparticle constrictions and determining corresponding critical Bond numbers for squeezing to occur.

## **2.7 Acknowledgements**

This work was supported by grants from the National Aeronautics and Space Administration (Grant No. NNC05GA55G) and Petroleum Research Fund of the American Chemical Society (Grant No. 40430-AC). T.R. was supported by a fellowship from the Department of Education Graduate Assistantships in Areas of National Need (GAANN) Program (Contract No. P200A060265).

## Chapter 3

### Trapping of a deformable drop in a three-dimensional constriction

#### Abstract

An artificial “time-dependent evolution” method is devised to determine trapping conditions for a drop moving due to buoyancy into a three-dimensional constriction. During the simulation, the drop surface advances by a rationally-devised normal “velocity,” containing both a local deviation of the Young-Laplace equation and the drop-solid clearance. Neither shape-solution iterations nor knowing the drop-solid contact area a priori are required, to solve the three-dimensional Young-Laplace equation via this artificial “time-dependent” process. For conditions near critical, where the trapped-drop steady state ceases to exist, severe surface-mesh distortions are treated by ‘passive mesh stabilization,’ mesh relaxation and topological transformations through node reconnections. For Bond numbers above a critical value, a drop is deformable enough to pass through the hole of the constriction, with no trapping. The critical Bond numbers are determined by extrapolation, through linearly fitting minima of the root-mean-squared surface velocities versus corresponding Bond numbers greater than critical. For ring and hyperbolic-tube constrictions, the results, including statically-trapped drops and critical Bond numbers, using both the present algorithm and a previous, axisymmetric method with extremely-high accuracy, show excellent agreement. Three-dimensional Young-Laplace and boundary-integral methods also give good agreement for the static shape of a drop trapped in a

tilted three-sphere constriction. For the following constriction types, including circular rings, hyperbolic tubes and agglomerates of three and four spheres, the critical Bond number increases nearly linearly with an increase in the drop-to-hole size ratio, which is also observed to be the most important geometry factor. Quite differently, the constriction type and tilt angle, which is the angle between the gravity vector and the normal to the plane of the constriction hole, only weakly affect the critical Bond number. Surprisingly, increasing the tilt angle, so that the horizontal projection of the hole is decreased, decreases the critical Bond number.

### 3.1 Introduction

In the absence of body forces, the shape between two, static fluids, i.e. an emulsion drop at rest on a solid, is described by the Young-Laplace (YL) equation, relating the pressure difference  $\Delta p$  across the interface and the curvature of this interface. Most research to date on deformable drops at a steady-state shape is of the classical problems of a drop either resting on or hanging from a solid surface. Practical applications of these previous research efforts include measuring the properties of the interfacial tension and contact angles associated with fluid interfaces in contact with solids and removing oil drops from surfaces.

Bashforth and Adams (1892) performed the first calculation of the axisymmetric shape of a drop, through numerical integration of the Young-Laplace equation. Rotenberg *et al.* (1983) developed a method for determining the interfacial tension and contact angle, by fitting empirical data from either a pendant or a sessile drop to a shape calculation, performed by numerical integration of the Young-Laplace equation. Chatterje (2002) calculated the critical Eötvös number, or half the Bond number, for the detachment of an oil drop due to buoyancy, by finding

the conditions where the solution of the Young-Laplace equation ceases to exist [Chatterje (2002)]. Related to the previous problems, a static drop trapped in a solid constriction is a prototypical model for the steady-state consequence of an emulsion settling through confined geometries, i.e. packed beds or porous media. The important applications, related to the settling of an emulsion through solid constrictions, are food and pharmaceutical manufacturing, oil-recovery, drop infiltration into a highly porous surface, fixed-bed catalytic reactors and liquid-liquid separation. Of particular engineering interest is determining the critical conditions delineating drop trapping within a constriction and drop squeezing through a constriction. Determining these critical conditions by dynamical boundary-integral simulations is especially difficult for gravity-driven motion, because the drop motion becomes very lubrication-sensitive as the critical conditions are approached. The near-critical, dynamical simulations require a high resolution on both the drop and solid surfaces and long simulation times to accurately handle the extremely small drop-solid fluid gaps. Therefore, a special static algorithm is meaningful to avoid very costly boundary-integral calculations and to improve the accuracy of the shape solutions for drops trapped in constrictions and of the critical conditions for demarcating the boundary between a drop becoming trapped within or squeezing through a constriction [Zinchenko & Davis 2006 and Ratcliffe *et al.* (2010)].

The shape calculation for trapped drops requires combining the solution of a fluid-fluid interface from the Young-Laplace equation with the solution of fluid-solid interface, which is assumed to be the same as the solid surface. Previous related research has been performed on solving for the shapes of two menisci in a capillary tube. The shape of the top interface is found through fitting of empirical data, and the shape of the bottom interface is found through a coupled set of Young-Laplace equations [Chatterje (2007)]. A major difference in this problem

and the trapping of a drop in a constriction is that the external fluid is not connected in a capillary tube.

Previous research has been performed for calculating the shape of a drop trapped in a ring constriction [Ratcliffe *et al.* (2010)]. For this axisymmetric problem, the solution is reduced to solving for the contour of the drop by numerically integrating the Young-Laplace (YL) equation from the tips along the drop arc length to the wetted points, which are the points of three-phase contact, for both the sessile and pendant portions, and calculating the free parameters in the equations by Newton-Raphson iterations. The free parameters are found so that the pressure continuity throughout the drop and conservation of the total drop volume are satisfied. Such an approach, however, cannot be generalized for three-dimensional constrictions, for example, when the axis of symmetry for an axisymmetric constriction is tilted relative to the gravity vector driving the motion of the drop. It is not clear how to accurately calculate the three-phase boundaries, because the wetting points for an axisymmetric constriction become wetting curves for 3D constrictions, or to calculate cumbersome derivatives of the drop surface necessary for Newton-Raphson iterations. Less work has been performed on solving three-dimensional (3D) fluid-fluid interfaces, but work by Brown *et al.* (1980) determined the shape of a three-dimensional drop resting on an inclined plane, through use of a finite element solution for the Young-Laplace equations, and empirical data for the wetted area of drop-solid contact.

### 3.1.1 Problem Description

For the present problem, we study the shape of deformable drops trapped due to gravity in an assortment of three-dimensional constrictions, including circular rings, hyperbolic tubes, three spheres, and four spheres. Fig. 3.1(a) depicts the initial conditions of a spherical, deformable

drop settling towards a constriction between three spheres. The constriction is held stationary in an unbounded and quiescent bulk-phase fluid with density  $\rho_e$  and viscosity  $\mu_e$ . The drop has an undeformed radius  $a$  and fluid properties of density  $\rho_d$  and viscosity  $\mu_d$ , respectively. A constant interfacial tension  $\sigma$  between the drop and external fluid is used, so the absence of surfactants is assumed. The surfaces of the drop and solid(s) are  $S_d$  and  $S_p$ , respectively, and the unit direction and magnitude of gravity are represented separately as  $\mathbf{d}$  and  $g$ , respectively. In Fig. 3.1(b), the drop statically trapped is a prototype for the steady-state consequence of emulsion flows through constrictions. It is assumed that the suspending fluid preferentially wets the solid and drop fluid is “nonwetting.” Then, the drop shape has a contact angle that is tangent to the solid surface, and protrudes into the hole by deforming between the spheres. Of note is that the viscosity ratio of the drop and external fluid phases is a dynamic property, and therefore does not affect the static solutions. The relevant length parameters for the multiple constriction types are illustrated in Fig. 3.2, where the minimum circle inscribing the interior of all the constriction types has a radius  $b_s$ , and where the ring cross section and sphere radius are  $a_s$ .

The nondimensionalized parameters, affecting the trapping of a drop in a constriction, are the Bond number ( $B = \Delta\rho g a^2 / \sigma$ , where  $\Delta\rho = \rho_d - \rho_e$ , and  $g$  is the magnitude of the acceleration due to gravity), the cross-section-to-hole radius ratio  $a_s/b_s$  and the drop-to-hole radius ratio  $a/b_s$ . The Bond number is the ratio of the gravitational and interfacial forces, and so a drop with a small Bond number tends to stay more spherical and a drop with a large Bond number tends to deform more easily. Important calculations include determining how the drop shape trapped in constriction is affected by the Bond number and the constriction geometry, and determining the critical Bond number  $B_{cr}$ , delineating the boundary between trapping, with  $B < B_{cr}$ , and

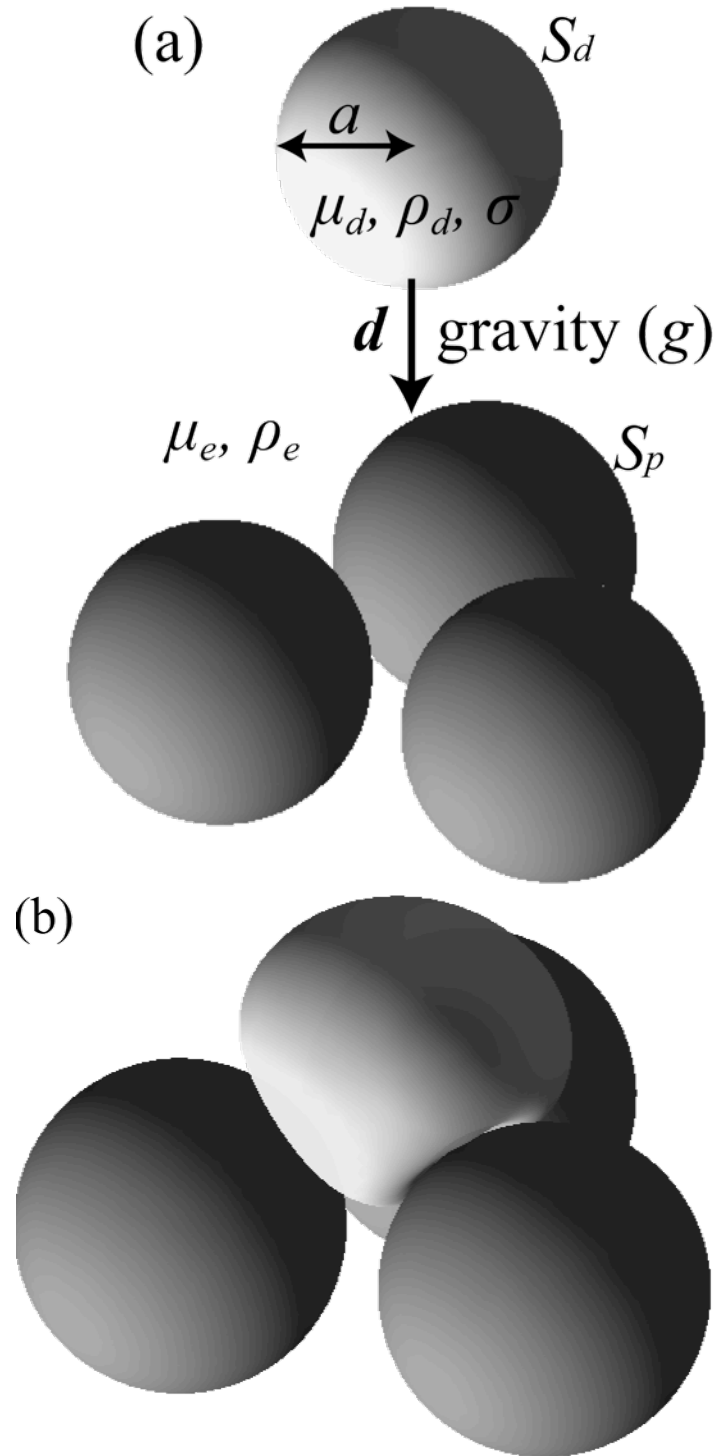


Fig. 3.1: (a) Deformable drop settling toward spheres. (b) Drop trapping inside the constriction at the steady-state shape for Bond number = 1, drop-to-hole radius ratio = 2.8 and sphere-to-hole radius ratio = 2.6.

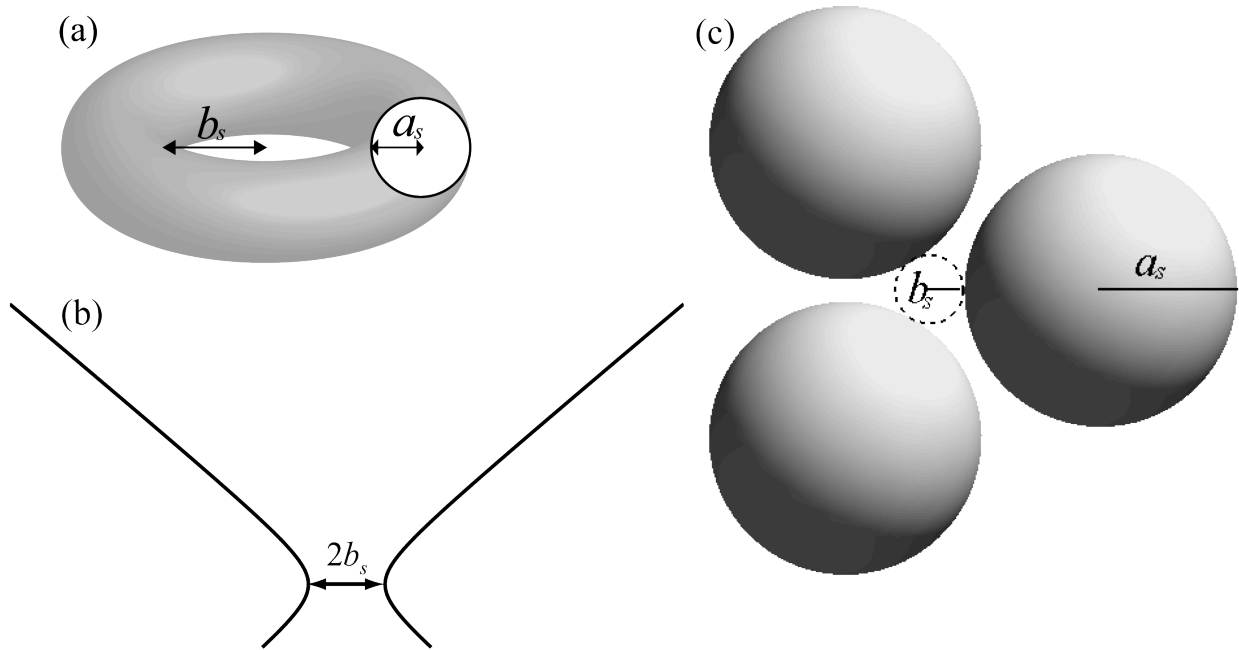


Fig. 3.2: (a) Ring constriction has length parameters of the hole and cross-sectional radii  $b_s$  and  $a_s$ , respectively. (b) Cross section of a hyperbolic tube is represented by solid lines, and the surface is described by the quadratic equation  $\frac{x^2}{b_s^2} + \frac{y^2}{b_s^2} - \frac{z^2}{c_s^2} = 1$ ,  $b_s$  is the skirt (hole) radius and  $c_s$  is the vertical length scale. (c) Three non-touching spheres are described by an inscribed circular radius  $b_s$  and a sphere radius  $a_s$ .

static results from an efficient, axisymmetric algorithm for the ring constriction. squeezing, with  $B > B_{cr}$ . Results from the 3D Young-Laplace method presented below are accurate, static results from an efficient, axisymmetric algorithm for the ring constriction.

### 3.2 Numerical Methods

As mentioned previously, boundary-integral algorithms may be used to simulate the gravitational settling of a deformable drop into a three-dimensional constriction for both of the consequential drop phenomena: dynamic pass through and steady-state trapping. However, for conditions near the critical point separating the phenomena, simulating drop motion is computationally prohibitive, so an accurate and efficient algorithm is desirable to elucidate both the steady-state branch and the critical point of separation. The surface of a trapped drop in a constriction contains two separate portions: (1) the interface (i.e. the portion of the drop interface that is not adjacent to the solids), governed by the Young-Laplace equation, and (2) the drop-solid interface (i.e. the portion of the drop interface in near-contact with the solid, separated by a very thin layer of the suspending fluid). Thus, it is not clear how to proceed with the seemingly feasible approach of numerically integrating the three-dimensional Young-Laplace (YL) equations from the drop tips to intersection of the distinct, drop-surface portions, without empirical knowledge used for an iterative solution.

#### 3.2.1 Three-dimensional Young-Laplace Solution Approach

We have developed an artificial dynamic process, the 3D YL algorithm, presented herein, to efficiently calculate statically trapped drops in three-dimensional constrictions. During a simulation, the drop surface  $S_d$  advances with a specially designed ‘velocity’  $U_n$ , where the

subscript  $\mathbf{n}$  refers to the outward-normal direction of motion. Tailored as the product of two functions, each relating to the separate portions of the drop surface,  $U_n(\mathbf{x})$  is explicitly calculated, for  $\mathbf{x}$  on  $S_d$ , as

$$U_n(\mathbf{x}) = [C_{YL} + B\mathbf{d} \cdot \mathbf{x} - 2k(\mathbf{x})]F_\delta(\mathbf{x}), \quad (3.1a)$$

where

$$F_\delta(\mathbf{x}) = 1 - \exp[-\lambda\delta(\mathbf{x})]. \quad (3.1b)$$

In (3.1b),  $\delta(\mathbf{x})$  is the distance between a point  $\mathbf{x}$  on  $S_d$  and the nearest intersection on the solid surface in the  $\mathbf{n}(\mathbf{x})$  direction ( $\mathbf{n}(\mathbf{x})$  is the outward unit normal on  $S_d$  at  $\mathbf{x}$ ), and  $\delta$  is subsequently referred to as the drop-solid clearance. The term  $\lambda$  in (3.1b) is a numerical constant used for simulation stability, where  $\lambda = O(1)$  is observed to be optimal. On the R.H.S. of (3.1a),  $k(\mathbf{x})$  is half of the local mean curvature at  $\mathbf{x}$  on  $S_d$ . In (3.1a),  $\mathbf{d}$  is the unit direction of gravity and the isolated drop-settling motion, ignoring solids. In the ‘velocity’ expression (3.1a),  $C_{YL}$  is a constant containing a reference pressure difference across the interface, and is continuously calculated by setting the flux across the drop surface, equal to zero,  $\int_{S_d} U_n(\mathbf{x}) dS = 0$ , due to

volume conservation:

$$C_{YL} = \int_{S_d} \{ [B\mathbf{d} \cdot \mathbf{x} + 2k(\mathbf{x})]F_\delta(\mathbf{x}) \} dS / \int_{S_d} F_\delta(\mathbf{x}) dS. \quad (3.2)$$

With a proper choice of the forcing function  $F_\delta$ , the drop artificially “evolves” to the steady state of a drop trapped in a constriction. The static shape is solved, when  $U_n = 0$  throughout both portions of the drop surface, because  $[C_{YL} + B\mathbf{d} \cdot \mathbf{x} + 2k(\mathbf{x})] \rightarrow 0$  as the drop-fluid interface satisfies the YL equation, and  $F_\delta(\mathbf{x}) \rightarrow 0$  as the drop conforms to the solid. The form of  $F_\delta$  is an

exponentially decaying function, because the drop “evolution” is observed to be both numerically stable and quickly convergent to the steady state.

### 3.2.2 Meshing Details

The initial triangular mesh is created by dividing regular polyhedra faces (i.e. icosaedron and dodecaedron) into triangles and projecting the vertices onto a unit sphere, whereupon further triangle subdivision can be made using previous methods [see Kim & Karrila (1991) and Zinchenko & Davis (2004)]. To avoid numerical instability during the drop motion simulations, the ‘passive mesh stabilization’ technique was employed to maintain triangle quality by introducing a mesh velocity field tangent to the drop surface. The tangential velocity field is calculated iteratively by minimizing a ‘kinetic energy’ of the mesh [Zinchenko & Davis (2002) and (2003)]. From previous boundary-integral studies, the ‘passive mesh stabilization’ technique is adequate for maintaining the overall triangle quality during long simulation times and large drop deformations, when the volume remains intact.

### 3.2.3 Algorithm Details

A drop-surface point  $\mathbf{x}$  is updated by the semi-implicit, Euler equation,  $\mathbf{x}^{v+1} = \mathbf{x}^v + U_n(\mathbf{x}^v)\mathbf{n}(\mathbf{x}^v)\Delta\tau$ , for a “time-interval”  $\Delta\tau$  and subsequent iterations  $v$  and  $v + 1$ . To finish calculating the drop “velocity”  $U_n$ , curvatures and normals  $k(\mathbf{x})$  and  $\mathbf{n}(\mathbf{x})$ , respectively, are calculated by a quadratic approximation of the local drop surface, through fitting using the nearest neighboring vertices of the triangular mesh, as illustrated in Fig. 3.3. A stable “time-interval” ( $\Delta\tau$ ) is calculated at each velocity iteration by using the empirically tested expression

with

$$\Delta\tau = K \frac{\min_i \left\{ \frac{\Delta\mathbf{x}_i}{\max\left(\|k_1(\mathbf{x}_i)\|, \|k_2(\mathbf{x}_i)\|\right)} \right\}}{\quad} \quad (3.3)$$

$\Delta\mathbf{x}_i$  is the shortest distance on  $S_d$  between connecting nodes of the mesh. Also, the denominator in the brackets of Eq. (3.3) is the maximum of the two principal curvatures  $k_1(\mathbf{x}_i)$  and  $k_2(\mathbf{x}_i)$  at  $\Delta\mathbf{x}_i$  and  $K = O(10^{-2}-10^{-3})$  is a constant, empirically-determined to achieve numerical stability .

The surface integrals used in the algorithm are calculated on the triangular mesh by the trapezoidal rule, where for any smooth surface function,  $\phi(\mathbf{x}_i)$ , on  $S_d$ ,

$$\int_{S_d} \phi(\mathbf{x}) dS_x \approx \sum_i \phi(\mathbf{x}_i) \Delta S_i \quad (3.4)$$

where  $\Delta S_i$  is the one-third of the sum of flat-triangle areas sharing a drop vertex  $i$ .

Volume rescaling is performed at each time step during simulation to avoid loss of mass due to numerical error. The drop volume is maintained by scaling the surface in the direction of the drop centroid. Simulation lengths, velocities, and times are nondimensionalized by the undeformed drop radius  $a$ , the magnitude of the isolated-drop “velocity”  $B$  from Eq. (3.1a), and their ratio  $a/B$ , respectively.

### 3.2.4 Solution Details of the Drop-solid Clearances

A key component of the artificial dynamic process used for the 3D YL solution is calculation of the drop-solid clearance normal to the drop surface  $\delta(\mathbf{x}_i)$ , which is illustrated in Fig. 3.3. Beneficially, for both a multi-sphere constriction and a hyperbolic tube,  $\delta(\mathbf{x}_i)$  is analytically calculated for a circular ring, through solving quadratic equations. However, the calculation of  $\delta(\mathbf{x}_i)$  for a ring requires a more computationally costly, two-part iterative scheme, where one part

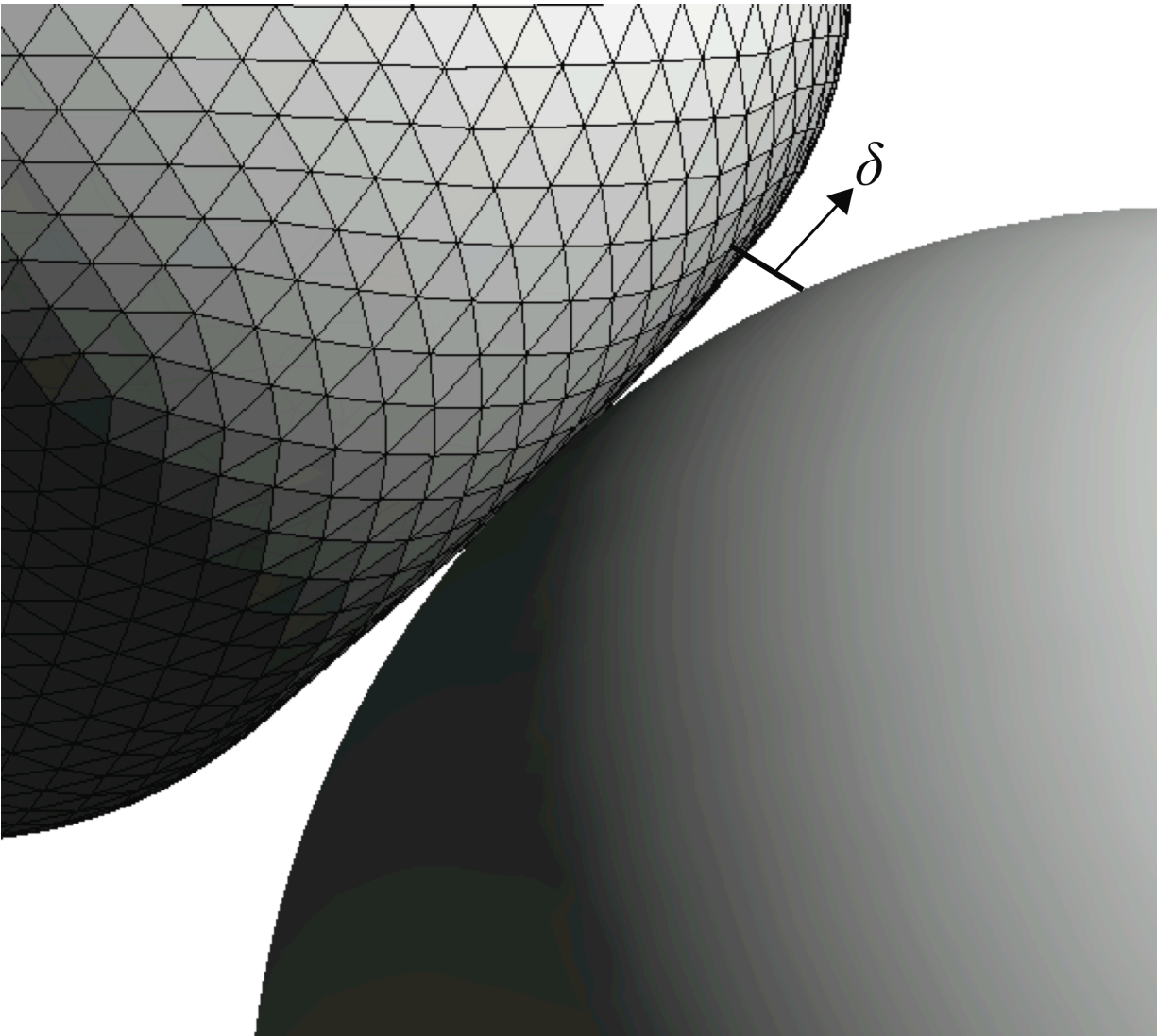


Fig. 3.3: The distance  $\delta$ , in the outward-normal direction to the drop, is between the drop surface, represented by a triangular mesh, and the solid surface, represented by a solid gray surface, with a close-up view.

determines if a solution exists at  $(\mathbf{x}_i)$ , by solving the minimum distance between it and the solid surface. The other part iteratively solves  $\delta(\mathbf{x}_i)$ , either using the previous time-interval solution or the calculated value of  $\delta(\mathbf{x}_i)$ , when the  $\rho$ -coordinate (cylindrical) of  $\mathbf{L}$  is  $b_s^2$  as the initial approximation.

The two-part iterative scheme for a ring is described in detail herein. Initially at  $\tau = 0$ , the drop shape is a sphere and either calculating or determining the existence for  $\delta(\mathbf{x}_i)$  is analytical. For all  $\tau > 0$ , a  $\delta(\mathbf{x}_i)$  scheme proceeds to one of the two iterative calculations, depending on whether or not  $\delta(\mathbf{x}_i)$  existed on the previous time step. So, without a  $\delta(\mathbf{x}_i)$  solution on the previous time step, a one-dimensional Newton method is used to determine the minimum distance between the line in the outward normal direction  $\mathbf{L} = \mathbf{x}_i + q\mathbf{n}(\mathbf{x}_i)$  starting at  $\mathbf{x}_i$ , and the circle formed by rotating the center of the solid cross section of the ring around the axis of symmetry, where the parameter  $q$  represents the positions of the points on  $\mathbf{L}$ . If the above mentioned minimum distance is less than the cross-section of the ring  $a_s$ , then  $\mathbf{L}$  intersects the ring, and  $\delta(\mathbf{x}_i)$  exists. Otherwise,  $\mathbf{L}$  does not intersect the ring, and  $F_\delta(\mathbf{x}_i)$  is set to unity.

The other Newton method determines the square of the minimum distance ( $F(\varphi)$ , where  $\varphi$  is the angle of rotation around the ring in the azimuthal direction) between  $\mathbf{L}$  and the circle, around the axis of symmetry of the center of the solid-ring cross section. The dependent variable  $\varphi$  is iteratively solved as

$$\phi^{v+1} = \phi^v + F_\phi(\phi^v) / F'_\phi(\phi^v) \quad (3.4)$$

The expressions for the minimum distance squared and its derivative  $F_\phi$  and  $F'_\phi$ , respectively, are

$$F_\phi = C_1 \sin^2 \varphi + C_2 \sin \varphi + C_3 \cos \varphi + C_4 \cos \varphi \sin \varphi + C_5, \quad (3.5)$$

$$F'_\varphi = 2C_4 \sin^2 \varphi + 2C_1 \sin \varphi \cos \varphi + C_2 \cos \varphi - C_3 \sin \varphi - C_4, \quad (3.6)$$

with constants  $C_1 = 2b_s n_x n_y$ ,  $C_2 = x_i(1-n_x^2) - n_x(y_i n_y + z_i n_z)$ ,  $C_3 = y_i(n_y^2 - 1) + n_y(x_i n_x + z_i n_z)$ ,  $C_4 = b_s(n_x^2 - n_y^2)$ , and  $C_5 = -b_s n_x n_y$ , and where  $(x_i, y_i, z_i)$  and  $(n_x, n_y, n_z)$  are the Cartesian coordinates of  $\mathbf{x}_i$  and  $\mathbf{n}(\mathbf{x}_i)$ , respectively, with  $\nu$  and  $\nu+1$  representing consecutive iterations of  $\varphi$ ,  $F_\varphi$  and  $F'_\varphi$ . The initial guesses for the integration of  $\varphi$  are either the converged value from the previous time step or, for no convergence, the value where the  $\rho$ -coordinate (spherical coordinates) is  $b_s^2$ . After  $\varphi$  converges, if  $F_\varphi > a_s^2$ , then  $F_d(\mathbf{x}_i) = 1$ , else a solution for  $\delta(\mathbf{x}_i)$  exists.

If either the solution for  $\delta(\mathbf{x}_i)$  existed on the previous time step or if  $\delta(\mathbf{x}_i)$  is shown to exist, then the Newton method in Eq. (3.7) solves for  $\delta(\mathbf{x}_i)$  by

$$\delta^{\nu+1}(x_i) = \delta^\nu(x_i) - F_\delta[\delta^\nu(x_i)] / F'_\delta[\delta^\nu(x_i)], \quad (3.7)$$

where  $\nu$  and  $\nu+1$  are  $\nu^{\text{th}}$  iterations of  $\delta$ ,  $F_\delta$  is the smallest intersection of  $\mathbf{L}$  with the ring, and  $F'_\delta$  is the derivative of  $F_\delta$  with respect to  $\delta$ . The equations for  $F_\delta$  and  $F'_\delta$  are

$$F_\delta = (r - b_s)^2 + L_z^2 - a_s^2 \quad (3.8)$$

$$\text{and} \quad F'_\delta = 2\left((r - b_s)/r\right) * (C_6 n_x + C_7 n_y) + 2n_z C_8, \quad (3.9)$$

where  $L_z$  is the  $z$ -coordinate of  $\mathbf{L}$ ,  $C_6 = x_i + \delta n_x$ ,  $C_7 = y_i + \delta n_y$ , and  $C_8 = z_i + \delta n_z$ . Also, if both more than 8 iterations of  $\delta(\mathbf{x}_i)$  are calculated and the other Newton method has not been used, then the existence of  $\delta(\mathbf{x}_i)$  is checked, before continuing with the calculations in (3.7). By using the two-part iterative scheme, the drop-solid clearances normal to the drop are calculated if they exist, else the forcing function is set to unity.

## 3.4 Results

### 3.4.1 Interaction of the Drop and Solid

The 3D Young-Laplace algorithm was tested using dynamic three-dimensional boundary-integral methods. A drop with a small Bond number is not deformable enough to pass through the constriction, but instead becomes trapped inside the constriction. With a drop-to-hole radius ratio  $a/b_s = 2.8$ , a sphere-to-hole radius ratio  $a_s/b_s = 2.6$ , 8640 triangles on each surface and  $B = 1$ , snapshots at increasing times are shown in Fig. 3.4 (a-c), and Fig. 3.4 (d) shows the steady-state trapped shape. The leading edge of the drop flattens as it settles towards the opening of the three-sphere constriction. Then, the drop velocity decreases considerably as it deforms to enter the constriction. Since the Bond number is less than critical, the drop is not deformable enough to pass through the constriction and a steady state is achieved with the drop trapped in the constriction.

Alternatively, the motion of a drop settling through a three-sphere constriction with the same geometry and number of surface triangles as before but with a higher Bond number of 1.7 is shown at increasing times in Fig. 3.5(a-d). As before, the drop flattens as it settles towards the opening of the reduced constriction. However, the drop deforms more easily as it passes through the constriction. To reduce computational costs, the simulation is stopped once it is clear the drop will pass through.

There is a critical Bond number  $B_{cr}$  that delineates the boundary between the two consequential branches of drop behavior. For the conditions shown in Fig. (3.4) and (3.5), the time-intensive, boundary-integral simulations yield  $B_{cr} \approx 1.5$ .

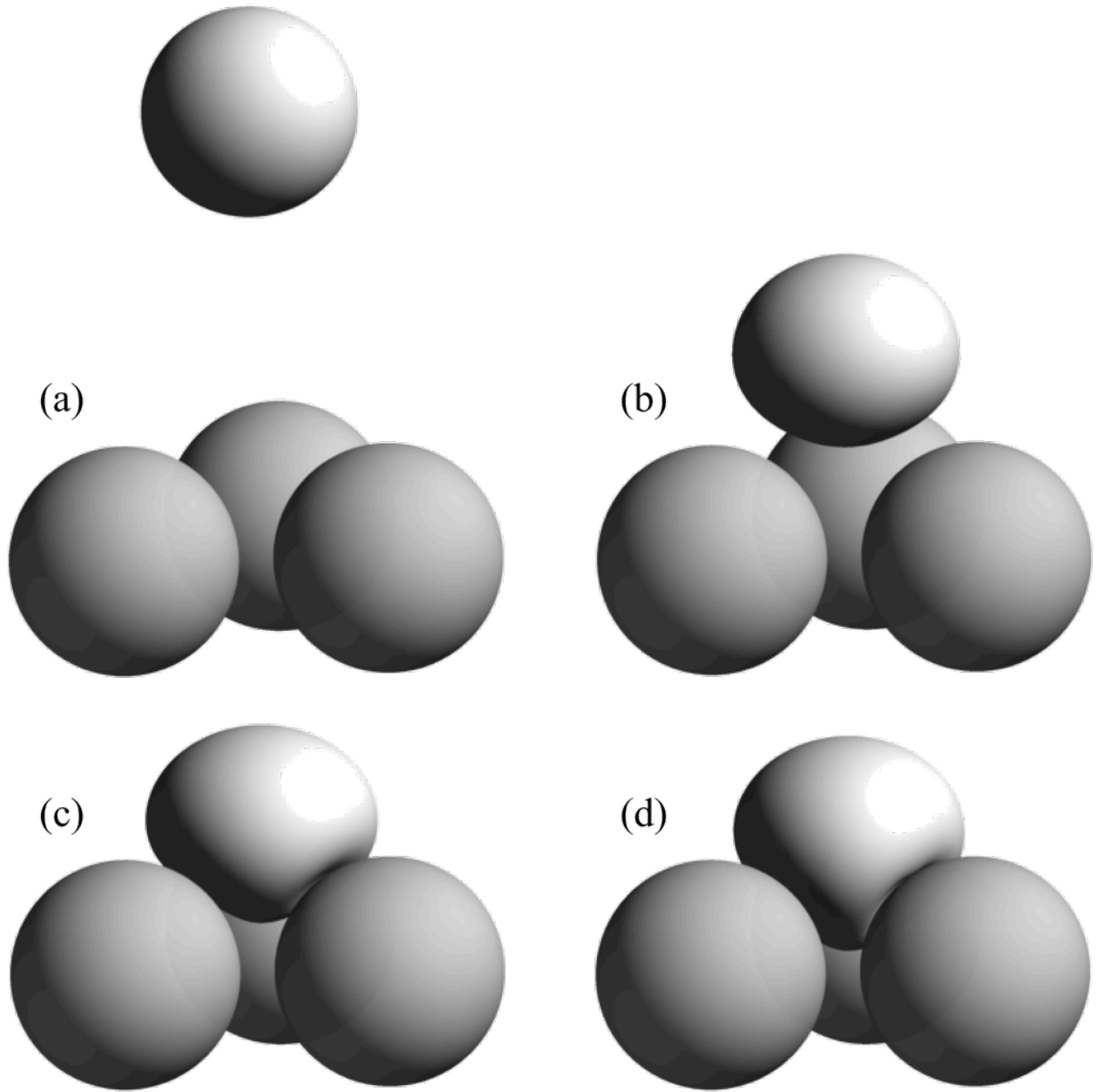


Fig. 3.4: Snapshots of the drop motion approaching three (nearly touching) spheres to the steady-state of trapping using BI algorithm with  $a/b_s = 2.8$ ,  $a_s/b_s = 2.6$ ,  $B = 1$  ( $B_{cr} = 1.42 \pm 0.04$  90% CI) and 8640 triangles used on each surface  $S_d$  and  $S_p$ , respectively at (a)  $\tau = 2.5$ , (b)  $\tau = 6.25$ , (c)  $\tau = 10$  and (d)  $\tau = 100$ .

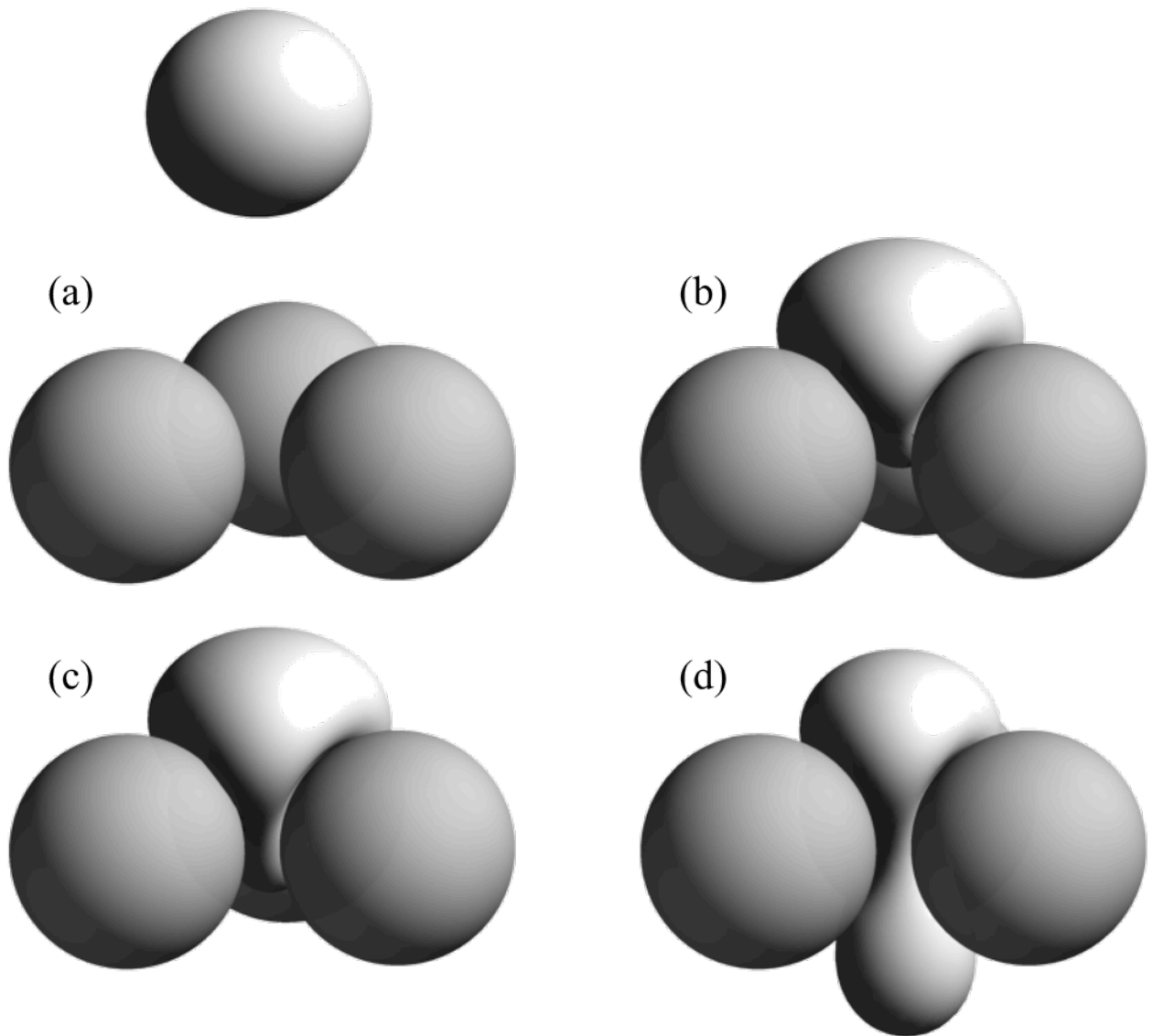


Fig. 3.5: Snapshots of the drop motion approaching three spheres (nearly touching) for squeezing using BI algorithm with  $a/b_s = 2.8$ ,  $a_s/b_s = 2.6$ ,  $B = 1.7$  ( $B_{cr} = 1.42 \pm 0.04$  90% CI) and 8640 triangles used on each surface  $S_d$  and  $S_p$ , respectively at (a)  $\tau = 3.75$ , (b)  $\tau = 25$ , (c)  $\tau = 46.25$  and (d)  $\tau = 67.5$ .

The more efficient and accurate 3D YL algorithm yields  $B_{cr} = 1.42 \pm 0.04$  90% CI. The near-critical, boundary-integral simulations are computationally expensive and highly sensitive to the resolution of both the drop and solid surfaces, due to the small drop-solid clearances. Therefore, our more accurate and efficient 3D YL solution method (and axisymmetric YL algorithm, where appropriate) is used for the remaining calculations of critical Bond numbers.

Next, we examine the behavior of the 3D YL solution method for Bond numbers on both sides of the critical value for a ring constriction, because the results can be easily verified using the highly-accurate, axisymmetric YL algorithm. For Bond numbers less than critical, the artificial dynamic process for the 3D YL solution converges to the steady state of a drop trapped in the constriction. However, for Bond numbers above the critical value, the artificial dynamic process will artificially simulate drop pass-through, due to the lack of a static solution. During the artificial dynamic process, the root mean square (rms) of the specially-designed “velocity” over the drop surface is defined as

$$\text{rms}U_n(\mathbf{x}) = \sqrt{\frac{\int_{S_d} U_n^2 dS}{SA_d}} \quad (3.10)$$

and provides a measure of the rate of drop deformation. In Fig. (3.6),  $\text{rms}U_n$  versus simulation time  $\tau$  is shown using the three-dimensional Young-Laplace algorithm for  $B = 1.8, 1.7, 1.6, 1.5$  and  $1.45$  from top to bottom for two surface resolutions of 5120 and 8640. The velocity curves show excellent agreement for the trials away from the critical Bond number, with increasing sensitivity to resolution is observed near the critical point. In Fig. (3.7)  $\text{rms}U_n$  versus simulation time  $t$  is shown using the three-dimensional boundary-integral algorithm for  $B = 1.75, 1.7, 1.65$  and  $1.6$  from top to bottom for two surface resolutions of either 5120 and 8640 for  $B = 1.75$  and  $1.7$  or 11520 and 15360 for  $B = 1.65$  and  $1.6$ . The boundary-integral algorithm results are more

sensitive to resolution than are the Young-Laplace algorithm results, with much higher surface resolution needed for the boundary-integral trials near the critical point.

Next, using the Young-Laplace algorithm, the critical Bond number ( $B_{cr} = 1.42 \pm 0.02$  90% CI) is extrapolated in Fig. (3.8) by plotting the trend of the minimum observed  $rmsU$  during each trial at the higher resolution versus the Bond number. By comparison, using the boundary-integral algorithm, the critical Bond number ( $B_{cr} = 1.45 \pm 0.07$  90% CI) is extrapolated in a similar fashion in Fig. (3.9) by plotting the trend of the minimum observed  $rmsU$  during each trial at the higher resolution versus the Bond number. Determination of the critical Bond number using both the Young-Laplace and boundary-integral algorithms is easier using supercritical Bond numbers, because large Bond number trials are faster and, by varying the Bond number and observing the minimum of the  $rmsU_n$ , a critical Bond number is easily determined by linear extrapolation to  $B \rightarrow B_{cr}$  as  $rmsU_n \rightarrow 0$ . The difference between the critical Bond numbers extrapolated by the two algorithms are statistically equivalent, and the discrepancy between the mean critical Bond numbers and the uncertainty between the two algorithms is due to a lack of sufficient resolution to accurately obtain minimum  $rmsU$  values near the critical point for the boundary-integral algorithm. Since the Young-Laplace algorithm is less affected by surface resolution and much more computationally efficient, all further critical Bond number extrapolations are made using this algorithm.

Multiple comparisons of critical Bond numbers versus drop size for hyperbolic tubes and rings using both the 3D YL solution method and the highly-accurate axisymmetric algorithm are shown in Fig. (3.10a) and (3.10b) for hyperbolic tubes and rings, respectively, with the curves representing the axisymmetric algorithm results and the symbols representing the 3D YL algorithm results. As observed in Fig. (3.10a) and (3.10b), the 3D YL algorithm results show

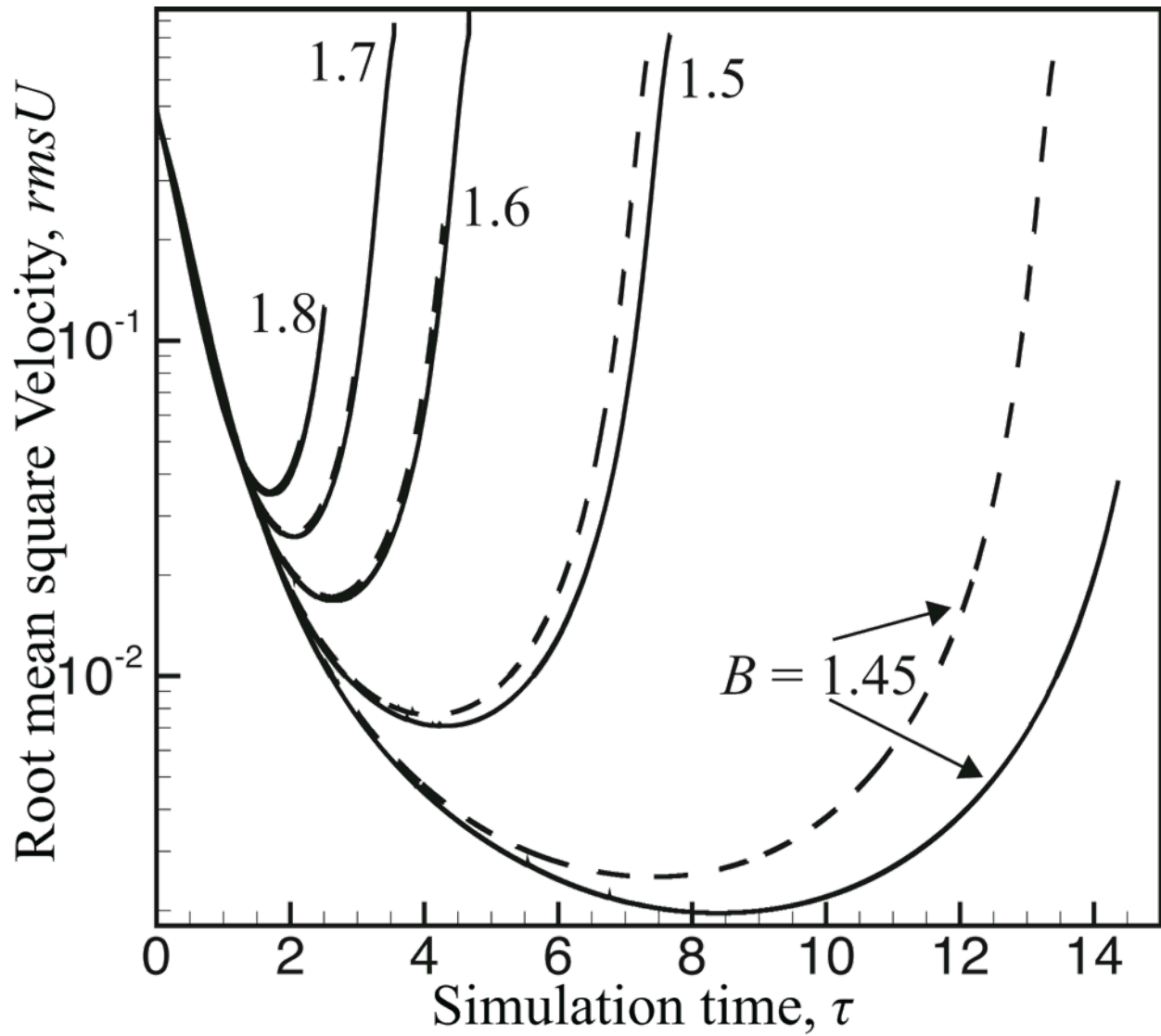


Fig. 3.6: The root mean square velocity of the drop surface versus simulation time using a 3-sphere constriction and the three-dimensional Young-Laplace algorithm with  $a/b_s = 2.8$  and  $a_s/b_s = 2.6$ , for  $B = 1.8, 1.7, 1.6, 1.5$  and  $1.45$  from top to bottom. Simulations using 5120 triangles for the drop surface are represented by solid lines and ones using 8640 triangles for the drop surface are represented by dashed lines.

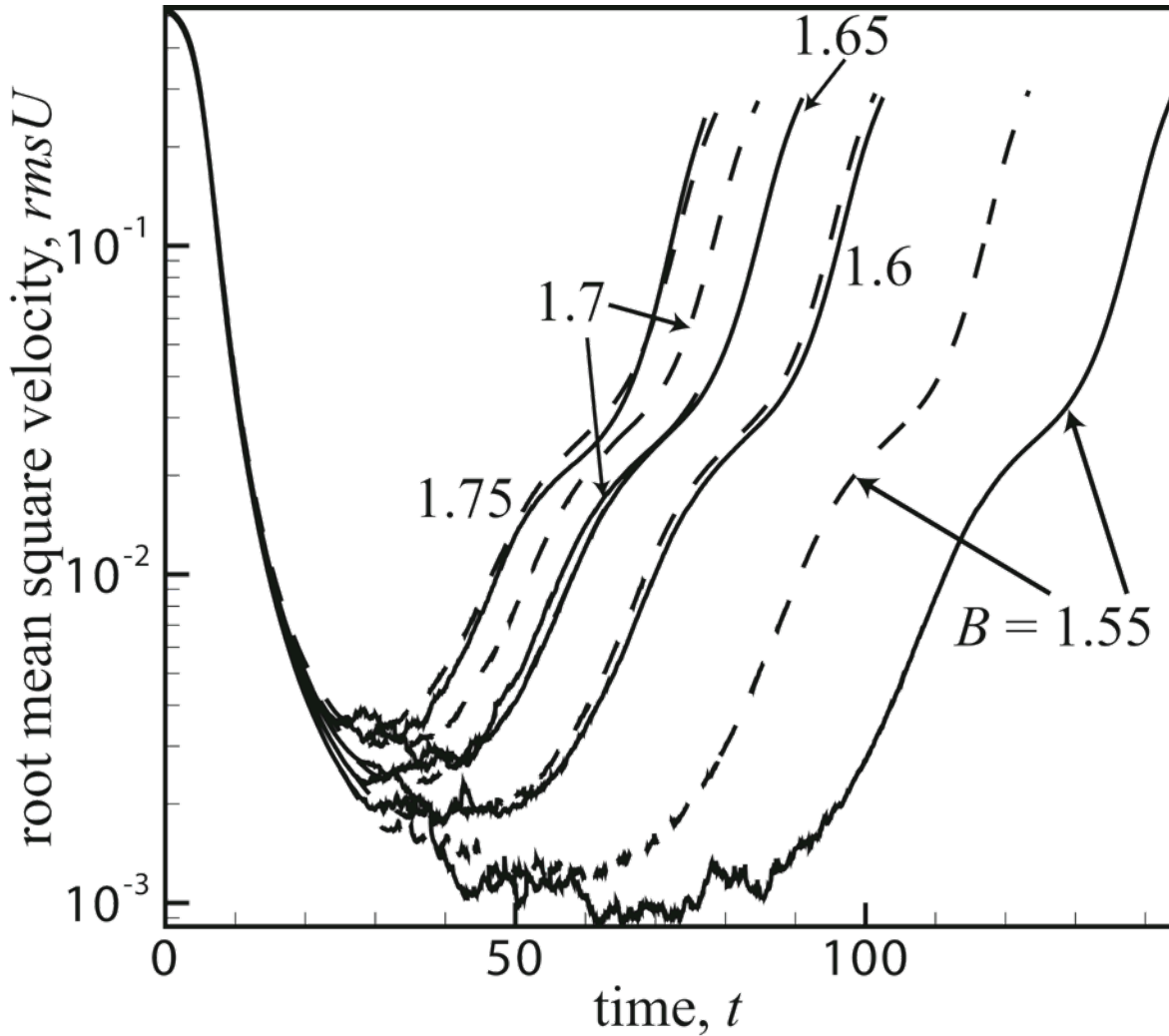


Fig. 3.7: The root mean square velocity of the drop surface versus simulation time using a 3-sphere constriction and the three-dimensional boundary-integral algorithm with  $a/b_s = 2.8$  and  $a_s/b_s = 2.6$ , for  $B = 1.75, 1.7, 1.65$  and  $1.6$  from top to bottom. For  $B = 1.75$  and  $1.7$ , simulations using 5120 triangles on the drop and sphere surfaces are represented by solid lines and ones with 8640 triangles on the drop and sphere surfaces are represented by dashed lines. For  $B = 1.65$  and  $1.6$ , simulations using 11520 triangles on the drop and sphere surfaces are represented by solid lines and ones using 15360 triangles for the drop and sphere surfaces are represented by dashed lines. Of note is that for the two  $B = 1.65$  trials, the two curves are almost identical and are very hard to distinguish.

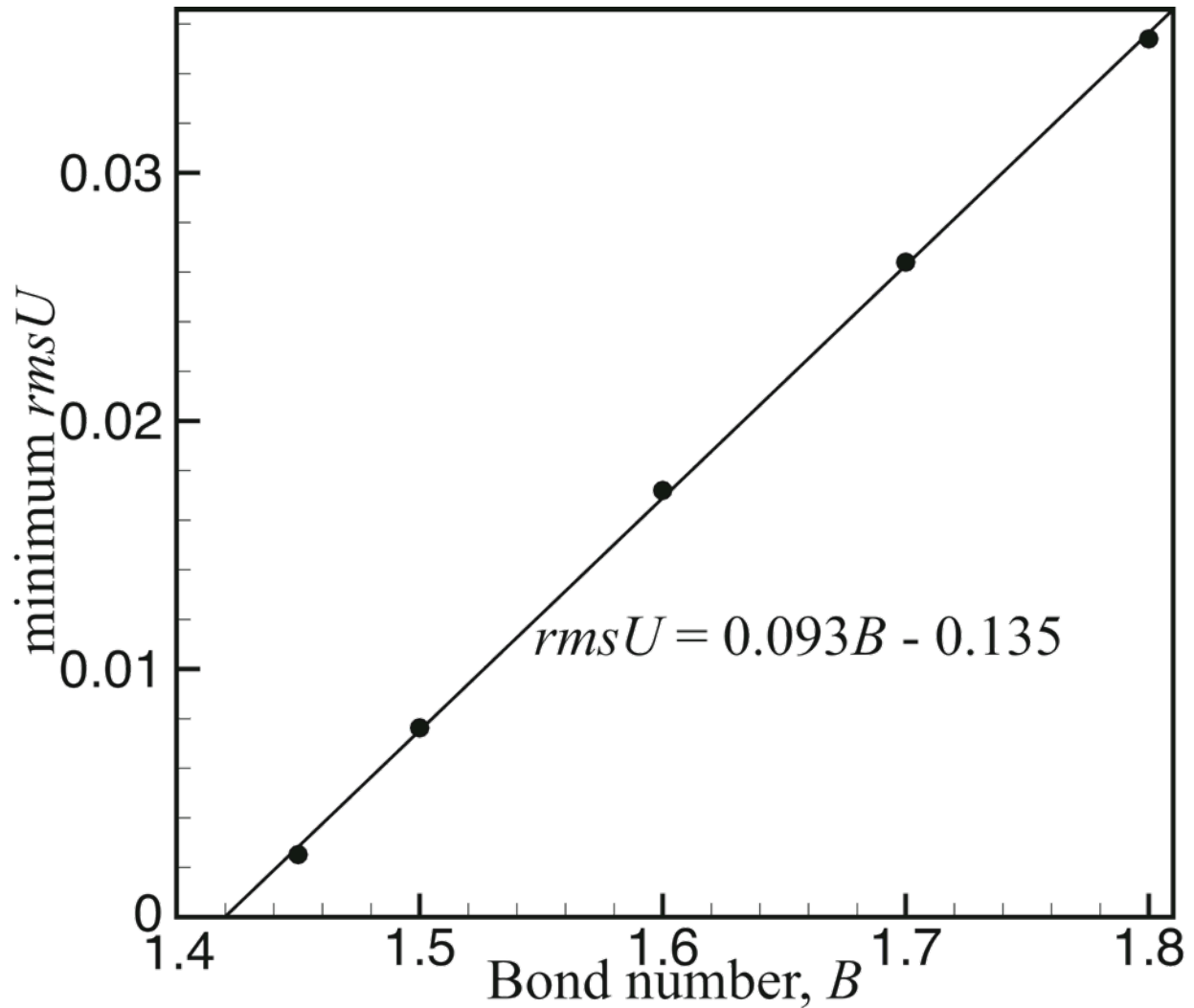


Fig. 3.8: Critical Bond number extrapolation from results using the three-dimensional Young-Laplace algorithm for a 3-sphere constriction with  $a/b_s = 2.8$  and  $a_s/b_s = 2.6$  and 8640 surface triangles representing the drop surface. The minimum observed root mean square velocity during each simulation versus Bond number is shown with solid circles representing simulation results and the line representing the extrapolation curve. The resulting critical Bond number determined is  $B_{cr} = 1.42 \pm 0.04$  90% CI.

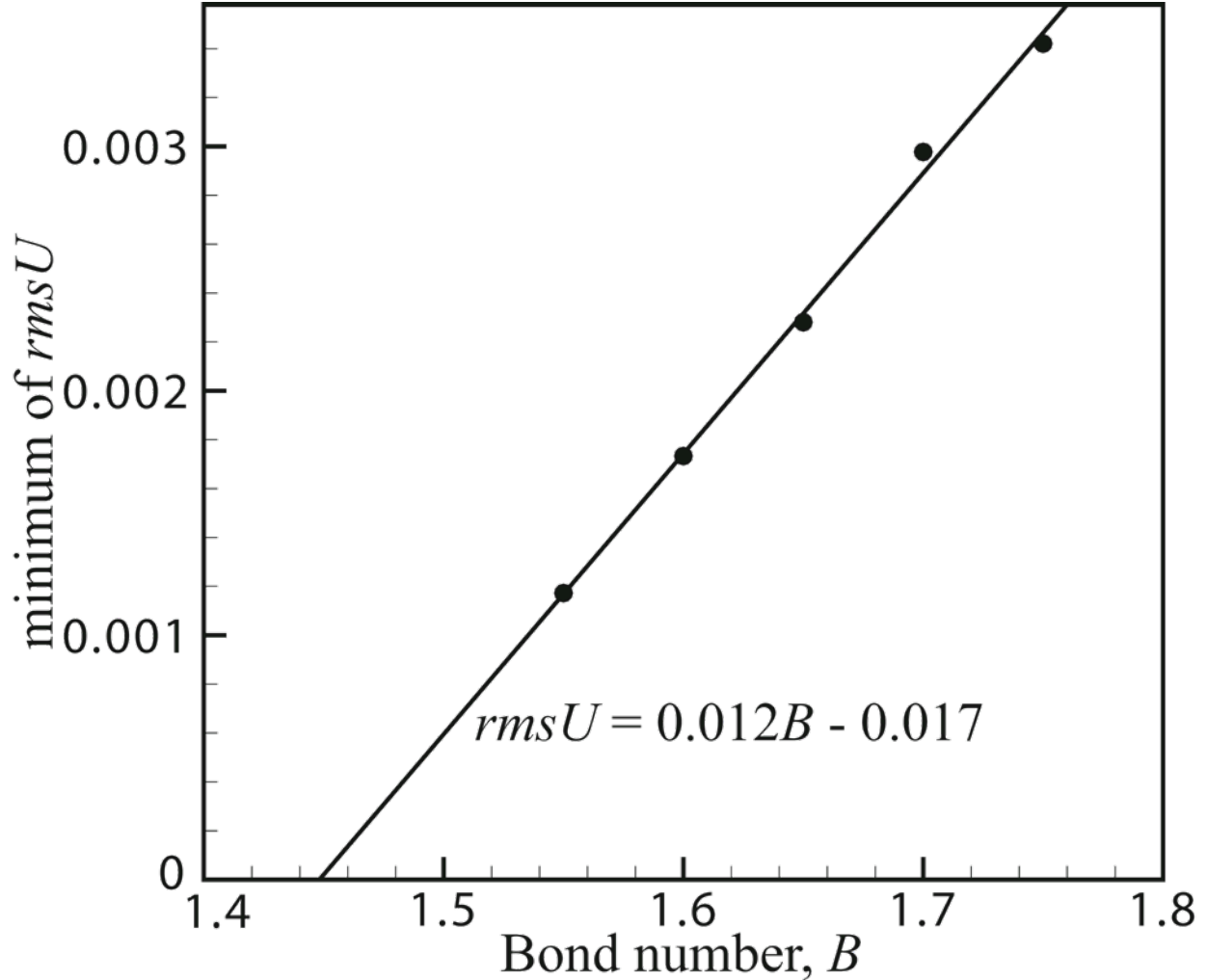


Fig. 3.9: Critical Bond number extrapolation from results using the three-dimensional boundary-integral algorithm for a 3-sphere constriction with  $a/b_s = 2.8$  and  $a_s/b_s = 2.6$  and 8640 or 15360 surface triangles representing the drop and solid surfaces. The minimum observed root mean square velocity during each simulation versus Bond number is shown with solid circles representing simulation results and the line representing the extrapolation curve. The resulting critical Bond number determined is  $B_{cr} = 1.45 \pm 0.07$ .

excellent agreement with the highly-accurate results from the axisymmetric algorithm, and the difference between the two methods falls within the uncertainty of the extrapolation. Not only do the critical Bond numbers compare favorably for the two algorithms, but the static shapes for trapped drops are in excellent agreement as shown in Fig. (3.10) for a hyperbolic tube constriction and three subcritical Bond numbers.

### 3.4.2 Effect of Constriction Shape and Tilt Angle

Through use of the 3D YL algorithm, multiple factors affecting the critical Bond number, separating trapping from squeezing, were studied in detail. Understanding which conditions lead to trapping or to squeezing is necessary for the proper design of a system that has a drop settling through a constriction. The critical Bond numbers of multiple constriction types, including rings, hyperboloids and both three and four spheres, are shown in Fig. (3.12). As was seen, the critical Bond number increases with the drop-to-hole size ratio, as more deformation is needed for the drop to squeeze through a smaller hole. Remarkably, the critical Bond number only weakly depends on the shape of the constriction. As also seen in Fig. (3.10b), there are some modest differences based on the geometry of the constriction. For example, a drop squeezes more easily through a 3-sphere constriction than a 4-sphere constriction, with the same hole radius  $b_s$ , presumably because the projected area of the hole in the plane normal to gravity is larger for 3 spheres than for 4 spheres.

For the hyperboloid constriction, we also studied the effect of the angle ( $\alpha$ ) between the gravity vector and the center axis of the tube on the critical Bond number for the trapping of a drop in hyperbolic tubes. The trends for the critical Bond number versus the drop-to-hole size ratio are shown in Fig. (3.13) for a hyperbolic tube with  $c_s/b_s \approx 0.84$  and multiple tilt angles

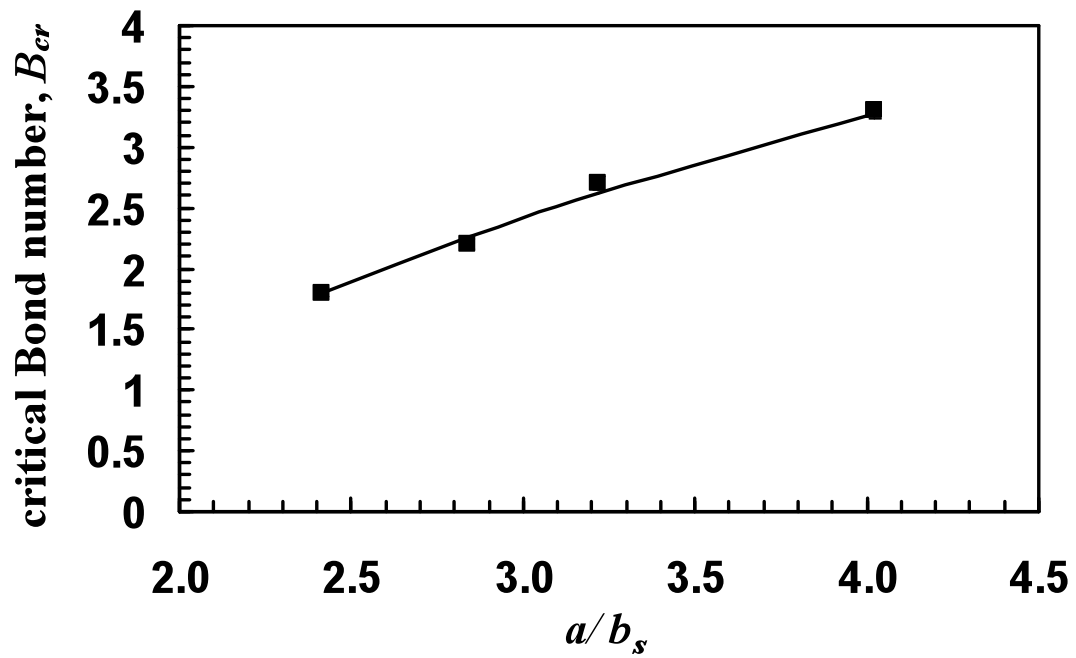


Figure 3.10 (a) Critical Bond number versus drop-to-hole size ratio for hyperbolic tube constrictions with  $c_s \approx 0.26$ ; the solid curve represents results from the highly accurate axisymmetric method and the square symbols represent 3D YL algorithm results.

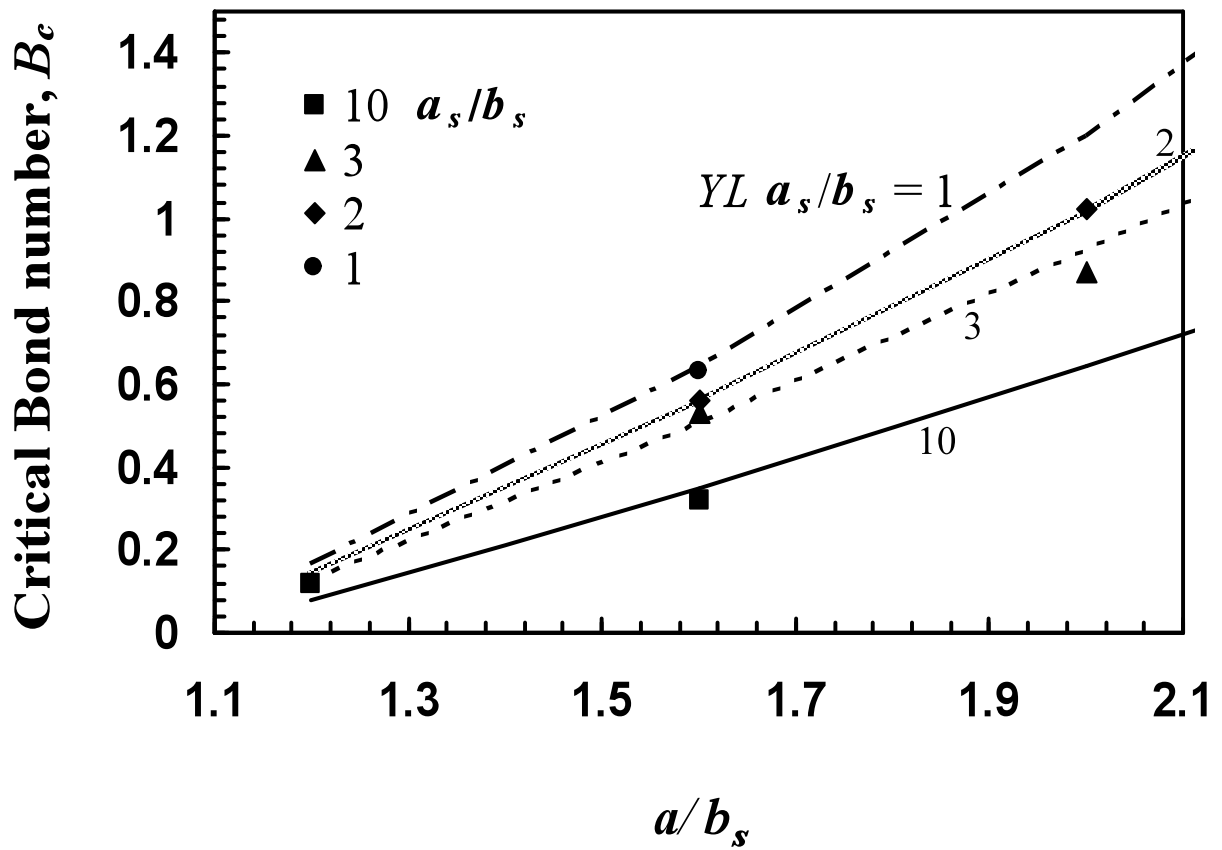


Figure 3.10 (b) Critical Bond numbers versus drop-to-hole size ratio for ring constriction; the curves represent results from the highly-accurate, axisymmetric method and the symbols represent 3D YL algorithm results.

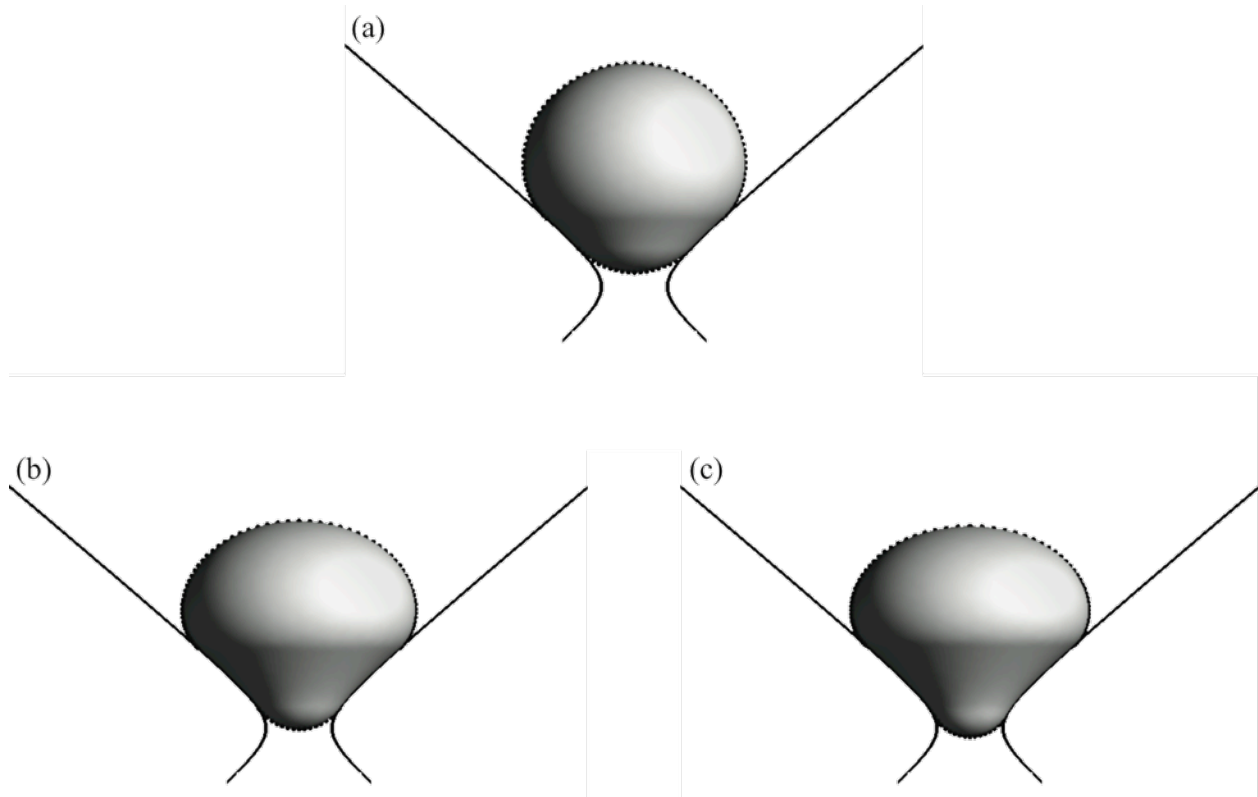


Fig. 3.11: The 3D YL algorithm and the highly-accurate axisymmetric YL algorithm are compared for drop shapes statically trapped in a hyperbolic tube, with solid black curves representing the cross-section of the tube, gray surfaces representing drop shapes from the 3D algorithm, and dotted curves representing the drop contours from the axisymmetric algorithm using geometry parameters  $a/b_s \approx 3.22$  and  $c_s/b_s \approx 0.84$ , and using 8640 triangles for all the 3D drop shape calculations, and with (a)  $B = 0.5$ , (b)  $B = 1.5$  and (c)  $B = 2$ . The critical Bond number is  $B_{cr} = 2.62$ .

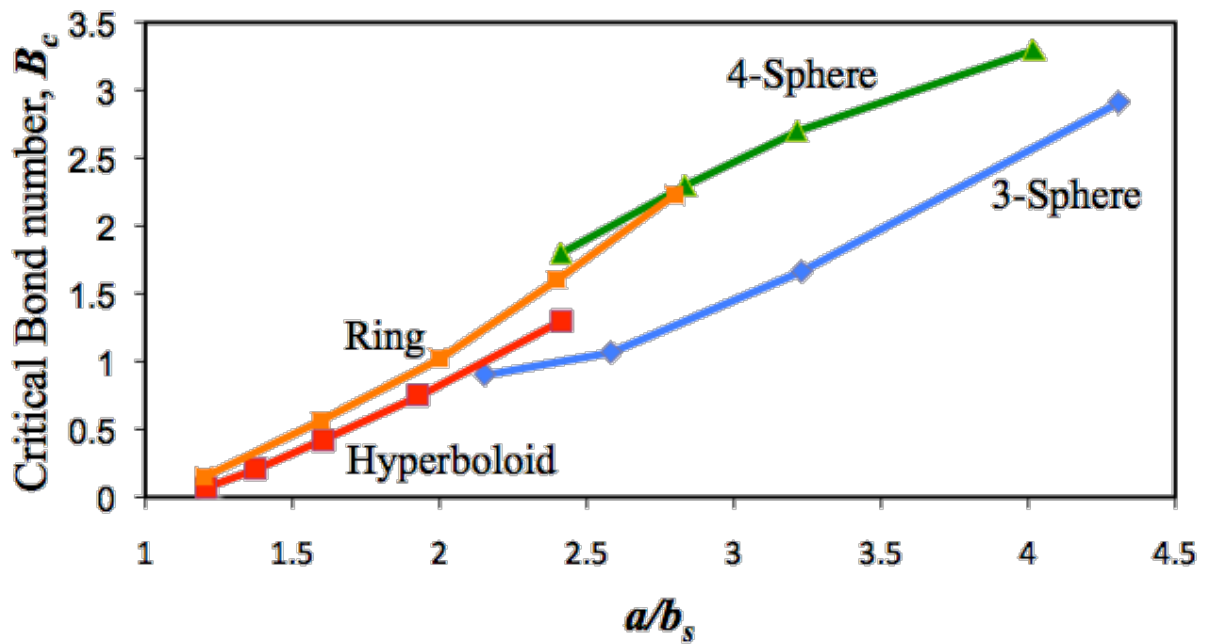


Fig. 3.12: Critical Bond numbers versus the drop-to-hole ratio for multiple constrictions including a ring with  $a_s/b_s = 2$ , a hyperbolic tube with  $c_s/b_s \approx 0.52$ , four spheres (touching) with  $a_s/b_s \approx 6.5$ , and three spheres (touching)  $a_s/b_s \approx 2.4$ .

including  $\alpha = 0^\circ, 5^\circ, 10^\circ$  and  $25^\circ$ . An overall observation of the data is that the tilt angle has only a small effect on the critical Bond number, and with the difference falling within the uncertainty of the extrapolation at  $\alpha = 0^\circ$  and  $5^\circ$ . Surprisingly, the data in Fig. (3.10) show that increasing the tilt angle decreases the critical Bond number. Physically, for constrictions at a small tilt, the minimum hole size perpendicular to the motion of the drop does not change much and so the critical Bond number only changes slightly from the value for a constriction without a tilt. However, for constrictions with larger tilt angles (i.e.  $10^\circ$  and  $25^\circ$ ), the minimum hole size in a plane perpendicular to gravity increases with increasing tilt angle, so a drop requires less force to squeeze through a constriction with a tilt, and the critical Bond number is lowered.

In addition to determining the critical Bond number, the shapes of trapped drops are analyzed for the tilted hyperboloid constrictions (Fig. 3.14). For the low Bond number 0.5, the drop deforms by a small amount, rests on the lower constriction surface, and only slightly protrudes into the hole. For  $B = 1$ , the drop is more deformable, so it flattens on the bottom surface of the constriction and protrudes slightly more into the hole. With  $B = 2$ , which is slightly below  $B_{cr} = 2.1$ , the drop is very deformable and spreads on the lower surface of the constriction so that the leading edge occupies the entire hole of the constriction. It is clear that the last case is near the critical value, because, if the drop becomes more deformable, then the leading edge should pass through the hole and bring with it the rest of the drop. The last still is a blow-up of the leading edge of the drop shape with  $B = 2$ , showing the triangular mesh of the drop surface.

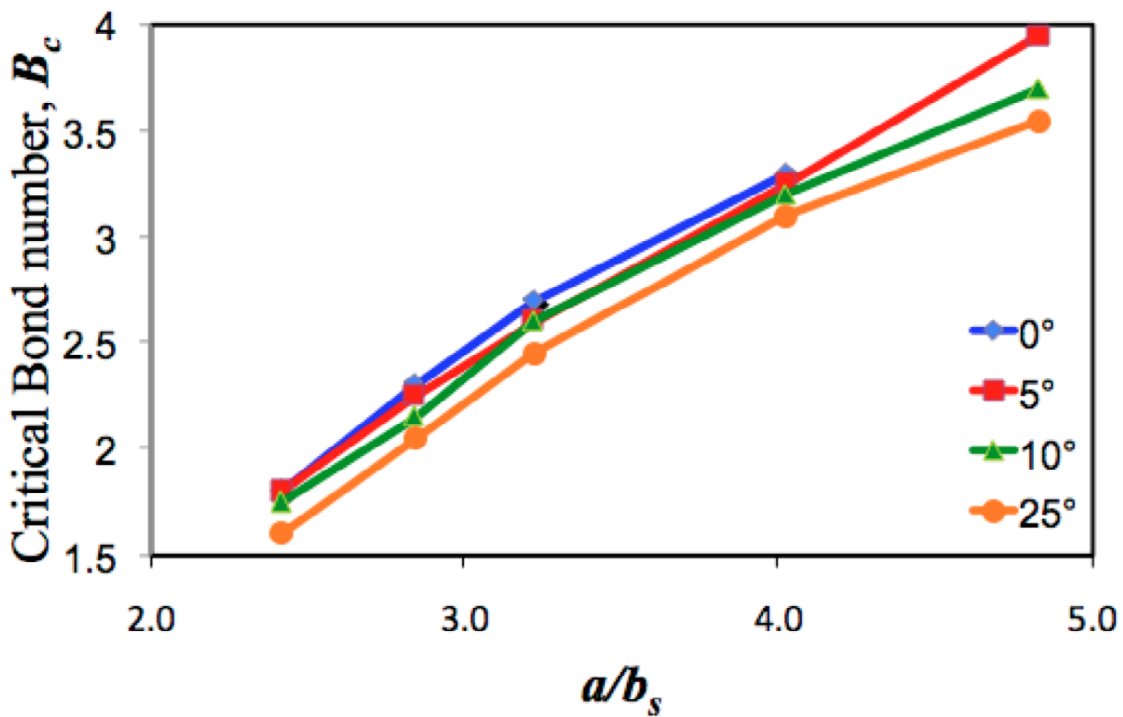


Fig. 3.13: Critical Bond numbers versus drop-to-hole size ratio for hyperbolic tubes with  $a_s/b_s \approx 0.52$  and tilt angles  $\alpha = 0, 5, 10$  and  $25^\circ$ , from top to bottom.

### 3.5 Concluding Remarks

The modeling of deformable drops settling through solid constrictions is numerically challenging, especially near the critical conditions, as it is a problem of high lubrication sensitivity when the drop is very close to the solid. While results from boundary-integral simulations could be used to extrapolate the critical Bond number, separating trapping and squeezing phenomena, these results are computationally expensive. Such simulations would require extremely fine resolutions of both the drop and solid surfaces to accurately calculate the hydrodynamics, due the small drop-solid clearances observed during the buoyancy-induced drop motion. Therefore, a special algorithm, based on the Young-Laplace equation, to calculate the static shape of a drop trapped in a three-dimensional constriction and to determine the critical conditions is useful to avoid the challenges of the boundary-integral simulations.

Instead of simulating the full hydrodynamics, an artificial evolution of the drop shape and position converges asymptotically to the static shape trapped in a three-dimensional constriction. The algorithm simultaneously determines both the drop fluid-fluid interface by the Young-Laplace equation and the fluid-solid interface by conforming to the shape of the constriction.

One major advantage of the current algorithm is that the area where the drop is in near contact with the solid is directly calculated, through use of the specially designed velocity, without requiring empirical data or an iterative solution. For use in the artificial velocity, the local mean curvature and surface normal at a mesh point on the drop surface are found, through representing the local surface by using nearest neighboring mesh points to fit a quadratic approximation. The mesh quality of the drop is maintained during the simulation by using a tangential mesh velocity. The present three-dimensional Young-Laplace algorithm is more efficient and accurate than boundary-integral algorithm, because the solution of the artificial

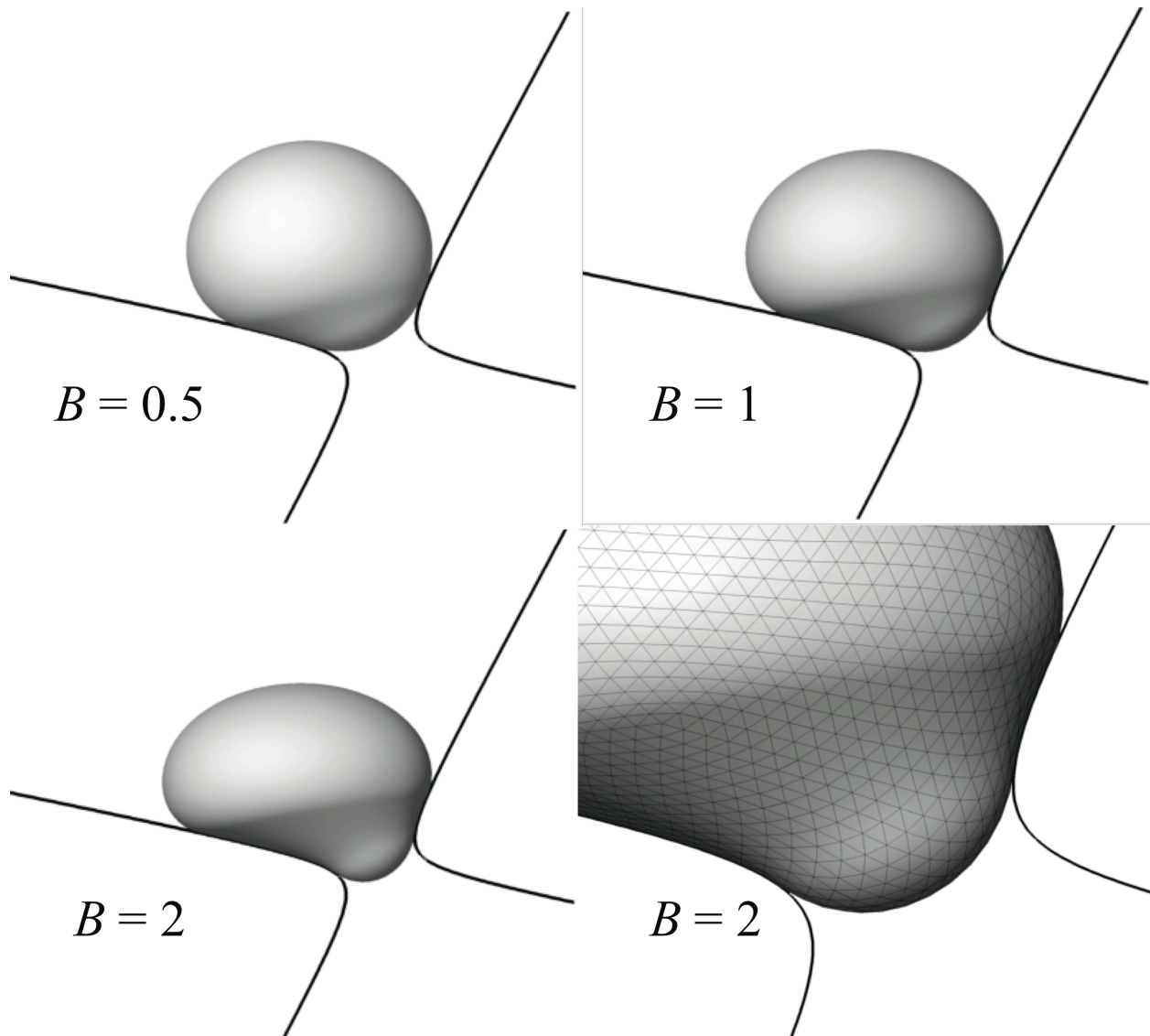


Fig. 3.14: Static drop shapes trapped in a hyperbolic tube, represented by solid black lines with  $a/b_s = 2.84$ ,  $c_s/b_s = 0.84$  and tilt angle  $\alpha = 25^\circ$ , and  $B = 0.5$ , 1 and  $B = 2$ , with a close-up view of the  $B = 2$  case showing the triangular meshing and leading edge protruding into the hole. The critical Bond number is  $B_{cr} = 2.1$

velocity at each location on the drop surface is explicit, instead of requiring numerical surface integration, and only the drop position has to be resolved instead of the full hydrodynamics on both the drop and solid constriction.

A key dimensionless parameter is the Bond number, representing the ratio of gravitational and interfacial forces. Drops with higher Bond numbers are more deformable, and so are able to squeeze through a constriction. Conversely, drops with small Bond numbers are less deformable and become trapped in the constriction.

The critical Bond number increases nearly linearly with the drop-to-hole size ratio, as a drop must be more deformable to pass through a smaller hole, and is only weakly affected by the shape of constriction. Also, the tilt angle of the constriction weakly affects the critical Bond number, which remains nearly unchanged for small tilt angles. Interestingly, the critical Bond number decreases with increasing tilt angle, because the minimum hole size perpendicular to gravity increases with increasing tilt angle. The static drop shapes trapped in a constriction show that a drop remains nearly spherical at small Bond numbers, but a drop with larger Bond number is more spread out on the lower constriction wall and the leading-edge protrudes into the hole. The critical point of trapping is when the drop is deformable enough for the leading edge to completely pass through the hole, pulling the rest of the drop through.

Currently, it is not clear how to extend the three-dimensional Young-Laplace solution method to handle a trapped drop with an arbitrary contact angle. For contact angles not equal to  $180^\circ$ , difficulties will arise in a three-dimensional numerical scheme from the need to accurately calculate the three-phase contact curves and to achieve stability of the artificial evolution of the drop, when the steady-state has a discontinuity in the second derivative of the drop surface at the

contact line. Our hope is that future research efforts will overcome the challenges of calculating the shape of a drop trapped in a three-dimensional constriction with an arbitrary contact angle.

Of future research interest is developing a special algorithm for calculating the static drop shape trapped in constriction due to an external flow. Presently, it is not clear how to model the drop-solid fluid gap, due to the external flow, with the static solution of the drop shape.

Also, it is of interest to apply the present methods to calculate the trapped shape of a static, deformable drop in a solid constriction with an arbitrary wetting angle, instead of  $180^\circ$  in this work, at the three-phase boundary. Presently, it is not clear how to handle the discontinuity of the second derivative of the drop surface, at the point of departure for the drop from the solid surface. It is our hope that future-research efforts will overcome the difficulty imposed from an arbitrary wetting angle, and study the consequential effects on the shape of a drop trapped in a solid constriction and the critical conditions.

## Chapter 4

### Experimental observation of drop squeezing and trapping

#### Abstract

Drop squeezing and trapping mechanisms were observed experimentally in both a ring and an agglomerate of three spheres. The measured critical Bond numbers and trapped drop shapes compare favorably with theoretical calculations from the axisymmetric and three-dimensional Young–Laplace algorithms, respectively. For tightly-packed spheres, the sphere radius scales with the square root of the Bond number for constant material, drop properties and drop-to-hole size ratios. This scaling is useful for designing systems of emulsions settling through tightly packed solids.

#### 4.1 Introduction

To confirm the validity of the computational results, experimental studies were performed to observe gravity-driven drop squeezing and trapping through a constriction. The goal of the experiments is to capture squeezing and trapping dynamics and determine critical Bond numbers for comparison with the axisymmetric and three-dimensional YL algorithms.

## 4.2 Materials and Methods

The experimental apparatus is composed of a small tank ( $10 \times 15 \times 15$  in.<sup>3</sup>) filled with canola oil. Two different constrictions are used. First, a rubber O-ring constriction is suspended using white, 100% polyester threads tied down to supports that allow for fine adjustments in the thread tension. Second, an agglomerate of three, acrylic spheres, which are touching, is shown in Fig. 4.1. The agglomerate of touching, acrylic spheres was formed by using the solvent ProWeld<sup>®</sup>, containing methanol chloride, as “glue.” Small acrylic bridges connect the spheres forming the agglomerate, and a small rubber band is placed around the exterior perimeter of the spheres at their equators for support. We know from our previous experimental and theoretical knowledge [Ratcliffe *et al.* (2010)], that, for the current agglomerate ( $a_s/b_s \approx 6.48$ ), static drop shapes that drip around the outside perimeter of the sphere equators and possibly come into contact with the rubber band will not be observed. Therefore, in the present experiments, it is a reasonable assumption that the presence of the rubber band will not affect the statically trapped drop shapes or critical Bond numbers. Due to their static nature, these calculations are only affected by the solid surface in near contact with the drop. Thin polyester strings are glued to both the rubber band and the agglomerate exterior perimeter at the equator, and the agglomerate is suspended by tying strings, outside the tank, which allow for fine adjustment. Both the rubber O-ring constriction and the agglomerate of three spheres are suspended in the viscous canola oil at the center of the tank so that the walls of the tank, do not interact with the drop.

Deformable drops used in experiments are composed of water-glycerol mixtures, including 100%, 75%, and 16% by weight water, and drop delivery was performed using Hamilton gas-



Fig. 4.1: The experimental agglomerate of three, acrylic Spheres (touching), with a dimensional sphere radius  $a_s \approx 0.95$  cm. Since  $a_s/b_s \approx 6.46$  for three touching spheres, the radius of the circle that just touches each sphere at the mid-plane location within the constriction is  $b_s \approx 0.15$  cm.

tight syringes with sizes of 100, 250  $\mu\text{l}$  and 1  $\text{ml}$ . Drop stills were captured using a Nikon Coolpix<sup>®</sup> digital camera. Temperature was recorded for the physical property measurements and tight syringes with sizes of 100, 250  $\mu\text{l}$  and 1  $\text{ml}$ . Drop stills were captured using a Nikon Coolpix<sup>®</sup> digital camera. Temperature was recorded for the physical property measurements and at the start of each laboratory session (22–23°C) for the O-ring trials and (21–22°C) for the 3-sphere trials.

The fluid density ( $\rho_e$ ) of the canola oil was measured using hydrometers, and the density ( $\rho_d$ ) of the water-glycerol solution was determined from a temperature versus density relation obtained from the work of Adamenko *et al.* (2006). Interfacial tension  $\sigma$  was measured by the drop-weight method described in Davies & Rideal (1963). Viscosities were determined using a Cannon Fenske viscometer for canola oil ( $\mu_e$ ), and viscosity values for water-glycerol solutions ( $\mu_d$ ) were taken from the literature [Stengel *et al.* 1982]. To determine the critical Bond number, the O-ring or 3-sphere geometry is set ( $a_s/b_s$  is constant) and the drop size is slowly increased ( $a/b_s$  increases) to observe the region where drop squeezing transitions to drop trapping. Physical properties of the drop phases and bulk phase used in the experiments are shown in Table 4.1, and the O-ring sizes and resulting  $a_s/b_s$  values are shown in Table 4.2.

## 4.3 Experimental results

### 4.3.1 O-ring constriction

First, drop squeezing and trapping are observed in Figs. 4.2 and 4.3, respectively. The two figures have the same drop and ring sizes, but Fig. 4.2 is for a drop of 75% water and 25% glycerol, while Fig. 4.3 is for a pure-water drop. Squeezing occurs for the former, where the

Table 4.1: Properties of the three water-glycerol/canola oil systems used in experiments.

System	wt. %	$\mu_d, \mu_e$	$\rho_d, \rho_e$	$\sigma$	$T$
	H <sub>2</sub> O	(g cm <sup>-1</sup> s <sup>-1</sup> )	(g cm <sup>-3</sup> )	(dyn cm <sup>-1</sup> )	(°C)
1	100	0.0096, 0.72	1.00, 0.91	20	22
2	75	0.0184, 0.72	1.03, 0.91	17	22
3	16	0.748, 0.72	1.20, 0.91	14	22

Table 4.2: O-ring sizes and the resulting  $a_s/b_s$  values used in experiments.

O-ring	O.D. (cm)	I.D. (cm)	$a_s/b_s$
1	0.70	0.275	0.773
2	0.75	0.274	0.864

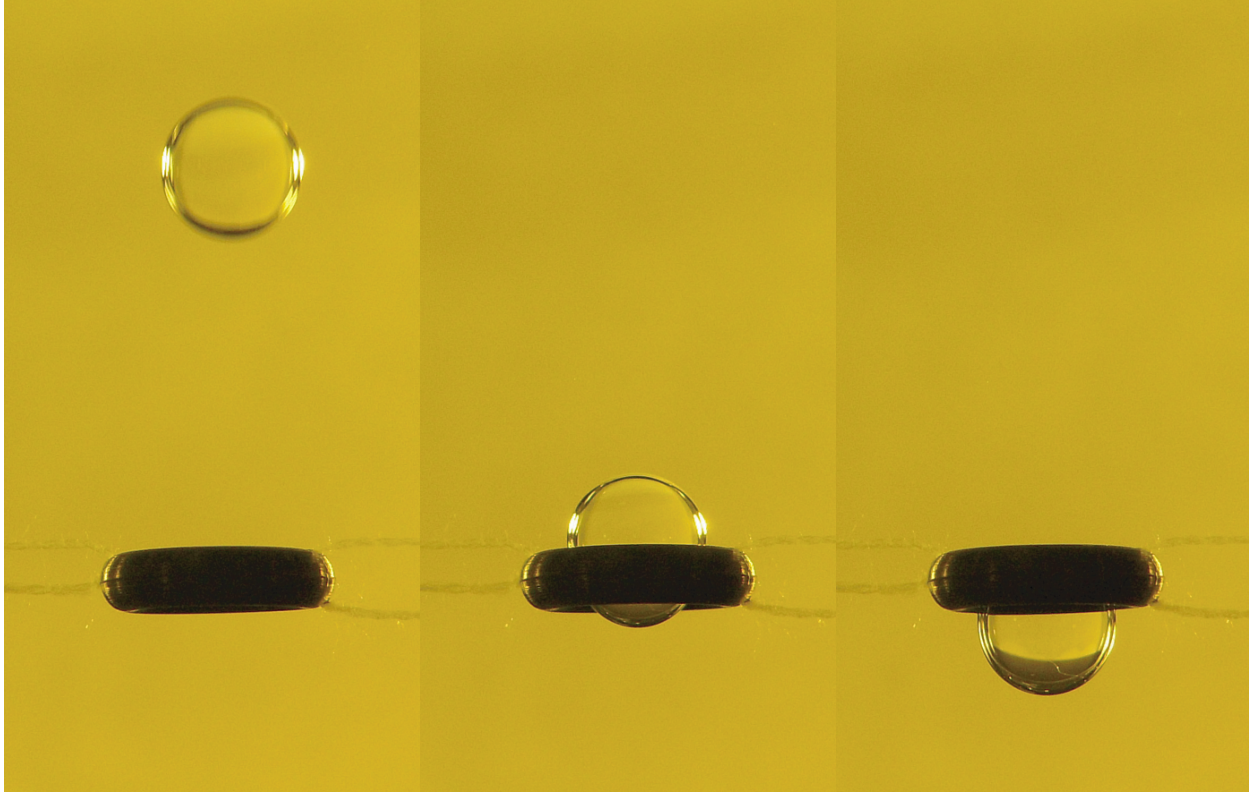


Fig. 4.2: Experimental stills of a 75% water drop squeezing through an O-ring constriction with  $a/b_s = 1.22$ ,  $a_s/b_s = 0.567$ ,  $\mu_d/\mu_e = 0.026$ , and  $B = 0.29$ ; the successive photos were taken about 2 s apart.



Fig. 4.3: Experimental stills of a 100% water drop being trapped in an O-ring constriction with  $a/b_s = 1.22$ ,  $a_s/b_s = 0.567$ ,  $\mu_d/\mu_e = 0.013$ , and  $B = 0.21$ ; the first three drop stills were taken about 2 s apart, and the last still was taken after a 20 s interval.

latter has a lower density and higher interfacial tension, leading to a smaller Bond number and trapping.

Next, the critical Bond number is determined experimentally by increasing the drop size ( $a/b_s$ ) until trapping is observed. As observed in Fig. 4.4 for water drops, the experimentally-determined  $B_c$  values show very good agreement with theory. Increasing the hole size at nearly constant ring cross section [O-rings 2–4 from Table 4.2] requires larger drop sizes and critical Bond numbers for trapping. In contrast, increasing the ring cross section while keeping the hole size constant [O-rings 1 and 2 in Table 4.2] has little effect on the critical drop size and Bond numbers; this experimental result confirms the model prediction that the critical Bond number is only weakly dependent on the cross-sectional size in this parameter range.

In Fig. 4.5, the effect of the drop fluid on the critical Bond number is observed for three different fluid compositions. With increasing amount of glycerol, the surface tension decreases and the density difference increases [Table 4.1], so that the Bond number and its critical value increase. For the fluid with only 16% water, the drop is sufficiently deformable that trapping does not occur.

In Fig. 4.6, the predicted shape using the axisymmetric YL algorithm is overlaid on a photo of a trapped drop from the experiments for the same parameters. Again, the experimental trapped drop shape is in good agreement with theory, and it validates the not-wetting assumption in the axisymmetric YL algorithm.

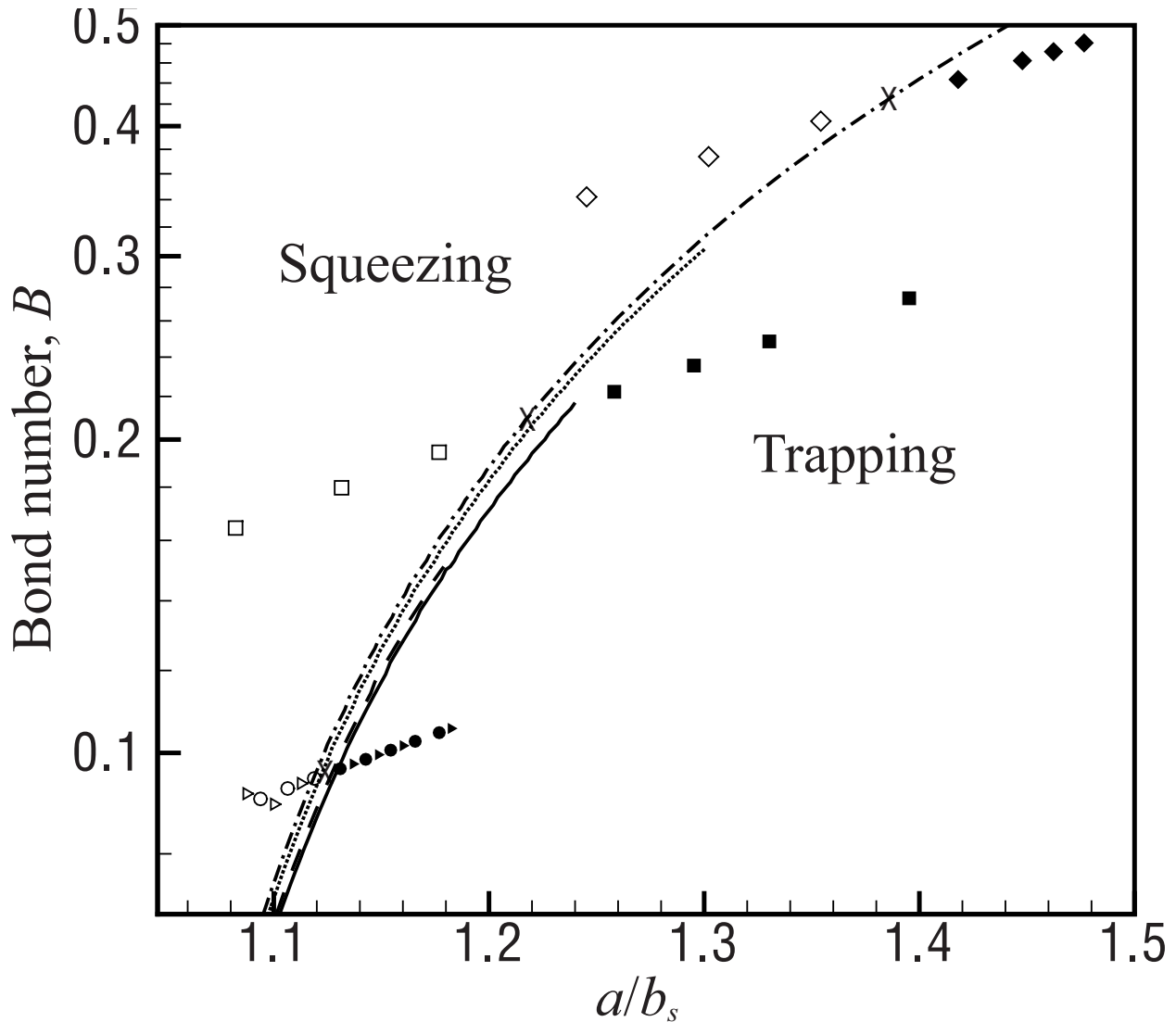


Fig. 4.4: Experimental determination of the critical Bond number for different ring sizes using 100% water drops and the four different O-rings from Table 4.2: O-ring 1 with  $a_s/b_s = 0.773$  (theoretical  $B_c$  is dashed curve and triangles represent drop sizes), O-ring 2 with  $a_s/b_s = 0.864$  (theoretical  $B_c$  is solid curve and circles represent experimental drop sizes), O-ring 3 with  $a_s/b_s = 0.567$  (theoretical  $B_c$  is dotted curve and squares represent experimental drop sizes), and O-ring 4 with  $a_s/b_s = 0.444$  (theoretical  $B_c$  is dashed-dotted curve and diamonds represent experimental drop sizes). The open symbols are for drops that pass through the O-ring, the closed symbols are for drops that become trapped in the O-ring, and the  $\times$  symbols are for drop sizes where both trapping and squeezing are observed in repeated trials.

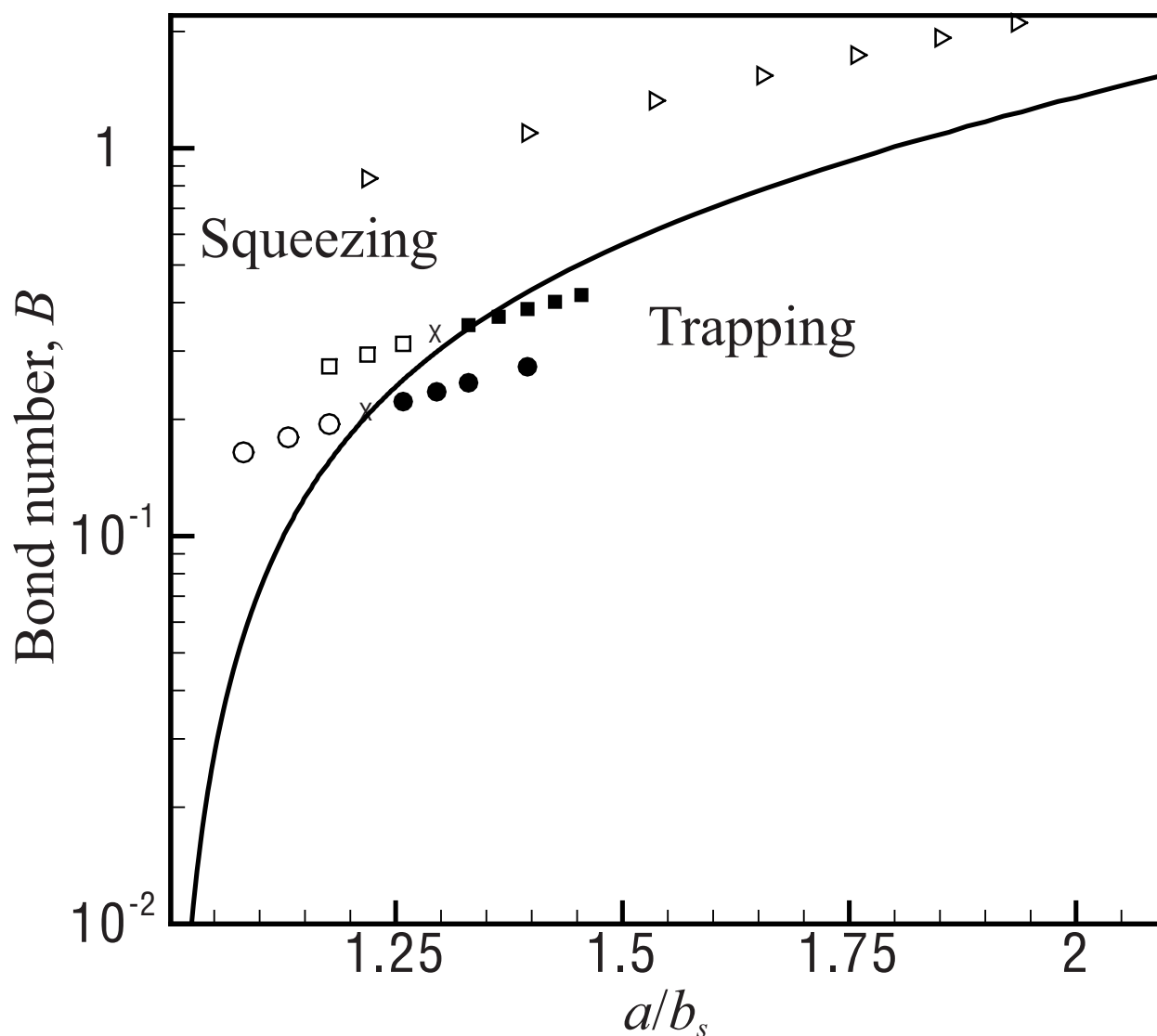


Fig. 4.5: Experimental determination of the critical Bond number for three different drop phases using O-ring 3 from Table 4.2 with  $a_s/b_s = 0.567$ . The circles represent 100% water drops, the squares represent 75% water drops, the triangles are for 16% water drops, and the solid curve is the predicted critical Bond number. The open symbols are drops that pass through the O-ring, the closed symbols are for the drops that become trapped in the O-ring, and the  $\times$  symbols are for the drop sizes where both trapping and squeezing are observed in repeated trials.

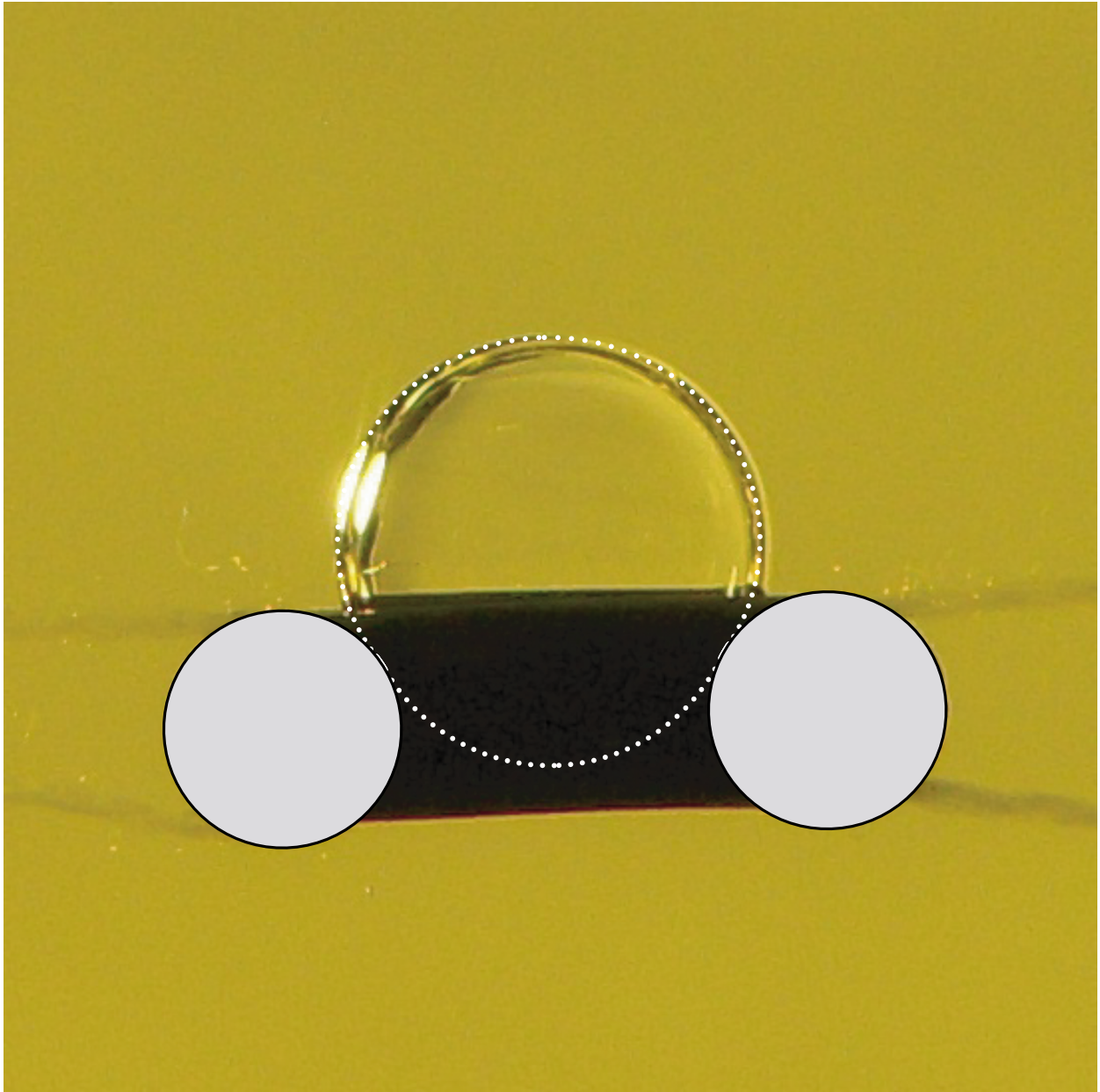


Fig. 4.6: Comparison of theoretical (axisymmetric YL algorithm) and experimental trapped drop interfaces for  $a_s/b_s \approx 0.773$ ,  $a/b_s \approx 1.3$ ,  $\mu_d/\mu_e \approx 0.013$  (experiment only), and  $B \approx 0.13$ , where the dotted white curve is the theoretical drop interface and the gray circles represent the 2D cross section of the torus.

### 4.3.2 Agglomerate of three, touching spheres

The critical Bond number is experimentally determined for an agglomerate of three spheres (touching) with  $a_s/b_s \approx 6.46$ , by varying the drop size ( $a/b_s$ ) until the transition from drop trapping to squeezing is observed. As shown in Fig. 4.7, interfacial tension of pure water is too high and all the drops within the size range studied become trapped in the agglomerate. Conversely, the drops with 16% water are too deformable and they all passed through the agglomerate. Finally, for drop with 75% water, a transition between squeezing and trapping was observed. However, the theoretical critical Bond number curve is close to all of the data points using the 75% water phase, and so accurate comparison of theory and experiment is not possible.

A trapped drop shape for the 75% water phase is shown in Fig. 4.8. The shape of the trapped drop is very similar to the ones computed using the 3D YL algorithm from Ch. 3, with a spherical cap at the top, three large dimples caused by the solid spheres and a small leading edge protruding into to the hole. Note that the theoretical curve for the critical Bond number, separating the parameter space for squeezing ( $B > B_c$ ) and trapping ( $B < B_c$ ) is independent of the fluid composition.

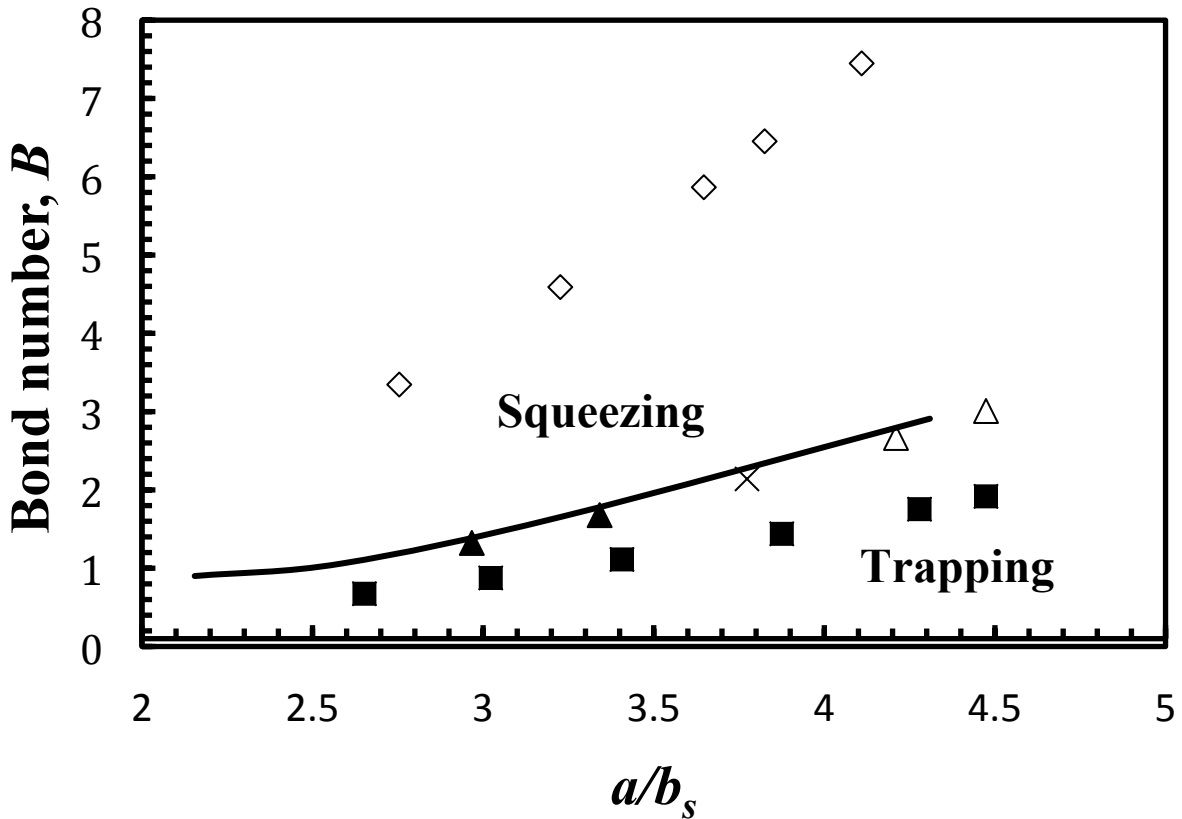


Fig. 4.7: Experimental determination of the critical Bond number for three different drop phases using an agglomerate of three spheres from Figure 4.1 with  $a_s/b_s \approx 6.46$ . The squares represent 100% water drops, the triangles represent 75% water drops, the diamonds are for 16% water drops, and the solid curve is the predicted critical Bond number from the 3D YL algorithm in Chpt. 3. The open symbols are drops that pass through the agglomerate, the closed symbols are for the drops that become trapped in the agglomerate, and the  $\times$  symbols are for the drop sizes where both trapping and squeezing are observed in repeated trials.

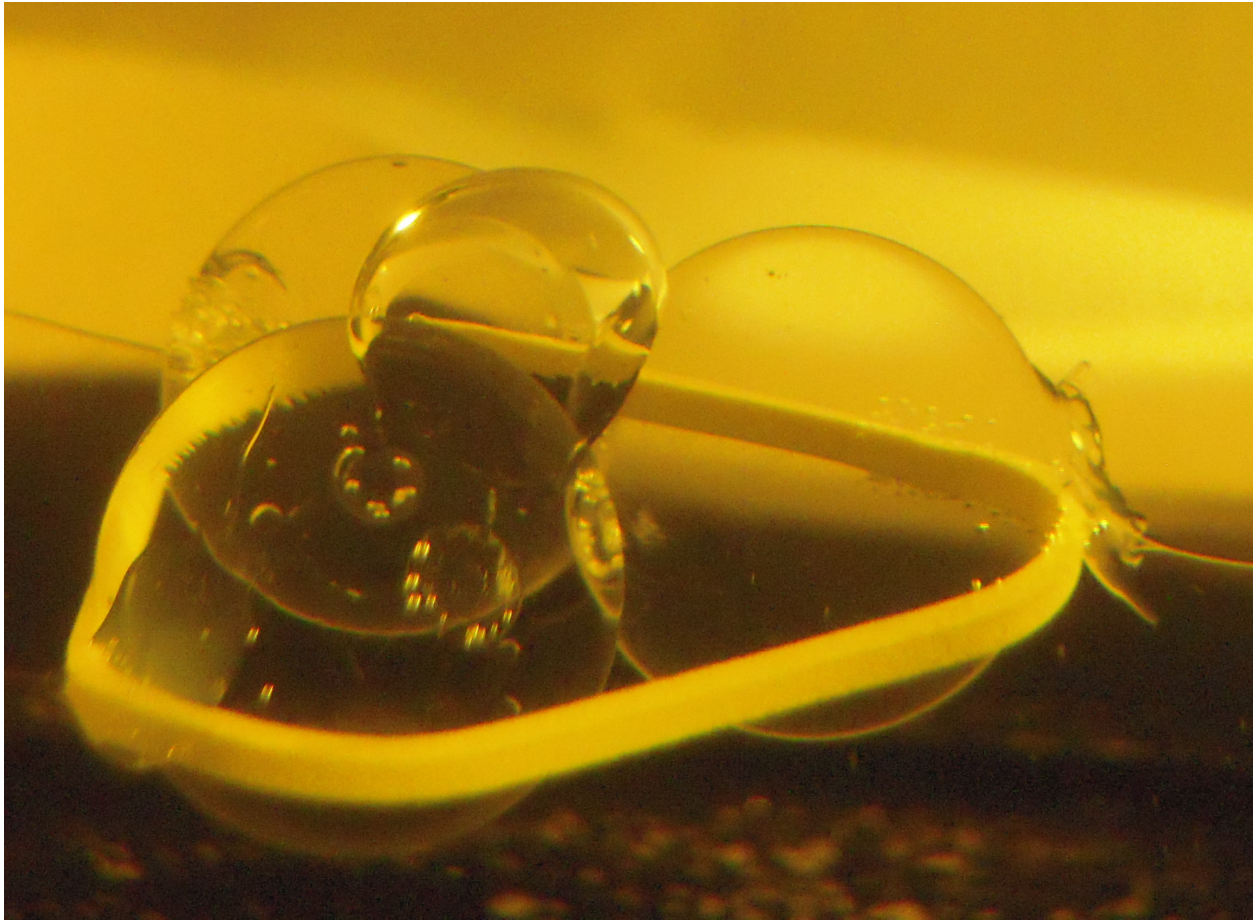


Fig. 4.8: A deformable drop statically trapped in an agglomerate of three spheres with  $a_s/b_s \approx 6.46$ ,  $a/b_s \approx 3.65$  and  $B \approx 2.0$  using the 75% water phase for the drop.

#### 4.4 Sphere radius versus Bond number scaling

Of practical note, since the Bond number,  $B = \Delta\rho g a^2 / \sigma$ , is proportional to the square of the drop radius, then increasing the size of the agglomerate while keeping  $a/b_s$  and  $a_s/b_s$  constant increases the Bond number for constant fluid properties. The relationship between the solid sphere radius and the Bond number is then

$$a_s \propto K_1 (a / b_s) \sqrt{B}, \quad (4.1)$$

where

$$K_1 (a/b_s) = \frac{6.45 b_s}{a \sqrt{\Delta\rho g / \sigma}}, \quad (4.2)$$

for three touching spheres. The scaling in Eq. (4.1) is also more general for any agglomerate of touching spheres, ring, hyperboloid tube or any solid constriction described by a single nondimensional geometric parameter that is fixed, but the numerical constant in Eq. (4.2) will be different for each constriction. The scaling of Eq. (4.1) is a worthwhile consideration of practical importance, when designing a system such as an emulsion settling through a tightly packed bed of stationary spheres, which is used for liquid/liquid separation.

#### 4.5 Concluding Remarks

Drop squeezing and trapping mechanisms were observed experimentally using an apparatus with canola oil bulk phase and water or water/glycerol drop phase. Critical Bond numbers  $B_c$  were experimentally determined by placing increasingly larger drops on both a ring and an agglomerate of three spheres and detecting the transition from squeezing to trapping. The experimentally determined  $B_c$  compares favorably with the theoretical values obtained from both the axisymmetric YL algorithm and the 3D YL algorithm. The transition between squeezing and

trapping is strongly dependent on the hole size of the ring and the fluid properties of the drop but only weakly dependent on the cross-sectional size of the ring, in good agreement with theory. Also, experimental trapped drop shapes show good agreement with those calculated using the axisymmetric YL algorithm. For designing a system of an emulsion settling through tightly packed spheres, or another porous medium with uniform spheres, the size of the spheres scales with the square root of the Bond number of drops with constant  $a/b_s$ . Potential future work includes fitting an empirical drop shape using the agglomerate using the 3D YL algorithm, discussed in detail in Chpt. 3, as an attempt of a new method to calculate physical properties, such as contact angle or interfacial tension.

## Chapter 5

### Drops statically trapped in rings with varying contact angle

#### Abstract

The shape of a deformable drop statically trapped in an axisymmetric ring constriction with a prescribed contact angle is numerically calculated using the Young-Laplace equations. The two drop-fluid interfaces are simultaneously determined, and the wetting area is automatically found from knowing the wetting points of the three-phase contact. An iterative scheme is used to converge the solutions of two differential equations to satisfy both volume constraint and pressure continuity. For contact angles near  $180^\circ$ , the critical Bond number is weakly dependent on the contact angle, so previous calculations for nonwetting drops may be used in this situation for a good approximation. Far away from  $180^\circ$ , the critical Bond numbers are observed to substantially decrease with decreasing contact angle. Also, a special case for a neutrally-buoyant deformable drop (Bond number of zero) statically trapped in a ring with a prescribed contact is considered and found to consist of two spherical caps joined by a fluid bridge in contact with the ring.

#### 5.1 Introduction

As previously mentioned, there is a vast amount of past research on calculating static deformable drop shapes using the Young-Laplace equation. Most of the research has been

focused on sessile or pendant drops on solid surfaces, but less work has been performed for drop trapping until the recent paper by Ratcliffe et al. (2010), which calculates the shape of a deformable drop, assumed to be “nonwetting,” statically trapped in an axisymmetric ring constriction. The present work is an extension of the previous research, but with varying contact angle between the drop and solid surfaces at the wetting points, to study the effects of the contact angle on the critical Bond number and trapped drop shapes. This study is restricted to contact angles between  $90^\circ$  and  $180^\circ$ , because additional changes to the algorithm are needed for contact angles less than  $90^\circ$ . It is important to note that the shape of a trapped drop with arbitrary contact angle is calculated using first principles only, and no empirical or a priori knowledge of the wetted area is needed for the calculation.

## 5.2 Numerical Methods

Most of the theory and numerical methods of the current problem are directly borrowed from our research discussed in Sec. 2.4 of a deformable drop statically trapped in an axisymmetric ring. The geometry parameters of  $a$ ,  $a_s$  and  $b_s$  are the undeformed drop, the solid cross-section and the hole radii, respectively. A key difference in the current work is that the drop interface is no longer restricted to depart tangent to the solid surface, but instead the contact angle is arbitrary. This change requires modification of the numerical methods, and convergence to the solution of a deformable drop statically trapped with an arbitrary wetting angle in an axisymmetric ring is observed to be much more computationally intensive than the problem in Sec. 2.4.

The following methods are unchanged from the problem in Sec. 2.4, including using constraints Eq. (2.35) and (2.36) for volume conservation and pressure continuity, respectively,

to numerically converge to the steady state, by simultaneously solving the sessile, pendant and wetted portions of the drop shape by numerically integrating the differential form of the Young-Laplace equation (Eq. (2.37)) and using asymptotic initial conditions Eq. (2.38) for the first integration step.

Since the assumption that the contact angle is  $180^\circ$  is no longer used, the criterion to stop the numerical integration of Eq. (2.37), because the wetting point  $W_i$  is reached, changes from Eq. (2.39) to the following expression:

$$0 = \rho - b_s + a_s \left[ \sin(\alpha - \theta_i^*) - 1 \right], \quad (5.1)$$

where  $\rho$  is the radial coordinate (in a cylindrical coordinate system) of the drop interface,  $\theta_i^*$  is the angle between the tangent vector of the drop surface and the  $\rho$ -axis at  $W_i$ , and  $\alpha$  is the prescribed contact angle at both  $W_1$  and  $W_2$ . Changing the criterion for wetting from Eq. (2.37) to Eq. (5.1) also changes some of the derivative terms used in the iterative scheme to converge to  $F(C) = 0$ .

The critical Bond number is still determined by monitoring the determinate of the Jacobian matrix for the derivatives of  $F(C)$ , and calculated at the Bond number where the determinate equals zero, which mathematically corresponds to the loss of a steady state. The curves for  $F(C)$  are steep, so Newton-Raphson iterations diverge from the steady state. Instead the method of steepest descent is used to converge to the steady state; however, this convergence scheme is much more computationally intensive than Newton-Raphson iterations. Additionally, using  $C_1 = C_2 = 2$  for an initial approximation (spherical drop) for the drop shape near the critical Bond number is no longer valid, since there is a prescribed contact angle. So, we have to slowly step down contact angles from  $180^\circ$  and use the converged  $C_1$  and  $C_2$  values from the previous contact angle for the initial guess.

### 5.3 Numerical results

First, critical Bond numbers  $B_{cr}$  are shown in Fig. 5.1 versus drop size for several contact angles near  $180^\circ$ . It is clear that the critical Bond number calculations for “non-wetting” drops with contact angle of  $180^\circ$  are an excellent approximation for critical Bond numbers for drops with contact angles of  $165^\circ \leq \alpha \leq 180^\circ$ . Since calculating the trapping shape of “non-wetting” drops is much more computationally inexpensive, the rest of the work will focus on wetting angles further away from  $180^\circ$ .

The critical Bond number significantly decreases with decreasing contact angle away from  $180^\circ$ , as observed in Fig. 5.2. Static drop shapes, just below the critical Bond number, are shown in Fig. 5.2 for the geometry parameters  $a/b_s = 1.5$  and  $a_s/b_s = 3$ . The critical Bond number is observed to decrease by more than half as the contact angle is decreased from  $165^\circ$  to  $135^\circ$ . It is clear from the drop shapes that decreasing the contact angle allows trapped drops to protrude farther into the hole for the same Bond number, due to the additional intermolecular forces accounted by the contact angle. Of important note is that, for contact angles below  $180^\circ$ , the bottom wetting point may fall below the centerline of the ring (as seen in Figure 5.2), which was never observed for “nonwetting” drops. The pendant portion of the drop shape has an additional force term accounted by the contact angle, which pulls upward on the drop, allows the pendant portion to hang lower into the hole without loss of a steady state.

As shown in the Fig. 5.3, a neutrally-buoyant, deformable drop is statically trapped in ring constriction with  $\alpha = 127^\circ$ ,  $a/b_s = 1.5$ ,  $a_s/b_s = 3$  and of course  $B = 0$ . The deformation of the drop is a three-portion, force balance (excluding gravity) including intermolecular forces between the

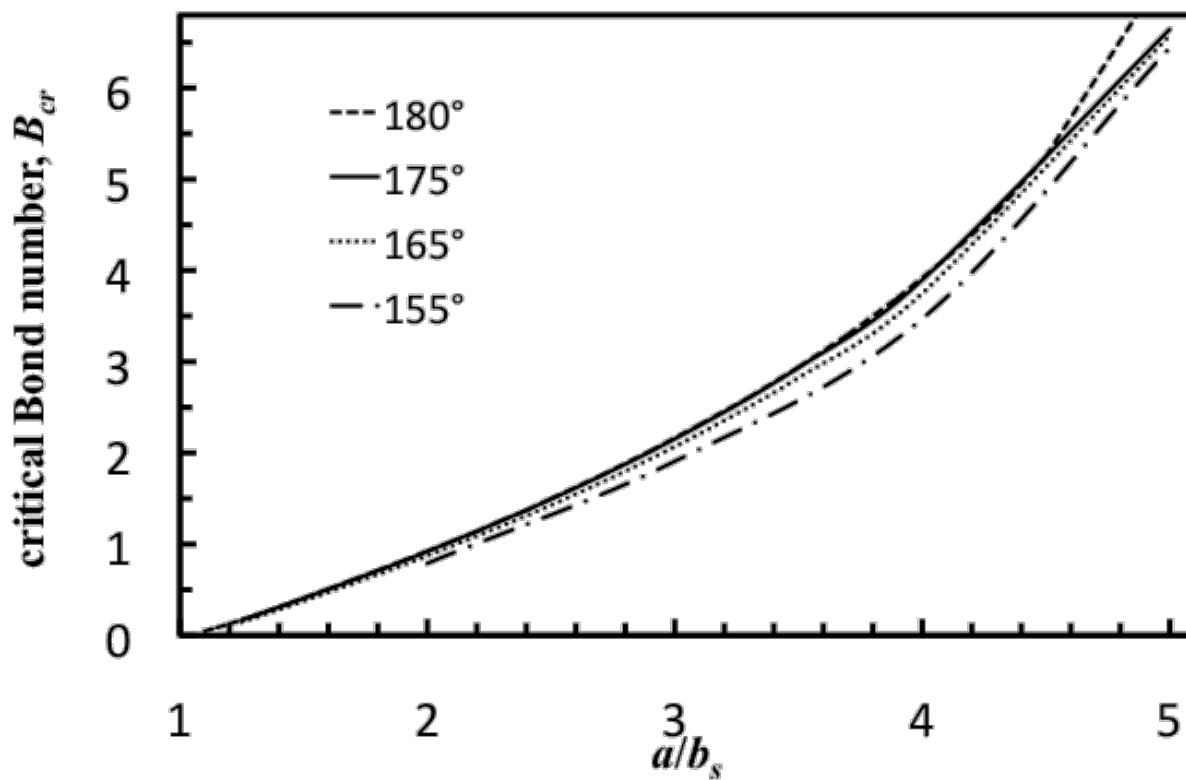


Fig. 5.1: The Critical Bond number vs the drop-to-hole radius ratio for rings with  $a_s/b_s = 3$ , and contact angles of 180°, 175°, 165° and 155° from top to bottom.

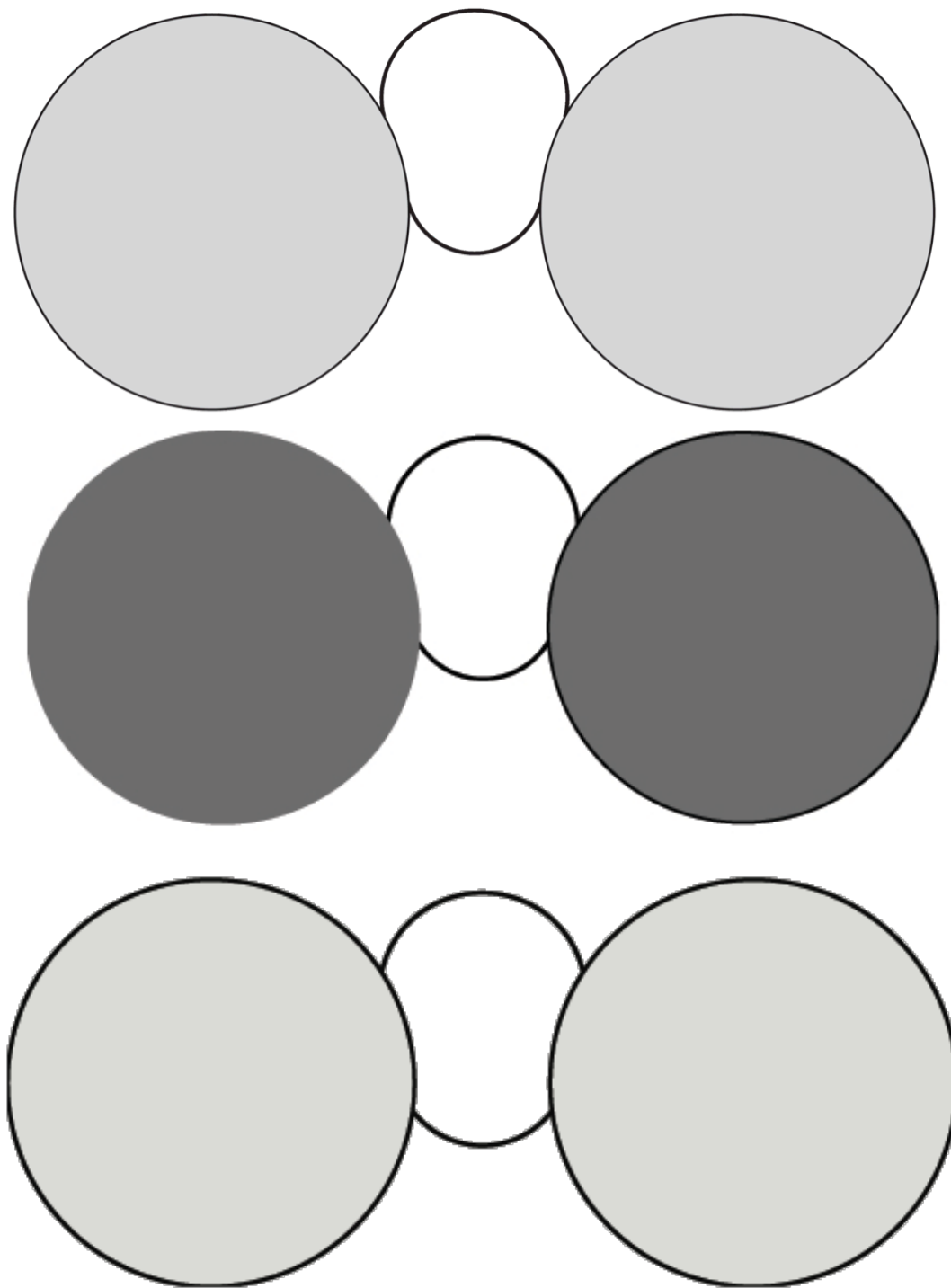


Fig. 5.2: Drops trapped just below the critical Bond number in a ring with  $a/b_s = 1.5$ ,  $a_s/b_s = 3$  and contact angles  $165^\circ$  and  $B = 0.376$ ,  $145^\circ$  and  $B = 0.252$  and  $135^\circ$  and  $B = 0.172$  from top to bottom.

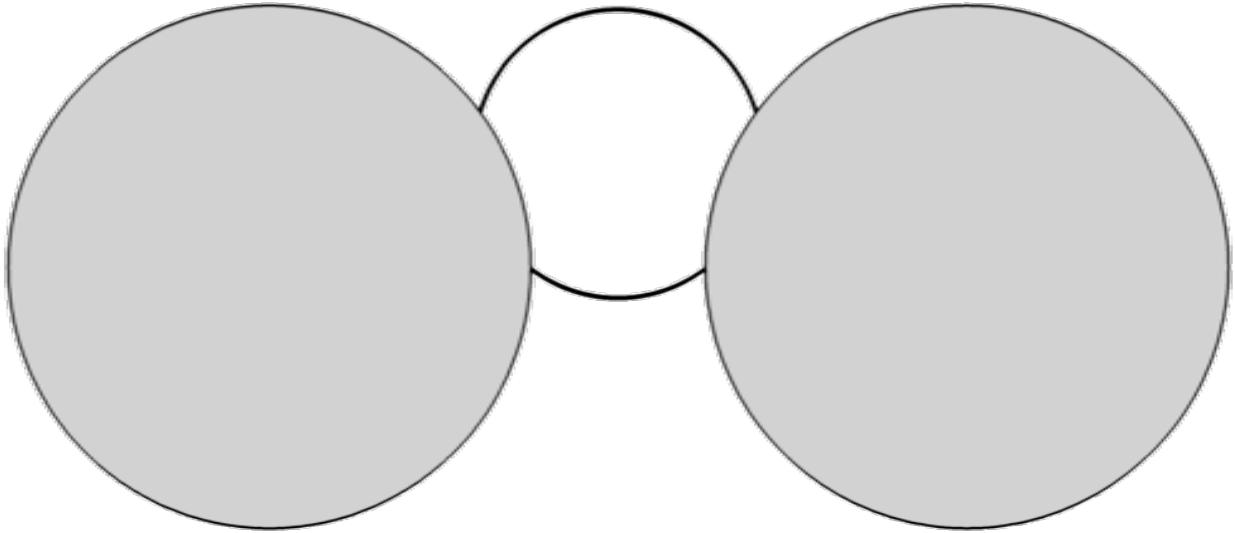


Fig. 5.3: A neutrally-buoyant (Bond number  $B = 0$ ) deformable drop, with arbitrary interfacial tension  $\sigma$ , statically trapped in a ring constriction, where the black curves represent the drop and solid gray circles represent the cross section of the ring constriction. The contact angle  $\alpha = 127^\circ$ , the drop-to-hole radius ratio  $a/b_s = 1.5$ , and the solid cross-section-to-hole radius ratio is  $a_s/b_s = 3$ .

solid and both fluid phases, which prescribe the contact angle, due to the pressure difference sustained across the drop-fluid interfaces, which is constant for neutrally buoyant drops, and the forces normal to the drop surface, due to the interfacial tension between the two fluid phases.

It is important to note that this special case employs a numerical calculation using theory, and may have not been empirically observed before. Also, the solution of this case for neutrally-buoyant drops might be unstable; therefore, empirical observation of this special limiting case of trapping might be impossible. More research is needed on this special, limiting case of trapping such as exploring the stability of the solution mathematically, and empirically attempting to observe this special case.

#### **5.4 Concluding remarks**

The algorithm presented in Ch. 2 for calculating the static shape of a “nonwetting” deformable drop trapped in an axisymmetric constriction has been extended to solve for an arbitrary wetting angle. The solution of the static shapes requires an iterative method, and with the addition of the arbitrary wetting angle the calculations become much more computationally expensive. For contact angles near  $180^\circ$ , the critical Bond number is very weakly dependent on the contact angle, and approximations of the critical Bond number from the “nonwetting” calculations should be used to avoid additional computational costs. However, for contact angles further away from  $180^\circ$ , the critical Bond number is strongly affected by the contact angle, because drops with smaller contact angles are able to protrude farther into the ring hole for the same Bond number. The shape of a neutrally-buoyant deformable drop ( $B = 0$ ) statically trapped with a prescribed wetting angle of  $127^\circ$  is calculated. This is an interesting calculation deserving more attention, to determine if this theoretical calculation is stable, and therefore, experimentally

observable. Since gravitational force is absent for neutrally-buoyant drops, this special limiting case of trapping may have potential for many different applications including microfluidics and measuring physical properties between solids and fluids.

## Chapter 6

### Concluding Remarks and Recommendations for Future Work

Emulsion flows through confined geometries such as packed beds and porous media have many important applications, including food and pharmaceutical manufacturing, oil recovery and fixed-bed catalytic reactors. Treating an emulsion flow as a continuous phase may be valid when the drops are much smaller than the constriction pathways. However, when the drops and constrictions are of comparable size, continuum models fail because complex phenomena including drop-solid interactions are ignored, such as pore blockage, circuitous flow pathways, and complex squeezing mechanisms brought on by constrictions.

The objectives of this dissertation are to model buoyancy-induced drop motion through tight constrictions and to determine the critical conditions, below which a drop becomes trapped in the throat of a constriction. To effectively model and design a process of an emulsion flow through solid constrictions, it is essential to know the critical conditions, delineating the boundary between the two consequential flow behaviors of dynamic drop squeezing through the constriction and static drop trapping by the constriction. Simulation models were developed for both axisymmetric and three-dimensional (3D) constrictions, and experiments were performed to validate the simulation results. The key result of this work is determination of the critical Bond number, below which the drops become trapped in the constriction and above which the drops deform enough to squeeze through the constriction. Other results of interest are the static shapes

of trapped drops for subcritical Bond numbers and the dynamic shapes and squeezing times to pass through the constriction at supercritical Bond numbers.

### **6.1 Buoyancy-induced Drop Motion in an Axisymmetric Ring**

The relevant nondimensional parameters affecting the drop motion in an axisymmetric constriction are the Bond number, which is a ratio of the gravitational and interfacial forces, the ratio of the drop fluid to external fluid viscosities, the cross-section-to-hole size ratio of the constriction and the drop-to-hole size ratio. At successive times, simulation snapshots illustrate the differences between the drop motion for pass through and for the approach to the statically trapped shape. Theoretical results using axisymmetric boundary-integral simulations are presented as a function of the nondimensional parameters, for both the squeezing dynamics and the static shapes of drops in constrictions made of toroidal rings. The drop velocity in the throat typically decelerates 100-fold or more, and the drop-solid separation typically decreases to 0.1%–1% of the undeformed drop radius. For near-critical squeezing, the drop is considerably slowed by the constriction, as measured by an increase in the time for the drop to pass through the constriction as the Bond number is decreased toward its critical value.

Using axisymmetric simulations to fully resolve the hydrodynamics on both the drop and solid surfaces, drop pass-through times are accurately calculated for Bond numbers above the critical value. The critical Bond number is then determined by extrapolation of these results as the drop pass-through time approaches infinity. A power-law scaling is observed for which the drop pass-through time varies inversely with the square of the difference in the Bond number and its critical value.

Near the critical conditions, dynamic boundary-integral simulations for buoyancy-induced drop motion in constrictions become computationally prohibitive. A special, static algorithm, based on the Young-Laplace equation, was developed to efficiently and accurately calculate both the static drop shapes trapped in axisymmetric constrictions and the critical Bond numbers. The critical Bond numbers extrapolated from the dynamic algorithm compare favorably to the values from this special, static algorithm. Calculated from the static Young-Laplace algorithm, the critical Bond number was found to nearly linearly increase with an increase in the most significant factor, the drop-to-hole size ratio, because the drops must be more deformable to pass through tighter holes. The critical Bond number weakly decreases, with an increase in the cross-section, due to a smoother constriction pathway.

However, the critical Bond number versus drop-to-ring radius ratio was found to have a sharp peak. Beyond this point, the drops are so large that they drip over the exterior edge of the ring, rather than pass through the interior hole. The dripping phenomenon for large drops was verified by dynamic boundary-integral methods.

Interesting future research on this topic include modifying the axisymmetric boundary-integral algorithm to simulate flow-induced drop motion in constrictions. For the flow-induced drop motion, it would be interesting to see if the power-law exponent of -2 for the drop pass-through time scaling versus  $B-B_{cr}$  is also observed, as preliminary research indicates a power-law exponent of -3 for flow-induced drop motion, using less-accurate, three-dimensional boundary-integral simulations as in Zinchenko and Davis (2008). It may also be possible to analytically derive the drop pass-through time scaling using asymptotic analysis.

## 6.2 Trapping of a Deformable Drop in a Three-dimensional Constriction

The shape of a deformable drop, statically trapped in a three-dimensional constriction (3D) due to buoyancy, was found using an artificial evolution of the drop surface. Advancement of the drop surface is controlled by a specially-designed, normal “velocity,” containing both a local deviation from the Young-Laplace equation and the drop-solid clearance normal to the drop surface. The benefits of using a simple, artificial motion to solve the 3D Young-Laplace equation are that prior knowledge of the drop-solid contact and iterations of the shape solution are nonessential. This method is also much less computationally intensive than using dynamic boundary-integral simulations to track the drop motion as it enters the constriction and then approaches a static, trapped shape.

For conditions near critical, where the steady-state shape ceases to exist, severe surface-mesh distortions are treated by ‘passive mesh stabilization,’ mesh relaxation and topological transformations through node reconnections. For Bond numbers above critical, the drops are deformable enough to pass through the hole of the constriction, but their motion is slowed as they squeeze through it. The artificial approach determines critical Bond numbers by linear extrapolation of the Bond numbers above critical versus the corresponding minima of the root-mean-squared surface velocities.

Calculations from the present algorithm, including the statically, trapped drop shapes and critical Bond numbers, for both ring and hyperbolic tube constrictions, show excellent agreement with highly-accurate calculations from the axisymmetric Young-Laplace method. For the hole between three fixed spheres, drop shapes from the 3D Young-Laplace algorithm and laborious, 3D boundary-integral simulations are in excellent agreement.

The critical Bond numbers from the 3D Young-Laplace algorithm are presented for holes of different constriction types and sizes, including circular rings, hyperbolic tubes, and agglomerates of three or four spheres. Of primary importance is that the critical Bond number almost linearly increases with the increase in the drop-to-hole size ratio. Quite differently, the constriction type and the tilt angle, which is the angle between gravity and the normal to the plane containing the minimum hole area, only weakly affect the critical Bond number. Unexpectedly, increasing the tilt angle decreases the critical Bond number, because the minimum hole size of the constriction increases in a plane that is normal to the gravity vector.

Interesting future research, which could potentially use the new “time-dependent” approach to solve statically trapped drop shapes without prior knowledge of the contact area, include calculating the static shape of drops resting on a rough or porous surface, or resting on a bed of loose particles, such as a flat surface covered with sand. Another potential area of research is combining this new algorithm for statically trapped drop shapes with a 3D boundary-integral algorithm to model many emulsion drops settling through a collection of solid constrictions. If it is possible to determine if a drop is going to be temporarily trapped in a constriction, the boundary-integral simulation can be stopped temporarily, so that a special “time-dependent” approach can be used to more accurately determine the static drop shape, before switching back to the dynamic boundary-integral simulation.

### **6.3 Experiments**

An experimental set-up, composed of either a tethered ring or an agglomeration of three and four spheres for the constriction, canola oil for the external fluid and water-glycol mixtures for the drop phase, is used to observe drop squeezing and trapping for comparison and validation of

the physics from the simulation results. The experimentally-observed physics of drop squeezing through and trapping in a ring are in very good agreement with the simulation results. The experimental shape of a statically trapped drop in the ring coincides within measurement accuracy with the shape calculated by the highly-accurate, Young-Laplace algorithm. The nearly linear increase of the critical Bond number with increasing drop-to-hole size ratio, calculated using the axisymmetric Young-Laplace algorithm, are inside the small uncertainty intervals of the experimental critical Bond numbers, determined by increasing the drop size until it is statically trapped in a ring of fixed size.

#### **6.4 Future Related Research**

Closely related to the present research, it would be interesting to simulate deformable capsule motion through tight constrictions as a model for the problem of blood cells flowing through capillaries, since the blood cells are larger than the diameters of the smallest capillaries. The capsule would be treated as a deformable drop with a membrane, so that the physics of squeezing and trapping might be quite different than for regular emulsion drops. Other related problems of potential interest include drop breakup when passing through narrow constrictions and the motion of deformable drops or cells through the narrow and complex channels of microfluidic devices. Perhaps most important would be to return to the original motivation for the dissertation: the flow of an emulsion of many drops through a packed bed or other porous medium. The findings and methods of the current research could be used to determine which drops, would become trapped within the pore throats, and the squeezing times for those drops which pass through the constrictions, ultimately allowing for separate determination of the

pressure-drop/flow-rate relationships for the drop and surrounding fluids and for the gradual plugging of the porous medium as the drops become trapped.

## Bibliography

- Adamenko, I.I., Bulavin, L.A., Ilyin, V., Zelinsky, S.A. and Moroz, K.O. 2006 Anomalous behavior of glycerol–water solutions. *J. Mol. Liq.* **127** 90-92.
- Bashforth, F., and Adams, J. C., “An Attempt to Test the Theory of Capillary Action.” Cambridge, 1892.
- H. Bateman and A. Erdelyi, *Higher Transcendental Functions* (McGraw-Hill, New York, 1953), Vol. 1.
- Bławdziewicz, J., Cristini, V. and Loewenberg, M. 2002 Critical behavior of drops in linear flows. I. Phenomenological theory for drop dynamics near critical stationary states. *Phys. Fluids* **14** 2709.
- Bretherton, F. P. 1961 The motion of long bubbles in tubes. *J. Fluid Mech.* **10**, 166.
- Brown, R. A., Orr, F. M. and Scriven, L. E. 1980 Static Drop on an Inclined Plate: Analysis by the Finite Element Method. *J. Colloid Interface Sci.* **73**, 76-87.
- Chatterje, J. 2002 Critical Eotvos numbers for buoyancy-induced oil drop detachment based on shape analysis. *Adv. Colloid Interface Sci.* **98**, 265-283.
- Chatterje, J. 2007 Prediction of coupled menisci shapes by Young–Laplace equation and the resultant variability in capillary retention. *J. Colloid Interface Sci.* **314**, 199-206.
- Chi, B. 1986 The motion of immiscible drops and the stability of annular flow. Ph.D. thesis, California Institute of Technology.
- J. T. Davies and E. K. Rideal, *Interfacial Phenomena* (Academic, New York, 1963).
- Davis, R. H. 1999 Buoyancy-driven viscous interaction of a rising drop with a smaller trailing drop. *Phys. Fluids* **11** 1016.
- Goldsmith, H. L. and Mason, S. G. 1963 The flow of suspensions through tubes. II. Single large bubbles. *J. Colloid Interface Sci.* **18**, 237.

Hartland, S. & Hartley, R.W. *Axisymmetric fluid-liquid interfaces: Tables giving the shape of sessile and pendant drops and external menisci, with examples of their use.* (Elsevier Scientific Pub. Co., Amsterdam and New York, 1976).

Hebeker, F. -K. 1986 Efficient boundary element methods for three-dimensional exterior viscous flow. *Numer. Methods Partial Differ. Equ.* **2**, 273.

Hodges, S. R., Jensen, O. E. and Rallison, J. M. 2004 Sliding, slipping and rolling: The sedimentation of a viscous drop down a gently inclined plane. *J. Fluid Mech.* **512**, 95.

G. A. Korn and T. M. Korn, *Mathematical Handbook for Scientists and Engineers* (McGraw-Hill, New York, 1968).

Kushner, J., Rother, M. A. and Davis, R. H. 2001 Buoyancy-driven interaction of viscous drops with deforming interfaces. *J. Fluid Mech.* **446**, 253.

Kim, S. and Karrila, S.J. 1991 *Microhydrodynamics: Principles and selected applications.* Butterworth-Heinemann, Boston.

S. L. Kokal, B. B. Maini, and R. Woo, in *Emulsions Fundamentals and Applications in the Petroleum Industry*, Advances in Chemistry Series Vol. 231, edited by L. L. Schramm (University Press, New York, 1992), pp. 219–262.

Lee, S. H. and Leal, L. G. 1982 The motion of a sphere in the presence of a deformable interface. II. A numerical study of the translation of a sphere normal to an interface. *J. Colloid Interface Sci.* **87**, 81.

Leyrat-Maurin, A. and Barthes-Biesel, D. 1994 Motion of a deformable capsule through a hyperbolic constriction. *J. Fluid Mech.* **279**, 135.

Loewenberg, M. and Hinch, E. J. 1996 Numerical simulation of a concentrated emulsion in shear flow. *J. Fluid Mech.* **321**, 395.

Majumdar, S. R. and O'Neill, M. E. 1977 On axisymmetric Stokes flow past a torus. *Math. Phys.* **28**, 541.

Martinez, M. J. and Udell, K. S. 1989 Axisymmetric creeping motion of drops through a periodically constricted tube. *AIP Conf. Proc.* **197**, 222.

Martinez, M. J. and Udell, K. S. 1990 Axisymmetric creeping motion of drops through circular tubes. *J. Fluid Mech.* **210**, 565.

P. Morse and H. Feshbach, *Methods of Theoretical Physics* (McGraw-Hill, New York, 1953).

Navot, Y. 1999 Critical behavior of drop breakup in axisymmetric viscous flow. *Phys. Fluids* **11**, 990.

- Nemer, M. B., Chen, X., Papadopoulos, D. H., Blawdziewicz, J. and Loewenberg, M. 2004 Hindered and enhanced coalescence of drops in Stokes flows. *Phys. Rev. Lett.* **92**, 114501.
- O'Brien, S. B. G. 1991 On the shape of small sessile and pendant drops by singular perturbation techniques. *J. Fluid Mech.* **233**, 519.
- Olbricht, W. L. and Leal, L. G. 1983 The creeping motion of immiscible drops through a converging/diverging tube. *J. Fluid Mech.* **134**, 329.
- Olbricht, W. L. and Kung, D. M. 1992 The deformation and breakup of liquid drops in low Reynolds number flow through a capillary. *Phys. Fluids A* **4**, 1347.
- Olbricht, W. L. 1996 Pore-scale prototypes of multiphase flow in porous media. *Annu. Rev. Fluid Mech.* **28**, 187.
- Padday, J.F. 1971 The Profiles of Axially Symmetric Menisci. *Phil. Trans. R. Soc. Lond. A* **269** 265-293.
- Padday, J.F. & Pitt, A. R. 1973 The Stability of Axisymmetric Menisci. *Phil. Trans. R. Soc. Lond. A* **275** 489-528.
- C. Pozrikidis, *Boundary-Integral and Singularity Methods for Linearized Viscous Flow* (Cambridge University Press, New York, 1992).
- Rallison, J. M. and Acrivos, A. 1978 A numerical study of the deformation and burst of a viscous drop in an extensional flow. *J. Fluid Mech.* **89**, 191.
- Ratcliffe, T. J., Zinchenko, A. Z., & Davis, R. H., Buoyancy-induced squeezing of deformable drop through an axisymmetric ring constriction. *Phys. Fluids* **22**, 082101 (2010).
- Rotenberg, Y., Boruvka, L., and Neumann, W. 1983 Determination of surface tension and contact angle from the shapes of axisymmetric fluid interfaces. *J. Colloid Interface Sci.* **93**, 169-183.
- Stengel, K. C., Oliver, D. S. and Booker, J. R. 1982 Onset of convection in a variable viscosity fluid. *J. Fluid Mech.* **120**, 411-431.
- Tsai, T. M. and Miksis, M. J. 1994 Dynamics of a drop in a constricted capillary tube. *J. Fluid Mech.* **274**, 197.
- Zinchenko, A. Z. & Davis, R. H. Shear flow of highly concentrated emulsions of deformable drops by numerical simulations. *J. Fluid Mech.* **455**, 21-62 (2002).
- Zinchenko, A. Z. & Davis, R. H. Large-scale simulations of concentrated emulsion flows. *Phil. Trans. R. Soc. Lond. A* **361**, 813-845 (2003).

Zinchenko, A. Z. & Davis, R. H. Hydrodynamical interaction of deformable drops. In *Emulsions: Structure Stability and Interactions* (ed. D. N. Petsev), pp. 391–447. Elsevier (2004).

Zinchenko, A. Z. and Davis, R. H. 2006 A boundary-integral study of a drop squeezing through interparticle constrictions. *J. Fluid Mech.* **564**, 227.

Zinchenko, A. Z. and Davis, R. H. 2008 Squeezing of a periodic emulsion through a cubic lattice of spheres. *Phys. Fluids* **20**, 040803.

Zinchenko, A. Z. and Davis, R. H. 2008 Algorithm for direct numerical simulation of emulsion flow through a granular material. *J. Comput. Phys.* **227**, 7841.

# APPENDIX: ANALYTICAL CALCULATIONS OF SINGULAR AND NEAR-SINGULAR INTEGRALS OVER A TOROIDAL SURFACE

According to Zinchenko and Davis,<sup>11</sup> the following general formulas apply to Cartesian components of the additional integrals in Eqs. (11,16):

$$\int_{S_p} \left( \frac{\delta_{ij}}{r} + \frac{r_i r_j}{r^3} \right) dS_x = (\delta_{ij} - R_i \nabla_j) \int_{S_p} \frac{dS_x}{r} + \nabla_j \int_{S_p} \frac{\xi_i}{r} dS_x, \quad (\text{A1})$$

$$\Psi_{k,\ell,m}(\mathbf{y}) = \frac{1}{8\pi} \left\{ (\delta_{k\ell} \nabla_m + \delta_{k m} \nabla_\ell - R_\ell \nabla_k \nabla_m - R_m \nabla_k \nabla_\ell) \int_{D_p} \frac{1}{r} dV_x + \nabla_k \nabla_m \int_{D_p} \frac{1}{r} dV_x \right\}$$

where  $r = x - y$ ,  $\nabla_j = \partial/\partial y_j$ ,  $\xi = x - xpc$ ,  $R = y - xpc$ ,  $xpc$  is an arbitrary reference point conveniently chosen to be the constriction center, and  $D_p$  is the volume inside  $S_p$ . Calculation of the additional integrals is therefore reduced to Newton surface and volume potentials of a torus with constant and linear densities and their derivatives.

The toroidal coordinates  $\xi, \eta$  are introduced and related to the cylindrical coordinates  $\rho, z$  as<sup>31</sup>

$$z = \frac{c \sin \xi}{\sigma - \mu}, \quad \rho = \frac{c \sinh \eta}{\sigma - \mu}, \quad -\pi \leq \xi \leq \pi, \quad \eta \geq 0, \quad (\text{A3})$$

where  $\sigma = \cosh \eta$  and  $\mu = \cos \xi$ . The torus  $S_p$  becomes a coordinate surface  $\eta = \eta_0 = \text{const}$  if  $\sigma_0 = 1 + b_s/a_s$ , and  $c = a_s \sinh \eta_0$ . For  $y = (\rho \cos \phi, \rho \sin \phi, z)$  outside the torus, the three independent surface potentials in Eq. (A1) have the expansions

$$\int_{S_p} \frac{dS_x}{r} = (\sigma - \mu)^{1/2} \sum_{n=0}^{\infty} A_n^0 \mathcal{B}_{n-1/2}(\sigma) \cos(n\xi), \quad (\text{A4})$$

$$\int_{S_p} \frac{\xi_1}{r} dS_x = (\sigma - \mu)^{1/2} \sum_{n=0}^{\infty} A_n^1 \mathcal{B}_{n-1/2}^1(\sigma) \cos(n\xi) \cos \varphi, \quad (\text{A5})$$

$$\int_{S_p} \frac{\xi_3}{r} dS_x = (\sigma - \mu)^{1/2} \sum_{n=1}^{\infty} A_n^3 \mathcal{B}_{n-1/2}^3(\sigma) \sin(n\xi), \quad (\text{A6})$$

where  $A_n^0, A_n^1$ , and  $A_n^3$  are unknown coefficients,  $\mathcal{B}_{n-1/2}(\sigma)$  are half-integer Legendre functions of the first kind regular at  $\sigma = 1$ ,

$$\begin{aligned} \mathcal{B}_{n-1/2}(\sigma) &= \frac{1}{\pi} \int_0^\pi (\sigma + \sqrt{\sigma^2 - 1} \cos \theta)^{n-1/2} d\theta \\ &= \sigma^{n-1/2} \sum_{k=0}^{\infty} \frac{(2n-1)(2n-3)\cdots(2n-4k+1)(2k-1)!!}{8^k k! (2k)!} \left(1 - \frac{1}{\sigma^2}\right)^k, \end{aligned}$$

and  $B_{n-1/2m}(\sigma) = (\sigma^2 - 1)^{m/2} d^m B_{n-1/2}(\sigma) / d\sigma^m$  are the associated functions. For  $\xi_2$  instead of  $\xi_1$  in Eq. (A5), the expansion is the same, with  $\cos \phi$  replaced by  $\sin \phi$ . To derive  $A_{n0}$ ,  $A_{n1}$ , and  $A_{n3}$ , the left hand side potentials (A4, A5, A6) are also considered inside the torus  $S_p$ , where they have similar expansions with different coefficients and  $B_{n-1/2}$ ,  $B_{n-1/21}$  replaced by the second-kind Legendre functions

$$\begin{aligned} \mathcal{D}_{n-1/2}(\sigma) &= \int_0^\infty \frac{d\psi}{(\sigma + \sqrt{\sigma^2 - 1} \cosh \psi)^{n+1/2}} \\ &= \sum_{k=0}^{\infty} \frac{\pi (2k-1)!! (2n+2k-1)!!}{2^{2k+n} (k+n)! k! [\sigma + \sqrt{\sigma^2 - 1}]^{n+2k+1/2}}, \end{aligned} \quad (\text{A8})$$

$$\mathcal{D}_{n-1/2}^m(\sigma) = (\sigma^2 - 1)^{m/2} d^m \mathcal{D}_{n-1/2}(\sigma) / d\sigma^m. \quad (\text{A9})$$

Using the generating function [Eq. 3.10(3)] from Bateman and Erdelyi,<sup>32</sup>

$$\frac{\pi}{\sqrt{2}} (\sigma - \mu)^{-1/2} = \mathcal{D}_{-1/2}(\sigma) + 2 \sum_{n=1}^{\infty} \mathcal{D}_{n-1/2}(\sigma) \cos(n\xi), \quad (\text{A10})$$

the continuity and normal-derivative jump condition for the surface potentials at  $S_p$ , and the explicit form for the Wronskian  $W[\mathcal{D}_{n-1/2}, \mathcal{B}_{n-1/2}]$ ,<sup>33</sup> a system of equations may be obtained for the coefficients of the expansions, yielding

$$A_n^0 = -8\sqrt{2}c(\sigma_0^2 - 1)^{1/2} (2 - \delta_{n,0}) \mathcal{D}'_{n-1/2}(\sigma_0) \mathcal{D}_{n-1/2}(\sigma_0), \quad (\text{A11})$$

$$\begin{aligned} A_n^1 &= -\frac{16\sqrt{2}}{3} c^2 (\sigma_0^2 - 1)^{3/2} (2 \\ &\quad - \delta_{n,0}) \frac{\mathcal{D}''_{n-1/2}(\sigma_0) \mathcal{D}'_{n-1/2}(\sigma_0)}{n^2 - 1/4}, \end{aligned} \quad (\text{A12})$$

$$A_n^3 = -\frac{32\sqrt{2}}{3} c^2 (\sigma_0^2 - 1)^{1/2} n \mathcal{D}'_{n-1/2}(\sigma_0) \mathcal{D}_{n-1/2}(\sigma_0), \quad (\text{A13})$$

where  $\delta_{ij}$  is the Kronecker delta.

The volume potential (A2) outside the torus is also expanded into toroidal harmonics,

$$\int_{D_p} \frac{dV_x}{r} = (\sigma - \mu)^{1/2} \sum_{n=0}^{\infty} a_n^0 \mathcal{B}_{n-1/2}(\sigma) \cos(n\xi), \quad (\text{A14})$$

$$\int_{D_p} \frac{\xi_1}{r} dV_x = (\sigma - \mu)^{1/2} \sum_{n=0}^{\infty} a_n^1 \mathcal{B}_{n-1/2}^1(\sigma) \cos(n\xi) \cos \varphi, \quad (\text{A15})$$

$$\int_{D_p} \frac{\xi_3}{r} dV_p = (\sigma - \mu)^{1/2} \sum_{n=1}^{\infty} a_n^3 \mathcal{B}_{n-1/2}(\sigma) \sin(n\xi). \quad (\text{A16})$$

To derive the coefficients  $a_n^0$ ,  $a_n^1$ , and  $a_n^3$ , the left hand side potentials (A14,A15,A16) are also considered inside the torus where they are expanded in a similar form, with  $\mathcal{D}_{n-1/2}(\mathcal{D}_{n-1/2})$  instead of  $\mathcal{B}_{n-1/2}(\mathcal{B}_{n-1/2})$  and with additional terms  $[-2\pi z^2, -\pi \rho^3 \cos \varphi/2, \text{ and } -2\pi z^3/3 \text{ for Eqs. (A14,A15,A16), respectively}],$  to satisfy the Poisson equation. Differentiating (A10) gives suitable series representations for these supplementary terms. Continuity of the potentials (A14,A15,A16) and their normal derivatives at  $S_p$  then yields the equations for the expansion coefficients. Omitting the algebra, we have

$$a_n^0 = \frac{8\sqrt{2}c^2}{3}(\sigma_0^2 - 1) \{ \mathcal{D}_{n-1/2}[(n+1)\mathcal{D}_{n+1/2}'' - (n-1)\mathcal{D}_{n-3/2}''] - \mathcal{D}'_{n-1/2}[(n+1)\mathcal{D}'_{n+1/2} - (n-1)\mathcal{D}'_{n-3/2}] \}, \quad (\text{A17})$$

$$a_n^1 = \frac{4\sqrt{2}c^3(2 - \delta_{n,0})}{15(n^2 - 1/4)}(\sigma_0^2 - 1)^2 \{ (\sigma_0^2 - 1)[\mathcal{D}_{n-1/2}'''\mathcal{D}'_{n-1/2} - \mathcal{D}_{n-1/2}'\mathcal{D}'_{n-1/2}] - 2\sigma_0\mathcal{D}_{n-1/2}''\mathcal{D}'_{n-1/2} \}, \quad (\text{A18})$$

$$a_n^3 = \frac{16\sqrt{2}}{15}c^3(\sigma_0^2 - 1)n \{ (\sigma_0^2 - 1)\mathcal{D}_{n-1/2}''\mathcal{D}'_{n-1/2} - [(\sigma_0^2 - 1)\mathcal{D}_{n-1/2}'''\mathcal{D}_{n-1/2} + 2\sigma_0\mathcal{D}_{n-1/2}''\mathcal{D}_{n-1/2}] \}. \quad (\text{A19})$$

Here, the  $\mathcal{D}(\sigma)$ -functions and their derivatives up to the fourth order are evaluated at  $\sigma = \sigma_0$ ; in Eq. (A17),  $\mathcal{D}_{n-3/2}''$  and  $\mathcal{D}_{n-3/2}'$  must be omitted when  $n = 0$ .

Upon substitution into Eqs. (A1,A2), the potentials (A4,A5,A6,A14,A15,A16) are differentiated as compound functions of  $y$ , with

$$\sigma = \frac{R_1^2 + R_2^2}{2R_1R_2}, \quad \mu = \frac{R_1^2 + R_2^2 - 4c^2}{2R_1R_2}, \quad (\text{A20})$$

taken into account, where

$$R_1 = [(\rho - c)^2 + z^2]^{1/2}, \quad R_2 = [(\rho + c)^2 + z^2]^{1/2}. \quad (\text{A21})$$

The convergence of all the series is typically fast and about 20–30 terms suffice. Stable and efficient calculation of the necessary derivatives  $\mathcal{D}_{n-1/2}(m)(\sigma)$  (for  $m \leq 4$ ) and  $\mathcal{B}_{n-1/2}(m)(\sigma)$  (for  $m \leq 3$ ) requires some attention, though. For the largest  $n = N_{\max}$ , we use the series (A7,A8) to compute  $\mathcal{D}_{n-1/2}$  and  $\mathcal{B}_{n-1/2}$ , while the elliptical integral representations are used to find  $\mathcal{D}_{-1/2}(\sigma)$  and  $\mathcal{B}_{-1/2}(\sigma)$ . The intermediate values of  $\mathcal{D}_{n-1/2}$ ,  $\mathcal{B}_{n-1/2}$  for  $0 < n < N_{\max}$  are then recovered by the Thomas algorithm for tridiagonal systems via recurrent

relations. The elliptical integral representations for  $D_{-1/2}$ ,  $B_{-1/2}$  also yield  $D_{-1/2}'(\sigma)$ ,  $B_{-1/2}'(\sigma)$ , which are used to calculate  $D_{-1/2}(m)(\sigma)$  ( $m \leq 4$ ) and  $B_{-1/2}(m)(\sigma)$  ( $m \leq 3$ ) recursively. Finally,  $D_{n-1/2}(m)(\sigma)$  is expressed via  $D_{n-3/2}(m)(\sigma)$  and  $D_{n-1/2}(m-1)(\sigma)$  by a stable recurrent relation, similar for  $B_{n-1/2}(m)(\sigma)$ .